
Doctoral

Engineering

2018

High Sensitivity Optical Fiber Interferometric Sensors

Dejun Liu

Technological University Dublin, dejun.liu@tudublin.ie

Follow this and additional works at: <https://arrow.tudublin.ie/engdoc>



Part of the [Electrical and Computer Engineering Commons](#)

Recommended Citation

Liu, D. (2018) *High Sensitivity Optical Fiber Interferometric Sensors*. Doctoral thesis, DIT, 2018. doi.org/10.21427/qjt6-0053

This Theses, Ph.D is brought to you for free and open access by the Engineering at ARROW@TU Dublin. It has been accepted for inclusion in Doctoral by an authorized administrator of ARROW@TU Dublin. For more information, please contact arrow.admin@tudublin.ie, aisling.coyne@tudublin.ie, vera.kilshaw@tudublin.ie.

High Sensitivity Optical Fiber Interferometric Sensors

A thesis

Submitted for the degree of Doctor of Philosophy

by

DEJUN LIU



School of Electrical & Electronic Engineering
College of Engineering & Built Environment
Dublin Institute of Technology

**Supervisors: Dr. Qiang Wu, Prof. Yuliya Semenova and
Prof. Gerald Farrell**

Dublin, Ireland

July, 2018

To my wife, parents, sister, and supervisors with all my love

Abstract

Optical fiber interferometers have been widely employed and investigated for monitoring the changes in both physical and chemical parameters, with the advantages of compact size, light weight, immunity to electromagnetic interference, high sensitivity, capability to work in harsh environments and remote operation capabilities. Among the different kinds of fiber sensors based on interferometry, singlemode-multimode-singlemode (SMS) structures has attracted considerable interest due to their inherent advantages of high sensitivity, ease of fabrication and interconnection to other fiber systems and low cost. However, the challenge is that the sensitivity of the traditional SMS based fiber structure is not sufficient in some cases, for example in bio-chemical applications, where detection of a very small variation in a bio-chemicals' concentration is required. There is thus a need to investigate how to modify or enhance an SMS structure to achieve ultrahigh sensitivity.

This thesis presents research and its applications concerning approaches to improve the sensitivity and detection accuracy of a traditional SMS fiber structure based sensor. The key achievements of this thesis include:

Traditional SMS fiber structure for breathing state monitoring

A bend SMS structure is investigated as a breathing sensor by attaching it to a thin plastic film in an oxygen mask. Breath rate can be monitored using this sensor by detecting power variations due to the macro bending applied to the SMS section during each inhalation and exhalation cycles. Different types of breathing conditions including regular and irregular breath patterns can be distinguished. The proposed sensor is capable of working in a strong

electromagnetic field and radioactive environment.

Tapered small core singlemode fiber (SCSMF) for the detection of refractive index (RI), ammonia, and volatile organic compounds (VOCs)

A modified SMS structure based on a tapered SCSMF is proposed and investigated with significantly improved RI sensitivity. It is found that the sample with a smaller waist diameter gives higher sensitivity. In the experiment, a maximum sensitivity of 19212.5 nm/RIU (RI unit) in the RI range from 1.4304 to 1.4320 has been demonstrated when the waist diameter of the SCSMF is tapered down to 12.5 μm . The best corresponding theoretical resolution of the proposed sensor is 5.025×10^{-7} RIU which is over 10 times higher than that of many previous reported optical fiber based RI sensors. The proposed structure is capable of monitoring relative humidity level change even without coating of the fiber sensor's surface with a layer of hygroscopic material.

A silica sol-gel based coating has been used as a sensitive material to ammonia for the first time, by applying it to the surface of the tapered SCSMF for the detection of ammonia in water. The proposed sensor shows an ultra-high sensitivity of 2.47 nm/ppm with short response and recovery time of less than 2 and 5 minutes respectively. The corresponding theoretical detection limit of ammonia in water is calculated to be 4 ppb, which is 3 orders of magnitude improvement compared to the previous reported interferometry based ammonia sensor. In addition, the sensor has good performance in terms of repeatability of measurement and selectivity for sensing ammonia compared to that of other common ions and organic molecules in water.

VOCs sensors are also demonstrated by coating a mixture of sol-gel silica and Nile red on the surface of two different types of tapered fiber sensors

(tapered SCSMF) and a microfiber coupler (MFC)). The MFC based sensor shows better sensitivities to ethanol and methanol than that based on a tapered SCSMF due to its smaller waist diameter. The detectable gas concentration changes of the MFC based sensor are calculated to be ~ 77 ppb and ~ 281 ppb for ethanol and methanol respectively which are over one order of magnitude improvement than many other reports. The sensors also show fast response times of less than 5 minutes and recovery times varied from 7 to 12 minutes. Simultaneous measurement of ethanol and methanol is achieved by utilizing two different coating recipes.

Hollow core fiber (HCF) structure for high temperature and twist sensing

A modified SMS structure with much improved spectral quality factor (Q) is investigated both theoretically and experimentally. The modified structure is based on a HCF. It is found that periodic transmission dips with high spectral extinction ratio and high Q factor are excited because of the multiple beam interferences introduced by the cladding of the HCF. The HCF structure can be used as a high sensitivity (up to $33.4 \text{ pm}/^\circ\text{C}$) temperature sensor in a wide working temperature range (from room temperature to $1000 \text{ }^\circ\text{C}$).

By coating a thin layer of silver ($\sim 6.7 \text{ nm}$) on one side of the HCF surface, a twist sensor with a maximum sensitivity of $0.717 \text{ dB}/^\circ$ has been achieved, which is the highest twist sensitivity reported for intensity modulation based fiber sensors, with excellent measurement repeatability. Further theoretical and experimental investigation attributes this high twist sensitivity to the polarization dependent reflection coefficient at the outer HCF surface associated with the partial silver coating.

Declaration

I certify that this thesis which I now submit for examination for the award of PhD, is entirely my own work and has not been taken from the work of others save and to the extent that such work has been cited and acknowledged within the text of my work.

This thesis was prepared according to the regulations for postgraduate study by research of the Dublin Institute of Technology and has not been submitted in whole or in part for an award in any other Institute or University.

The work reported in this thesis conforms to the principles and requirements of Institute's guidelines for ethics in research.

The Institute has permission to keep, to lend or to copy this thesis in whole or in part, on condition that any such use of the material of the thesis be duly acknowledged.

Signature _____ *Dejun Liu* _____ Date 05/07/2018 _____

Candidate

Acknowledgements

The work presented in this thesis has been carried out within the Photonics Research Centre of the Dublin Institute of Technology.

There are a number of people who have guided, helped and supported me throughout the course of my PhD study. It is impossible to complete the thesis without their support.

Firstly, I would like to thank Dr. Qiang Wu for giving me this opportunity to study and work with him. I am fortunate to have him as my supervisor. For many times, He helped me out from the doubts, troubles, and anxious mood. I really appreciate for his enthusiasm, encouragement, advice, inspiration, patience, and great efforts for explaining things simply and clearly.

I would also like to thank my co-supervisors, Prof. Yuliya Semenova and Prof. Gerald Farrell. Yuliya is very kind and she helped me overcome many difficulties on the way of pursuing my PhD. Her professional suggestions and encouragement have helped me a lot not just in PhD study but also for my career development. I am always loved and enjoyed talking with her. Gerry has a big wisdom, he taught me a lot on paper writing and structure organizing. I am so appreciated for your kindness that squeezing time from your busy work for revising the manuscript.

Within the Photonic Research Centre, I am also grateful to Dr. Manjusha Ramakrishnan, Dr. Youqiao Ma, Dr. Haoyu Zhao, Mr. Vishnu Kavungal, Mr. Arun Kumar Mallik, Mr. Binghui Li, Mr. Wei Han, Ms. Fangfang Wei, Ms Lei Sun, and Mr. Xiaokang Lian for all the help they provided. It was my pleasure to work with them.

My sincerer gratitude to members of Department of Mathematics, Physics and Electrical Engineering, Northumbria University, Newcastle upon Tyne for providing the help during my visit in Northumbria University. My special thanks to Mr. Rahul Kumar, Mr. Nagesh Lalam, and Dr. Jie Zeng for their hospitality reception during my visit. I really enjoyed working and playing with you guys. Many thanks to Rahul for organizing the memorable UK trip before my leave. My thanks also go to Dr. Junyong Huang (Newcastle university) who provide me the opportunity to work with him in bio-sensing. I also would like to thank Prof. Gang-Ding Peng (University of New South Wales) for providing the experimental guide during his visit in PRC. I would also like to extend my sincere gratitude to my publications' co-authors: Mr. Chao Mei, Ms. Lei Sun, Prof. Jinhui Yuan, Dr. Zhe Kang, Dr. Feng Li, Dr. Zhengyong Liu, Prof. Xiangjun Xin, Prof. Chongxiu Yu, Prof. Shengpeng Wan, Prof. Xingdao He, Prof. Bo Liu, Prof. Changyu Shen and Prof. Hwa-Yaw Tam. I would like to express my gratitude to all the faculty staff for their friendship, technical assistance and support.

I am extremely grateful to my family, including my mother, father, sister, brother-in-law and my wonderful nephew for their unconditional love and support. Finally, I would like to express my highest gratitude to my beloved wife Chengling Lv, for her enormous help, support and encouragement in every aspect of my life. Many thanks to her for bring me a happiness family and a lovely daughter Anna.

Dejun Liu

July 2018

List of publications arising from research

Journal papers

1. **D. Liu**, R. Kumar, F. Wei, W. Han, A. K. Mallik, J. Yuan, S. Wan, X. He, Z. Kang, F. Li, C. Yu, G. Farrell, Y. Semenova and Q. Wu, “High sensitivity optical fiber sensors for simultaneous measurement of methanol and ethanol”, **Sensors and Actuators B: Chemical**, vol. 271, pp. 1–8, 2018. DOI:10.1016/j.snb.2018.05.106.
2. **D. Liu**, R. Kumar, F. Wei, W. Han, A. K. Mallik, J. Yuan, C. Yu, Z. Kang, F. Li, Z. Liu, H.Y. Tam, G. Farrell, Y. Semenova, and Q. Wu, “Highly sensitive twist sensor based on partial silver coated hollow core fiber structure”, **Journal of Lightwave Technology**, vol. 36, pp. 3672–3677, 2018. DOI: 10.1109/JLT.2018.2842111.
3. **D. Liu**, Q. Wu, C. Mei, J. Yuan, X. Xin, A. K. Mallik, F. Wei, W. Han, R. Kumar, C. Yu, S. Wan, X. He, B. Liu, G. D. Peng, Y. Semenova, and G. Farrell, “Hollow Core Fiber Based Interferometer for High Temperature (1000 °C) Measurement”, **Journal of Lightwave Technology**, vol. 36, pp. 1583–1590, 2018. DOI: 10.1109/JLT.2017.2784544.
4. X. Li*, **D. Liu***, R. Kumar*, W. Ng, Y. Fu, J. Yuan, C. Yu, Y. Wu, G. Zhou, G. Farrell, Y. Semenova, and Q. Wu, “A simple optical fiber interferometer based breathing sensor,” **Measurement Science and Technology**, vol. 28, pp. 035105, 2017. DOI: 10.1088/1361-6501/aa577d. (*These authors contribute equally).
5. **D. Liu**, W. Han, A. K. Mallik, J. Yuan, C. Yu, G. Farrell, Y. Semenova, and Q. Wu, “High sensitivity sol-gel silica coated optical fiber sensor for detection of ammonia in water,” **Optics Express**, vol. 24, pp. 24179–24187, 2016. DOI: 10.1364/OE.24.024179
6. **D. Liu**, A. K. Mallik, J. Yuan, C. Yu, G. Farrell, Y. Semenova, and Q. Wu, “High sensitivity refractive index sensor based on a tapered small core single-mode fiber structure,” **Optics Letters**, vol. 40, pp. 4166–4169, 2015. DOI: 10.1364/OL.40.004166.

7. A. K. Mallik, G. Farrell, **D. Liu**, V. Kavungal, Q. Wu, and Y. Semenova, “Silica gel coated spherical micro resonator for ultra-high sensitivity detection of ammonia gas concentration in air,” **Scientific Reports**, vol. 8, pp. 1620, 2018. DOI: 10.1038/s41598-018-20025-9.
8. C. Shen, C. Zhong, **D. Liu**, X. Lian, J. Zheng, J. Wang, Y. Semenova, G. Farrell, J. Albert, and J. F. Donegan, “Measurements of milli-Newton surface tension forces with tilted fiber Bragg gratings,” **Optics Letters**, vol. 43, pp. 255–258, 2018. DOI: 10.1364/OL.43.000255.
9. A. K. Mallik, G. Farrell, **D. Liu**, V. Kavungal, Q. Wu and Y. Semenova, “A Coated Spherical Micro-Resonator for Measurement of Water Vapor Concentration at ppm Levels in Very Low Humidity Environments,” **Journal of Lightwave Technology**, vol. 36, no. 13, pp. 2667–2674, 2018. DOI: 10.1109/JLT.2018.2821272.
10. C. Shen, X. Lian, V. Kavungal, C. Zhong, **D. Liu**, Y. Semenova, G. Farrell, J. Albert, and J. F. Donegan. “Optical spectral sweep comb liquid flow rate sensor,” **Optics letters**, vol. 43, no. 4, pp. 751–754, 2018. DOI: 10.1364/OL.43.000751.
11. F. Wei, A. K. Mallik, **D. Liu**, Q. Wu, G. D. Peng, G. Farrell, and Y. Semenova, “Magnetic field sensor based on a combination of a microfiber coupler covered with magnetic fluid and a Sagnac loop,” **Scientific Reports**, vol. 7, pp. 4725, 2017. DOI: 10.1038/s41598-017-05199-y.
12. L. Sun, Y. Semenova, Q. Wu, **D. Liu**, J. Yuan, T. Ma, X. Sang, B. Yan, K. Wang, C. Yu, and G. Farrell, “High sensitivity ammonia gas sensor based on a silica-gel-coated microfiber coupler,” **Journal of Lightwave Technology**, vol. 35, no. 14, pp. 2864–2870, 2017. DOI: 10.1109/JLT.2017.2701404.
13. L. Sun, Y. Semenova, Q. Wu, **D. Liu**, J. Yuan, X. Sang, B. Yan, K. Wang, C. Yu, and G. Farrell, “Investigation of Humidity and Temperature Response of a Silica Gel Coated Microfiber Coupler,” **IEEE Photonics Journal**, vol. 8, pp. 6805407, 2016. DOI: 10.1109/JPHOT.2016.2619479.
14. A. K. Mallik, **D. Liu**, V. Kavungal, Q. Wu, G. Farrell and Y. Semenova, “Agarose Coated Spherical Micro Resonator for Humidity Measurements,” **Optics Express**, vol. 24, pp. 21216–21227, 2016. DOI: 10.1364/OE.24.021216.

Conference papers

1. **D. Liu**, X. Lian, A. K. Mallik, W. H., F. Wei, J. Yuan, C. Yu, G. Farrell, Y. Semenova, and Q. Wu, “Detection of volatile organic compounds using an optical fiber sensor coated with a sol-gel silica layer containing immobilized Nile red,” The 25th International Conference on Optical Fiber Sensors (OFS-25), Jeju, Korea, 2017. ISSN: 0277-786X, DOI: 10.1117/12.2263671. (poster presentation)
2. **D. Liu**, A. K. Mallik, W. H., F. Wei, L. Sun, J. Yuan, C. Yu, G. Farrell, Y. Semenova, and Q. Wu, “Sol-gel Silica Coated Optical Fiber Sensor for Ammonia Gas Detection”. The 15th International Conference on Optical Communications and Networks (ICO CN 2016), Hangzhou, China, 2016. ISBN-13: 9781509034918, DOI: 10.1109/ICO CN.2016.7875756. (**Oral presentation**)
3. **D. Liu**, W. H., G. Farrell, Y. Semenova, and Q. Wu, “Tapered hetero-core silica fiber structure for relative humidity sensing”. Photonics Ireland 2015, Cork, 2015. (poster presentation)
4. A. K. Mallik, G. Farrell, **D. Liu**, V. Kavungal, Q. Wu and Y. Semenova, “Compact relative humidity sensor based on an Agarose hydrogel coated silica microsphere resonator,” The 25th International Conference on Optical Fiber Sensors (OFS-25), Jeju, Korea, 2017. ISSN: 0277-786X, DOI: 10.1117/12.2263529.
5. F. Wei, A. K. Mallik, **D. Liu**, W. Han, X. Lian, G. Farrell, Q. Wu, G. D. Peng and Y. Semenova, “Simultaneous measurement of both magnetic field strength and temperature with a microfiber coupler based fiber laser sensor,” Jeju, Korea, 2017, The 25th International Conference on Optical Fiber Sensors (OFS-25), Jeju, Korea, 2017. ISSN: 0277-786X, DOI: 10.1117/12.2263678.
6. A. K. Mallik, G. Farrell, **D. Liu**, V. Kavungal, Q. Wu and Y. Semenova, “Porous silica coated spherical microresonator for vapor phase sensing of ammonia at a sub-ppm level,” EWOFs-2016, Limerick, Ireland, 2016. ISSN: 0277-786X, DOI: 10.1117/12.2236486.

7. W. Han, **D. Liu**, X. Lian, A. K. Mallik, F. Wei, L. Sun, G. Farrell, Y. Semenova and Q. Wu, "A spherical-structure-based fiber sensor for measuring simultaneous measurement of both ammonia gas concentration and temperature," Photonics Asia 2016, Beijing, China, 2016. ISSN: 0277786X, DOI: 10.1117/12.2247652.
8. B. Li, **D. Liu**, Yuliya Semenova, Gerald Farrell, Hauping Chan, Qiang Wu, "Investigation on stress/strain sensing characteristics for magnetorheological smart composite material by a SMS fiber structure," TENCON 2015 IEEE Region 10 Conference, Macao, 2015. ISSN: 21593442, DOI: 10.1109/TENCON.2015.7372785.

Contents

High Sensitivity Optical Fiber Interferometric Sensors	I
Abstract	III
Declaration	VI
Acknowledgements	VII
List of publications arising from research	IX
Contents	XIII
List of Figures	XVI
List of Tables	XXI
List of abbreviations and symbols	XXII
Chapter 1 Introduction	1
1.1 Background to the research.....	1
1.1.1 Light propagation in an optical fiber.....	3
1.1.2 Evanescent wave	4
1.1.3 Review of optical fiber sensor types and their applications.....	5
1.1.3.1 Fabry-Perot Interferometer.....	5
1.1.3.2 Mach-Zehnder Interferometer	7
1.1.3.3 Michelson Interferometer.....	8
1.1.3.4 Sagnac interferometer	8
1.1.3.5 SMS interferometer.....	9
1.1.3.5.1 A traditional SMS fiber structure	10
1.1.3.5.2 SMS modifications.....	13
1.2 Aim, Objectives and Achievements	21
1.3 Research methodology	24
1.4 Thesis organization	30
1.5 References	31
Chapter 2 SMS structure based interferometer as a breathing sensor	38
2.1 Introduction.....	39
2.2 Principle and experimental setup	42
2.3 Results and discussion	43
2.4 Conclusion	48

2.5	References	49
Chapter 3 Tapered SCSMF based interferometer sensors		52
3.1	High sensitivity refractive index sensor based on a tapered SCSMF structure.....	54
3.1.1	Introduction	54
3.1.2	Theory and Experiment.....	56
3.1.3	Refractive index sensing performance	59
3.1.4	Humidity sensing performance	62
3.1.5	Conclusion	66
3.1.6	References	66
3.2	High sensitivity sol-gel silica coated optical fiber sensor for detection of ammonia in water.....	69
3.2.1	Introduction	70
3.2.2	Experimental setup and sensor fabrication	73
3.2.3	Results and discussion	75
3.2.4	Conclusion	83
3.2.5	References	84
3.3	High sensitivity optical fiber sensors for simultaneous measurement of methanol and ethanol	86
3.3.1	Introduction	87
3.3.2	Theory and operating principle of the sensors	89
3.3.3	Experiments.....	90
3.3.4	Results and discussion	93
3.3.5	Conclusions	102
3.3.6	References	102
Chapter 4 Hollow core fiber based interferometer sensors		107
4.1	Hollow core fiber based interferometer for high temperature (1000 °C) measurement	109
4.1.1	Introduction	110
4.1.2	Theoretical model and analysis.....	112
4.1.3	Results and discussion	118
4.1.4	Conclusion	126
4.1.5	References	127
4.2	Highly sensitive twist sensor based on partially silver coated hollow	

core fiber structure	131
4.2.1 Introduction	132
4.2.2 Theoretical model and analysis	133
4.2.3 Results and discussion	136
4.2.4 Conclusion	147
4.2.5 Reference.....	147
Chapter 5 Conclusions and future work.....	151
5.1. Conclusions from the research	151
5.2. Future work	156
5.3. References	158
Appendix A Statement of Contribution	160
Appendix B Modes theory	162
Appendix C List of multiple numbering references in this thesis	166

List of Figures

Figure 1. Examples of physical and chemical variables that could be monitored by optical fiber sensors.	2
Figure 2. Typical optical fiber sensor configuration.	3
Figure 3. Schematic diagram of FPI in an optical fiber.	6
Figure 4. Schematic diagram of a typical early MZI.	7
Figure 5. Schematic diagram of a typical MI.	8
Figure 6. Schematic diagram of a typical SI.	9
Figure 7. (a) Schematic diagram of an SMS fiber structure and (b) a simulation result showing the self-imaging property in the MMF with a core diameter of 50 μm ((b) is reproduced from Q. Wu et.al. Opt. Express, vol. 19, no. 9, pp. 7937–7944, 2011).	11
Figure 8. Schematic diagram of modified SMS structure with a (a) SCSMF, and (b) CF.	15
Figure 9. Schematic diagrams of two main types of photonic crystal fibres (PCF): (a) index-guiding PCF and (b) photonic bandgap PCF. (Figure is reproduced from O. Frazão et.al. Laser Photon. Rev., vol. 2, no. 6, pp. 449–459, 2008)	16
Figure 10. Schematic diagram of a tapered fiber.	19
Figure 11. A schematic diagram of the fiber tapering setup.	26
Figure 12. Diagram of the humidity testing setup: (a) an overall view of the humidity testing system; (b) Humidity/Temperature controller; (c) Dehumidification System; (d) Ultrasonic humidification system; (e) Integrated heating system; and (f) Thermoelectric cooling system.	28
Figure 13. (a) Schematic diagram of an SMS fiber structure and (b) a schematic diagram and a photograph of the real prototype of the oxygen mask with embedded SMS.	43
Figure 14. Schematic diagram of the breath monitoring experimental setup.	44
Figure 15. Spectral responses of the SMS breath sensor during inhalation and exhalation process.	45

Figure 16. Experimentally recorded breathing pattern and dynamic threshold in real time (upper plot) and the corresponding breath analysis program response (lower plot) to a regular breathing pattern.	46
Figure 17. Experimentally recorded breathing pattern and dynamic threshold in real time (upper plot) and the corresponding breath analysis program response (lower plot) to an irregular breathing pattern. ...	47
Figure 18. Experimentally recorded breathing pattern and dynamic threshold in real time (upper plot) and the corresponding breath analysis program response (lower plot) to an urgent breathing pattern.	47
Figure 19. Experimentally recorded breathing pattern and dynamic threshold in real time (upper plot) and the corresponding breath analysis program response (lower plot) to a slow breathing pattern.	48
Figure 20. Schematic diagram of (a) micro fiber tapering setup and (b) RI sensing system setup.	59
Figure 21. Measured spectral responses of S-12.5 in different RI ranges: (a) 1.3405-1.3463; (b) 1.3748-1.3837; (c) 1.4304-1.4320.	60
Figure 22. Measured spectral wavelength shift vs. RI for three different tapered SCSMF structure based sensors S-18.8, S-15.0, S-12.5. ...	61
Figure 23. A schematic diagram of the setup for RH sensing experiment. ..	64
Figure 24. (a) Measured spectral responses at different RH values for S-12.5; (b) wavelength shift vs. RH.	65
Figure 25. Schematic diagram of: (a) Tapered SCSMF structure and (b) Experimental setup for ammonia sensing in water.	75
Figure 26. Measured spectral dip shift vs. ammonia concentration in water for S-23 with different coatings.	76
Figure 27. (a) Measured spectral response of S-13.5 at different ammonia concentrations in water; (b) Measured spectral wavelength shift vs. ammonia concentration in water (varies from 2.6 ppm to 65 ppm) for S-13.5 with 8-pass coating; measured data fitted with nonlinear function parameters of which are listed in the inset table.	78
Figure 28. Sensor's response and recovery at different ammonia concentrations.	79
Figure 29. Silica coating morphology at the taper waist. The inset SEM images show (a) cross section at the taper waist; (b) taper transition	

section.	80
Figure 30. Sensor’s response illustrating reversibility and repeatability of measurements for S-13.5 at low and high ammonia concentrations: (a) 2.6 ppm; (b) 65 ppm.	81
Figure 31. Sensor’s sensitivity to a range of ions and molecules including methanol, ethanol, CaCl ₂ , NaCl, Al ₂ (SO ₄) ₃ , NaH ₂ PO ₄ and ammonia in water.	82
Figure 32. Schematic diagram of: (a) TSCSMF, (b) MFC and (c) experimental setup for VOCs sensing.	91
Figure 33. SEM images of (a) TSCSMF, (b) MFC and (c) the cross section of MFC after coating with Nile red immobilized sol-gel silica (recipe I). EDS results on the coating surface of TSCSMF sample are also shown in (a).	93
Figure 34. Normalized measured spectral response at different concentrations of ethanol for (a) TSCSMF with 8-pass coating and (b) MFC with 4-pass coating; Measured corresponding wavelength shifts for different VOCs and concentrations for (c) TSCSMF with 8-pass coating and (d) MFC with 4-pass coating.	95
Figure 35. Spectral response and recovery of (a) TSCSMF based sensor with 8-pass coating and (b) MFC based sensor with 4-pass coating to ethanol and methanol at selected gas concentrations.	97
Figure 36. Sensors’ response and recovery illustrating reversibility and reproducibility of measurements for both sensors at selected ethanol concentrations of 45 ppm and 9 ppm: (a) TSCSMF; (b) MFC.	98
Figure 37. A SEM images of the new TSCSMF sample after coating with recipe II based material.	100
Figure 38. (a) Normalized measured spectral responses at different concentrations of ethanol for a TSCSMF based 4-pass coating sensor; and (b) corresponding measured wavelength shifts for different VOCs and concentrations.	101
Figure 39. (a) A schematic diagram of the proposed SMF28-HCF-SMF28 fiber structure, and (b) a microscope image showing an example of the transition region between the SMF28 and HCF after splicing.	113

Figure 40. Simulated spectral response of the SMF-HCF-SMF fiber structure (a) no diameter variation (b) HCF cladding diameter variation amplitude of ± 10 nm and (c) Q factor vs. amplitude of HCF cladding diameter variation.....	116
Figure 41. (a) Simulated transmission responses of the SMF-HCF-SMF fiber structure at different temperatures; and (b) the corresponding spectral shift of a selected transmission dip versus temperature. .	117
Figure 42. Schematic diagram of the experimental setup for temperature and strain measurements.....	118
Figure 43. Measured transmission spectra for HCF based fiber structure with (a) different lengths of HCF and (b) different output fiber types of SMF and MMF.....	119
Figure 44. (a) HCF based sensor (HCF=3.5 mm) stability test and (b) the corresponding standard deviation plot in one hour period before and after the annealing process at different temperatures.....	121
Figure 45. Wavelength shift versus temperature for HCF based sensor (HCF=3.5 mm): (a) dependencies for different dips within transmission spectrum for the sensor with no pre-annealing process and an example in the inset of the spectral response for dip 3 at different temperatures; (b) dependencies for the same transmission dip for all three different annealing processes and in the inset an example of spectral response at a selected dip for the sensor after annealing at 1005 °C for 65 hours.....	123
Figure 46. Spectral wavelength shift versus applied strain at 21 °C and 503 °C, and spectral responses to various strains at 503 °C for the sensor annealed at 1005 °C for 65 hours.....	125
Figure 47. Influence of the HCF length on temperature and strain sensitivities of the proposed sensor.....	126
Figure 48. (a) A schematic diagram of the proposed SMF-HCF-SMF fiber structure, showing the multiple beams interference inside the hollow core; (b) an SEM image of the used HCF at the cross-section; and (c) a schematic diagram of the HCF cross-section after coating with silver layer.....	134
Figure 49. Simulated spectral responses of the HCF structure with a	

constant reflection coefficient r_1 and varying reflection coefficient r_2	136
Figure 50. Measured spectral responses of the HCF based fiber structures before and after deposition of the silver coating	137
Figure 51. Schematic diagram of the twist sensing setup.	139
Figure 52. (a) Measured transmission spectral responses of the partially silver coated sample (40 s coating) for different input polarization states (angle of linearly polarized light changes from 0° to 22°), and a schematic diagram shows the E-field orientation (b) at different LP state, and (c) at different twist angles.	141
Figure 53. Measured spectral dip strength variations for a range of twist angles by twisting SMF only and HCF only – uncoated HCF sensor (T1).....	143
Figure 54. (a) An example of the measured spectral response of T3 when twisting HCF; (b) measured dip strength change of T3 and (c) T4 for a range of twist angles when twisting SMF only and HCF only – partially silver coated HCF sensor.	144
Figure 55. (a) First order derivative of the measured spectral dip strength change with the twist angle when twisting HCF and (b) sensor's reproducibility demonstration with different samples when twisting the HCF.	146
Figure 56. Cylindrical coordinate system in an optical fiber.	162

List of Tables

Table 1. Sensors sensitivities and linear fit correlative coefficients for different tapered waist diameters.	62
Table 2. Wavelength shift of the spectral dip for the S-13.5 sensor for a series of repeat tests at 2.6 ppm and 65 ppm ammonia concentrations in water.....	81
Table 3. Spectral dips wavelength shifts for the TSCSMF and MFC based sensors for a series of repeat tests at selected ethanol concentrations.	98

List of abbreviations and symbols

BCP	Bromocresol Purple
CF	Coreless Fiber
CMKR_s	Cascaded Microfiber Knot Resonators
CT	Computed Tomography
dB	Decibel
DC	Direct Current
DMAC	N, N-dimethylacetamide
DWDM	Dense Wave Division Multiplexing
EDS	Energy-Dispersive X-ray Spectroscopy
FBG	Fiber Bragg Grating
FP	Fabry-Perot
FPI	Fabry-Perot Interferometer
FSR	Free Spectral Range
HBFs	Highly Birefringent Fibers
HCF	Hollow Core Fiber
HC-PCF	Hollow-Core Photonic Crystal Fibre
IPA	Isopropyl Alcohol
LP	Linearly Polarized
LPGs	Long Period Gratings
MFC	Microfiber Coupler
MI	Michelson Interferometer
MMF	Multimode Fiber
MRI	Magnetic Resonance Imaging
MZI	Mach–Zehnder Interferometer
OFSs	Optical Fiber Sensors
OSA	Optical Spectrum Analyzer
PCF	Photonics Crystal Fibers
PDDA	Poly(diallyldimethylammonium chloride)
PDMS	Polydimethylsiloxane
PMFs	Polarization Maintaining Fibers
POFs	Polymeric Optical Fibers

ppb	Parts per Billion
PVP	Polyvinylpyrrolidone
Q factor	Quality factor
rad	Radians
RH	Relative Humidity
RHU	Relative Humidity Unit
RI	Refractive Index
RIU	Refractive Index Unit
SCSMF	Small Core Singlemode Fiber
SEM	Scanning Electron Microscope
SMF	Singlemode Fiber
SMS	Singlemode-Multimode-Singlemode
SRI	Surrounding Refractive Index
TEC	Thermal Expansion Coefficient
TEOS	Tetraethylorthosilicate
TOC	Thermo-Optic Coefficient
TSCSMF	Tapered Small Core Singlemode Fiber
VOCs	Volatile Organic Compounds

Chapter 1

Introduction

This chapter introduces the background, objectives and key achievements of this research. An overview of the thesis layout is also included.

1.1 Background to the research

Currently optical fibers are widely used in communications over long and short distances for voice, data and a wide variety of internet content. Long distance transmission did not become reality until the early 1970s due to the very high transmission loss (~ 1000 dB/km) of the early optical fibers. In 1966, Charles K. Kao and G. Hockham showed theoretically that the transmission loss introduced by the contaminants in the silica fiber materials could be potentially removed by the purification of silica [1]. In 1970, a low attenuation (~ 20 dB/km) optical fiber was first fabricated by Corning Glass Works [2]. Since then optical fiber telecommunications have experienced a rapid development from the first generation fiber networks using GaAs semiconductor lasers for communications to the present fifth generation networks using techniques such as Dense Wavelength Division Multiplexing (DWDM) to further increase the data rates [3]. Compared to a conventional electrical cable-based communication system, optical fiber based communication system shows a number of advantages such as ultrahigh bandwidth, a long distance transmission capability, immunity to electromagnetic interference, cost effectiveness and light weight [4].

Stimulated in part by the development of semiconductor lasers and low-loss optical fibers for the telecommunications industry, significant efforts have also

been invested in the field of optical fiber sensors (OFSs) since the 1970s [5]. Numerous OFSs have been developed to detect various physical and chemical variables as listed in Figure 1. The ability to be used in a wide variety sensing application is a result of the inherent advantages of optical fiber, such as compact size, light weight, immunity to electromagnetic interference and a demonstrated high sensitivity, a capability to work in harsh environments and remote sensing ability [6]. As a result there are a number of application areas for OFSs for example in environmental monitoring, manufacturing control, monitoring of large civil structures, measurements of gas and liquid concentrations, monitoring of compound materials solidification and detection of biomolecules.

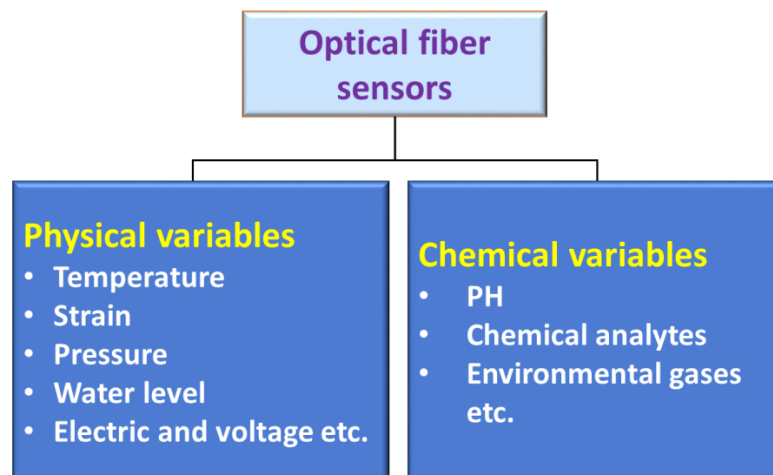


Figure 1. Examples of physical and chemical variables that could be monitored by optical fiber sensors.

In general, a typical optical fiber based sensing system can be divided into four parts as illustrated in Figure 2, including the Light source, Sensor head, Light detector, and Optical path (usually realized by optical fibers). Depending on the specific application, the sensor head could be a bare fiber structure or a functionalized fiber structure with an additional coating layer of sensitive material on the fiber surface. The sensing capability is achieved by allowing the transmitted or reflected light in the sensor head to interact with the surrounding

medium. Due to the change of environmental parameters, molecular binding or chemical reactions within the coating materials, the optical properties of the medium in the vicinity of the sensor head, such as light absorption, reflectance, fluorescence/ phosphorescence and refractive index (RI), can be changed. In turn, by means of a suitable calibration of these variations in the optical properties, the change of the parameters of interest can be determined.

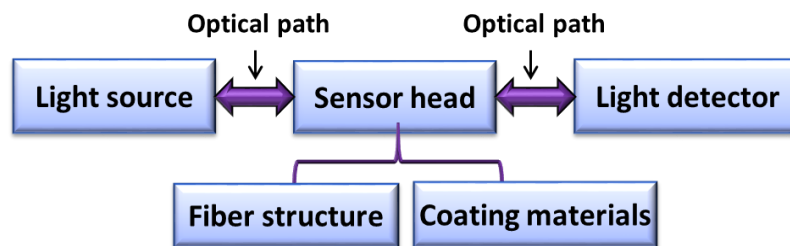


Figure 2. Typical optical fiber sensor configuration.

1.1.1 Light propagation in an optical fiber

A light wave is fundamentally an electromagnetic wave. A complete description of light propagation in an optical fiber is derived from Maxwell's equations, especially for small core fibers, typically less than $8 \mu\text{m}$ in fiber core diameter (so-called singlemode fibers), since geometrical optics cannot be used in a waveguide whose dimensions are comparable or smaller than the transmitted light wavelength. As mentioned above a major strength of optical fiber for communications is its immunity to environmental influences, such as for example temperature and humidity. However for sensing application this strength becomes a disadvantage, since for a sensor head, by definition, there is a need for a strong interaction with the local environment. As a result a wide variety of approaches to fiber modification have been developed that allow the fiber sensor head to interact effectively with the local environment. Many optical fiber

sensors, involve exposing a large proportion of the evanescent field to the testing environment, by means of fiber tapering or removal of the fiber cladding by etching. However such processing steps mean that the approximation of weakly-guided light used for the description of transmission in a standard single mode fiber (SMF) is no longer applicable, since for the standard SMF the RI difference between the core and cladding is less than 1% whereas for an etched or tapered fiber the difference in RI is now dictated by the external environment and can be much larger. Therefore, light propagation within such a modified optical fiber must be calculated by rigorously solving Maxwell's equations. The detailed rigorous solution of Maxwell's equations for this case has been developed in many references, for example in [7-9], and as such will not be covered in this thesis. However, some important equations are listed in the appendix B as a reference.

1.1.2 Evanescent wave

In a standard optical fiber, light is guided within the core via total internal reflection, and such light rays are the so called guided light [9]. In the case of the guided light, although the components of the incident light are totally reflected, the electromagnetic field does not decrease to zero at the interface between the fiber core and cladding, but instead it decays exponentially into the cladding within a short distance from the core-cladding interface. The light wave outside the fiber core is defined as the evanescent wave, and the extended field in the cladding is known as the evanescent field. The penetration depth (d_p) of the evanescent field in the cladding is given by the following equation [9]:

$$d_p = \frac{\lambda}{2\pi\sqrt{(n_1^2 \sin^2 \theta_1 - n_2^2)}} \quad (1.1)$$

where λ is the wavelength of the light, θ_1 is the incident angle at the interface of the fiber core/cladding, and n_1 and n_2 are the RIs of the fiber core and cladding respectively.

1.1.3 Review of optical fiber sensor types and their applications

To date, various approaches to the categorization of OFSs have been reported [10]. It is difficult to categorize all the possible types of fiber sensors due to the scale and rate of development of new sensing schemes. In this work, all the proposed OFSs are based on interferometry and thus this review section focuses on interferometric OFSs. A typical optical fiber based interferometer uses the interference between two beams that propagate through different optical paths either within a single fiber or along two different fibers. Usually, one of the optical paths acts as a reference arm, while the other acts as a sensing arm which is deliberately designed to be easily affected by the appropriate external environmental perturbations. The changes in the output optical signal intensity, phase, wavelength or polarization can be recorded by a suitable analyzer, and hence, with calibration, the measurand can be quantitatively determined. In general, there are five representative types of optical fiber based interferometers: Fabry-Perot, Mach-Zehnder, Michelson, Sagnac interferometers and SMS interferometers [10-11]. Each type of interferometric sensors is briefly reviewed in the following sub-sections, starting with a Fabry-Perot interferometer.

1.1.3.1 Fabry-Perot Interferometer

A Fabry-Perot Interferometer (FPI) is typically formed by placing two mirrors in parallel separated by a short distance, so that the light beams reflected from the front and back mirror surfaces of the FP cavity interfere with each other to

produce a stable interference pattern. For an optical fiber implementation, Figure 3 shows a typical schematic diagram of an optical fiber based FPI where the FP cavity is usually produced by fusion splicing a hollow core fiber between two conventional fibers or by fabricating a cavity within the fiber core with a femtosecond laser. The phase difference between the two reflected light beams is given as

$$\delta = \frac{2\pi}{\lambda} n2L \quad (1.2)$$

where λ is the wavelength of the incident light, n is the RI of the cavity material, and L is the length of the FPI cavity. According to this equation, the phase difference and hence the interference pattern is dependent on the length and refractive index of the cavity, which provides the possibility to measure the change of many environmental parameters such as temperature, strain, pressure and many other parameters [12-16]. The free spectral range (FSR) of the interference spectrum (the space between adjacent interference peaks) is influenced by the length (L) and RI of the cavity. If the cavity RI is fixed, a shorter L gives a larger FSR and hence a wider dynamic sensing range, but with the disadvantage of a poorer resolution due to a decreased quality factor of the interference spectrum.

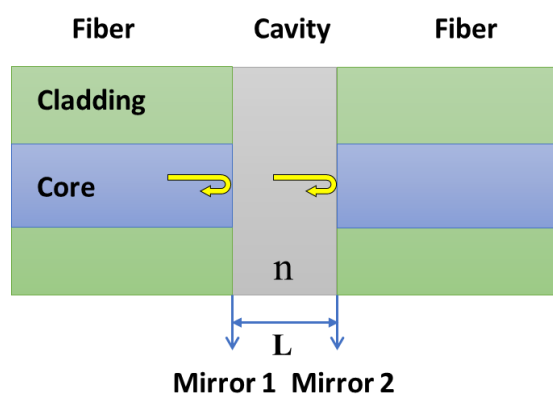


Figure 3. Schematic diagram of FPI in an optical fiber.

1.1.3.2 Mach-Zehnder Interferometer

Mach-Zehnder interferometer (MZI) is a device used to determine the relative phase shift variations between two collimated beams produced by splitting light from a single source. Figure 4 illustrates an early optical fiber based MZI [11], where an incident light is split into two parts by a 3-dB fiber coupler and propagates along two arms (reference arm and the sensing arm), and is then recombined within another fiber coupler and monitored by a light detector. The sensing arm is exposed to the environment and the measurand such as temperature, strain, or RI changes, while the reference arm is kept isolated from any influence by the measurand. The optical properties of the sensing arm are affected by the measurand, this will alter the optical phase difference between the two arms, resulting in the change of the output interference pattern. Assuming a suitable calibration has been made, the change in the measurand can be determined.

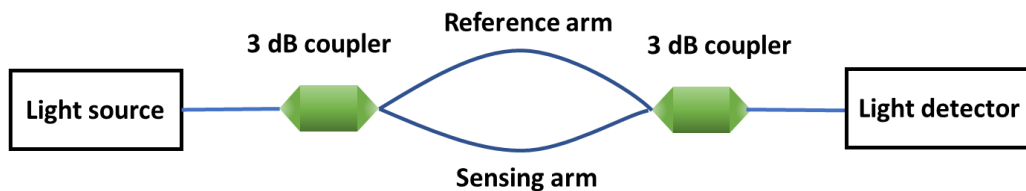


Figure 4. Schematic diagram of a typical early MZI.

e

attention due to their compact nature and robust configurations, which can be realized by using various approaches and fibers such as core mismatch between fibers, a pair of long period gratings (LPGs), air-hole collapsed PCF [11]. The phase shift in these approaches is a result of modal dispersion since light transmission in the cladding and the fiber core will have different optical path lengths due to different RIs.

1.1.3.3 Michelson Interferometer

An Optical fiber based Michelson interferometer (MI) has a similar configuration, operating principle and thus fabrication to that of an MZI. The major difference between the MI and MZI is that the interference in the MZI is produced by transmitted beams while that in the MI is produced by reflected beams. Basically, an MI could be treated as a half of an MZI as shown in Figure 5, where an additional device circulator is used for the measurement of the reflected light interference. Mirrors are introduced at the end of each arm so that light propagating in the two arms (the reference arm and the sensing arm) can be reflected and recoupled to the input fiber by the coupler. Compared to an MZI, an MI is more compact and convenient for installation in practice.

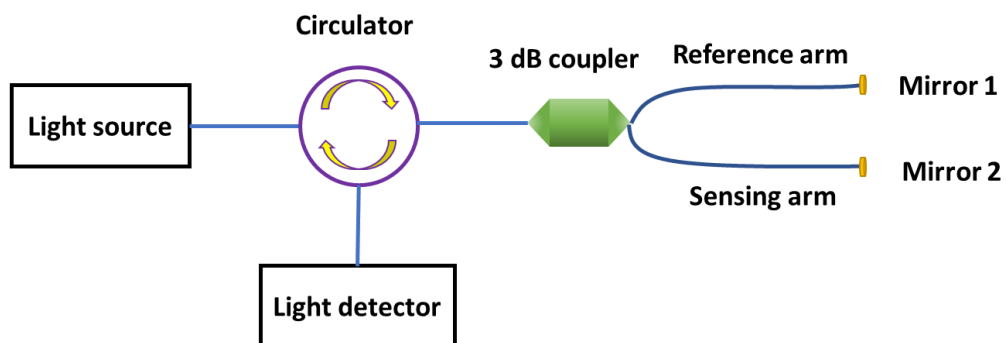


Figure 5. Schematic diagram of a typical MI.

1.1.3.4 Sagnac interferometer

In a typical optical fiber Sagnac interferometer shown in Figure 6, the input light is split into two beams by a 3-dB fiber coupler and the two beams propagate along identical but oppositely directed paths in the fiber loop and are recombined in the coupler. To introduce an optical path difference between the two paths, a birefringent fiber is usually introduced into the fiber loop which is used as the sensor head. The input light polarization state is adjusted by a polarization controller placed before the birefringent fiber section. The output signal is

governed by the interference between the beams propagating along the slow axis and the fast axis of the birefringent fiber. The phase difference between the two beams is given as:

$$\delta = \frac{2\pi}{\lambda}BL, \quad B = |n_f - n_s| \quad (1.3)$$

where B and L are the birefringence and the length of the fiber sensor head respectively and n_f and n_s are the effective indices of the fast and slow modes, respectively [17].

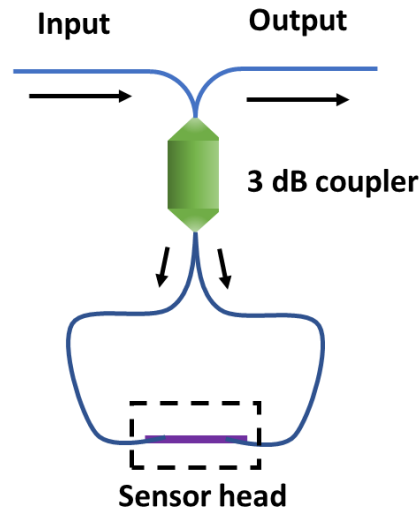


Figure 6. Schematic diagram of a typical SI.

Based on the equation (1.3), a large refractive index difference between the fast and slow modes introduces a large phase difference. Therefore, highly birefringent fibers (HBFs) and polarization maintaining fibers (PMFs) are preferred in order to achieve a high phase sensitivity [18-20].

1.1.3.5 SMS interferometer

In this section an introduction to a singlemode-multimode-singlemode (SMS) fiber structure and its variant forms are provided, which serves as the fundamental fiber structures in the research discussed in this thesis. A SMS fiber

structure is one of the most extensively investigated fiber interferometers for a number of applications, such as refractive index sensing, temperature measurement, displacement monitoring and so on, with a range of advantages including ease of fabrication, high sensitivity, compact size, and potentially low cost [21-24]. In the following sub-sections, a general introduction to traditional SMS fiber structure based optical fiber sensors is given in the first instance and subsequently other modified SMS structures are discussed.

1.1.3.5.1 A traditional SMS fiber structure

A traditional SMS fiber structure is prepared by fusion splicing a section of multimode fiber (MMF) between two SMFs as shown in Figure 7 (a). Since the MMF has a much larger core diameter than that of an SMF, when light propagates from the SMF to MMF, multiple high-order modes will be excited in the core of the MMF. These modes propagate through the MMF with different propagation constants and then re-couple into the output SMF. Interference between these multiple modes occurs and dictates the output spectral response of the SMS fiber structure, which is affected by the surrounding environment.

Self-imaging is a unique feature of multimode interference, which has been widely used in the design of couplers, splitters, combiners, optical switches, and multi/demultiplexers [25-29]. The first theoretical analysis of self-imaging phenomenon was proposed and demonstrated in a planar multimode waveguide in 1995 [30]. Figure 7 (b) shows a simulation example of the light intensity distribution along the MMF with a core diameter of 50 μm [21]. At a certain distance from the entry point, it is found that the light intensity distribution replicates the light distribution at the entry point to the MMF section. This is the so-called imaging point.

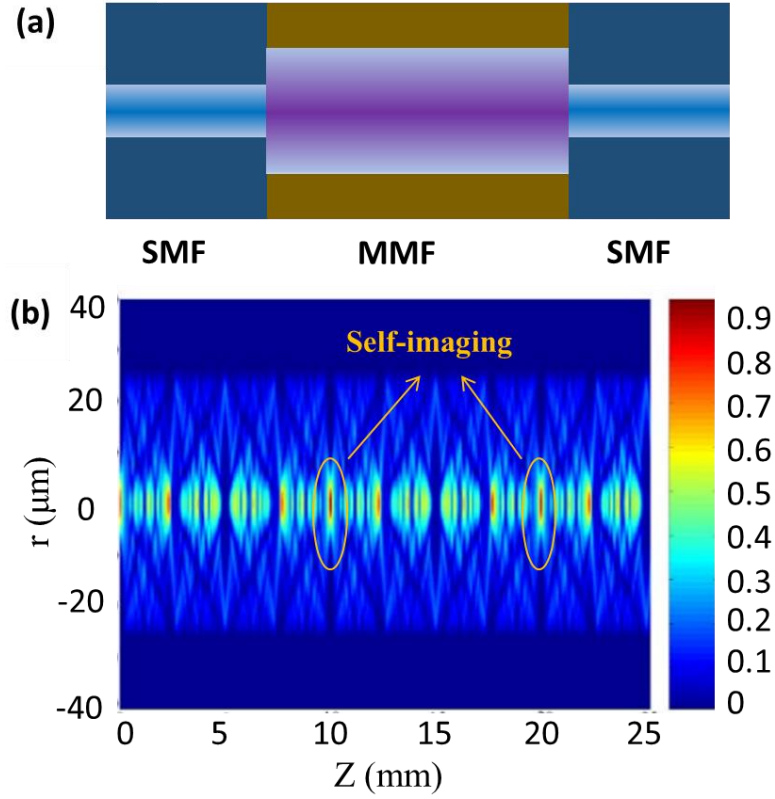


Figure 7. (a) Schematic diagram of an SMS fiber structure and (b) a simulation result showing the self-imaging property in the MMF with a core diameter of 50 μm ((b) is reproduced from Q. Wu et.al. Opt. Express, vol. 19, no. 9, pp. 7937–7944, 2011).

The input field at the MMF can be written as

$$E(r, 0) = \sum_{m=0}^{M-1} b_m \Psi_m(r) \quad (1.4)$$

where $E(r, 0)$ is the eigenmode of the singlemode fiber SMF28, $\Psi_m(r)$ is m_{th} eigenmode of the step index MMF, m is an integer [31]. b_m is the excitation coefficient for each mode, which can be expressed as

$$b_m = \frac{\int_0^{\infty} E(r, 0) \Psi_m(r) r dr}{\int_0^{\infty} \Psi_m(r)^2 r dr} \quad (1.5)$$

The field within the MMF section at a propagation distance z can thus be calculated by

$$E(r, z) = \sum_{m=0}^{M-1} b_m \Psi_m(r) \exp(j \beta_m z) \quad (1.6)$$

where β_m is the propagation constant of each eigenmode within the MMF. The transmitted power to the output SMF thus can be expressed as

$$L_s(z) = 10 \log_{10} \left(\frac{|\int_0^\infty E(r,z)E(r,0)rdr|^2}{\int_0^\infty |E(r,z)|^2 rdr \int_0^\infty |E(r,0)|^2 rdr} \right) \quad (1.7)$$

Assuming β_m and β_n are the longitudinal propagation constants for the m_{th} and n_{th} order modes, then the phase difference between these two modes can be expressed as [32]:

$$\beta_m - \beta_n = \frac{u_m^2 - u_n^2}{2ka^2n_{co}} \quad (1.8)$$

where $u_m = \pi(m - 1/4)$ and $u_n = \pi(n - 1/4)$ are the roots of the Bessel function of zero order, a is the core radius of the MMF, $k = 2\pi/\lambda$ is the free-space wave number, and n_{co} is the refractive index of the fiber core.

Constructive interferences occur when the phase difference between two modes is an integer multiple of 2π .

$$(\beta_m - \beta_n)L = 2\pi N \quad (1.9)$$

where L is the length of the MMF, N is an integer. Then the wavelength of the constructive interference can be derived from equations (1.8) and (1.9):

$$\lambda = \frac{16n_{co}a^2N}{(m-n)[2(m+n)-1]L} \quad (m > n) \quad (1.10)$$

In addition, the FSR between two adjacent modes is

$$\lambda_N - \lambda_{N-1} = \frac{16n_{co}a^2}{(m-n)[2(m+n)-1]L} \quad (m > n) \quad (1.11)$$

As can be seen from equation (1.11), the longer the MMF length, the smaller the spectral FSR.

Since the refractive index of the fiber core, core radius and fiber length are dependent on the surrounding temperature and strain, an SMS based fiber

structure can be easily used as a temperature, displacement, curvature, vibration, strain, voltage, liquid level measurement, and magnetic field sensor [33-37].

1.1.3.5.2 SMS modifications

RI sensing is used as an underlying principle in applications such as measurement of gas and liquid concentrations, compound materials solidification monitoring and biomolecules detection. Due to the large cladding diameter of the MMF, traditional SMS fiber structures cannot be directly used for RI sensing because they do not allow the evanescent field to interact with the surrounding environment. To overcome this limitation, many modified SMS structures have been proposed, for example the use of special fibers, etching or fiber tapering technics.

- **Modified SMS with special fibers**

Small core single mode fiber and coreless fiber

To access the evanescent wave of the traditional SMS fiber structure, one of the commonly used methods is to etch off the cladding of the MMF. However, etching, typically using hydrofluoric acid can introduce a lot of problems including unacceptable fiber surface roughness and also safety concerns. For applications based on monitoring of the surrounding RI variation, an small core single mode fiber (SCSMF) structure is a good candidate since in it the multimode fiber section typical for an SMS structure is replaced with a SCSMF, so that etching is no longer required. This is because in a typical SMF28-SCSMF-SMF28 fiber structure, as shown in Figure 8 (a), cladding modes are excited within the cladding of the SCSMF section due to the core diameter mismatch between the SMF28 and SCSMF. Multimode interference for

these cladding modes occurs within the SCSMF section and sensing is possible since the boundary of the cladding is adjacent to the local environment.

Q. Wu *et al.* [38] provided a comprehensive theoretical analysis for the SMF28–SCSMF–SMF28 structure, and experimentally demonstrated a maximum sensitivity of 1808 nm/RIU (refractive index unit) for a surrounding RI range from 1.324 to 1.431. Subsequently based on this structure, they fabricated a highly sensitive humidity sensor by coating a layer of poly (ethylene oxide) (PEO) on the bare SCSMF surface. The proposed structure can act as a humidity sensor with a high sensitivity of up to 430 nm per relative humidity unit (RHU) in the humidity range from 80% to 83% RH and a sensitivity of 50 nm per RHU in the range from 83% to 95% RH [39]. By employing fiber tapering technology, a refractive index sensor with periodical tapers has also been proposed. An average sensitivity of 226.6 nm/RIU has been experimentally demonstrated in the RI range from 1.33 to 1.38 [40].

In a similar fashion to an SCSMF, Coreless Fiber (CF) is also widely reported for use in this type of modified SMS structure (Figure 8 (b)). Fukano *et al.* proposed a sensitivity enhanced fiber-optic refractive index sensor using multimode interference in a structure composed of a coreless fiber sandwiched between SCSMFs, with a high RI resolution of 8.1×10^{-6} [41]. A coreless fiber based structure has also been widely reported as a humidity sensor [42], a temperature sensor [43], and a curvature sensor [44].

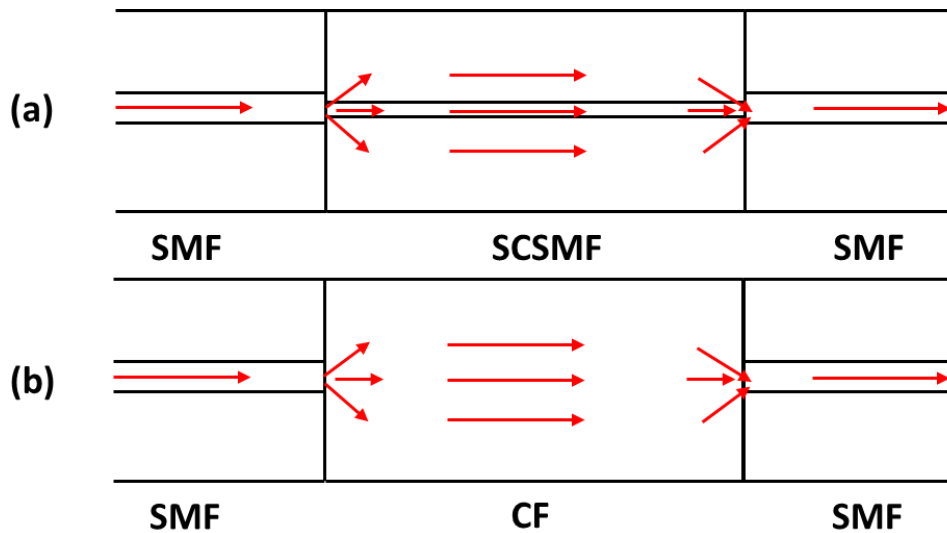


Figure 8. Schematic diagram of modified SMS structure with a (a) SCSMF, and (b) CF.

Photonics crystal fiber

Photonics crystal fiber (PCF), also known as a micro-structured optical fiber, is a relatively new type of fiber which has been attracting intensive investigation since being first reported in 1996 by Knight *et al.* [45]. Depending on the light guidance mechanisms, there are two types of PCF: index-guiding PCF and photonic bandgap PCF (Figure 9) [46]. An index-guiding PCF has a solid core surrounded by a micro-structured cladding (Figure 9 (a)). Due to the presence of air holes in the cladding, the effective RI is higher in the core, hence, light is guided by the same mechanism as in conventional silica fibers. The second type of PCF is known as the hollow-core photonic crystal fibre (HC-PCF) (Figure 9 (b)), where light propagates through the lower refractive index fiber core by the photonic bandgap effect. It is noted that only a specific range of wavelengths which do not fall within the photonic crystal stop bands, can be efficiently confined in the core and propagate along the HC-PCF.

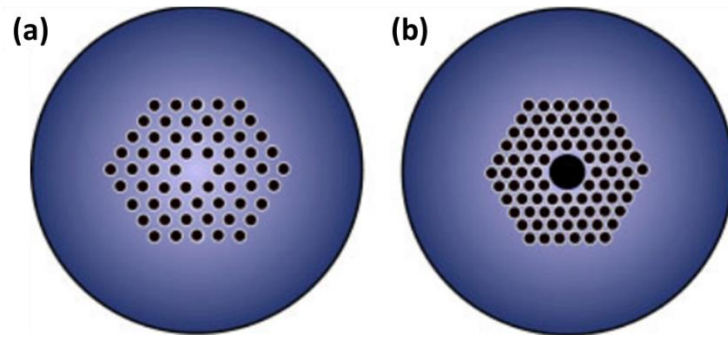


Figure 9. Schematic diagrams of two main types of photonic crystal fibres (PCF): (a) index-guiding PCF and (b) photonic bandgap PCF. (Figure is reproduced from O. Frazão *et al.* *Laser Photon. Rev.*, vol. 2, no. 6, pp. 449–459, 2008)

By incorporating a section of PCF between SMFs, twist/ rotation sensors can be achieved given the fact that PCF usually has an intrinsic linear birefringence. To further improve the sensitivity, most PCF based twist sensors utilize the Sagnac effect. For example, Chen *et al.* [47] reported a highly sensitive torsion sensor by incorporating a segment of novel side-leakage PCF. Other twist sensors using highly birefringent PCF and low-birefringence PCF were also reported [50].

In addition to twist sensing, Villatoro *et al.* [51] reported a highly sensitive wavelength-encoded strain sensor ($\sim 2.8 \text{ pm}/\mu\epsilon$) by splicing a piece of PCF to standard SMFs. The air holes in the PCF were intentionally collapsed over a short region to enlarge the propagating mode of the lead-in fiber which allows the coupling of only two modes in the PCF. Li *et al.* [52] prepared a humidity sensor by coating a layer of polyvinyl alcohol on the surface of a PCF which is spliced between two SMFs with fully collapsed air holes. A sensitivity of $40.9 \text{ pm}/\% \text{RH}$ is achieved within a measurement range from 20% to 95% RH. By using a large-core air-clad PCF, a RI sensor has been demonstrated by Silva *et al.* with a RI resolution of 3.4×10^{-5} [53].

Multicore fibers

As distinct from most fibers, where light is guided within a single core, in a multicore fiber light is guided along multiple cores. In a multicore fiber, if the cores are designed to be close enough to each other, modes transmitting in each of the cores can evanescently couple, and the superpositions of each individual mode are known as the supermodes. Yuan *et al.* [54] investigated the coupling characteristics between SMF and different types of Multicore fibers. A twin-core fiber Michelson interferometer for temperature measurement is reported by Rugeland *et al.* [55], where two supermodes (symmetric/antisymmetric) couple between two cores due to different modes propagation constants. Antonio-Lopez *et al.* [56] reported a high temperature sensor based on a customized multicore (7 cores) fiber structure consisting of a section of multicore fiber between two SMFs. Since the cores are symmetrically distributed, only two supermodes are excited inside the multicore fiber. Compared to the twin-core device, the proposed multicore fiber based sensor shows a significantly improved transmission spectral dip strength (over 30 dB), and hence better detection accuracy. Furthermore, the sensor is polarization independent due to the symmetric core distribution. A sensor for simultaneous measurement of curvature and strain is also realized by using a suspended multicore fiber [57].

Hollow core fiber

A hollow core fiber (HCF) has an air core surrounded by a silica cladding, which is mostly used as a means to incorporate an air-gap microcavity within the fiber to form an FPI for sensing. For example, Lee *et al.* [58] reported a high sensitivity temperature sensor by incorporating an air-gap fiber FPI with a

polymer-filled HCF. Furthermore, they developed a sensor for the measurement of the thermo-optic coefficients of liquids utilizing a fiber Fabry–Perot interferometer fabricated with dual hollow core fibers [59]. Ferreira *et al.* [60] reported a high temperature sensor up to 1000 °C by using an HCF based FPI.

Recently, a HCF based interferometer with high quality factor (Q) transmission spectrum has been demonstrated by simply splicing a short piece of HCF between two SMFs where the ring cladding in such waveguides serves as a built-in Fabry–Perot interferometer [61]. Functionalized HCF structures have been demonstrated for various sensing applications. For example, a humidity sensor has been reported by coating a layer of reduced graphene oxide on the HCF surface [61]; a magnetic field sensor is realized by placing a magnetic gel outside the HCF [62]; a temperature sensor is fabricated by coating a layer of zinc oxide film on the inner surface of the hollow core [63]. However, to date there has been a lack of in-depth analysis of the HCF based structure, and more work is required to better understand this structure and thus develop its applications.

- **Modified SMS utilizing fiber tapering**

Figure 10 shows a typical tapered optical microfiber where the central part with the smallest diameter is called the taper waist. The section between the taper waist and the uniform un-tapered fibers is referred to as the transition region. As can be seen from the figure, there are two transition regions on both sides of the taper waist in a tapered fiber structure. Tapered microfibres can be classified into adiabatic and nonadiabatic. If the taper angle is small enough so that coupling between the fundamental mode and higher order modes is negligible throughout

the length of the tapered fiber, then such a tapered fiber can be considered as adiabatic. If the taper angle is so large that the coupling between the fundamental mode and higher order modes is not negligible, such a tapered fiber is regarded as nonadiabatic. In a nonadiabatic tapered fiber, before the tapered section, light will propagate in the fiber core as the fundamental mode. When light enters the tapered transition region, where the light propagation constant changes along the fiber axis due to the gradually reduced core size, the fundamental mode is partially coupled into the closest higher order modes, and the mode field distribution varies with the change of the fiber core and cladding diameters. The energy transfer from the fundamental mode to the high-order modes is dependent on the rate of change of the fiber diameter with distance along the fiber (tangent value of the local taper angle), which also determines the loss of the transmission light. Therefore, to minimize the mode coupling and hence the power loss, most fiber tapers choose a small taper angle that results in an adiabatic taper.

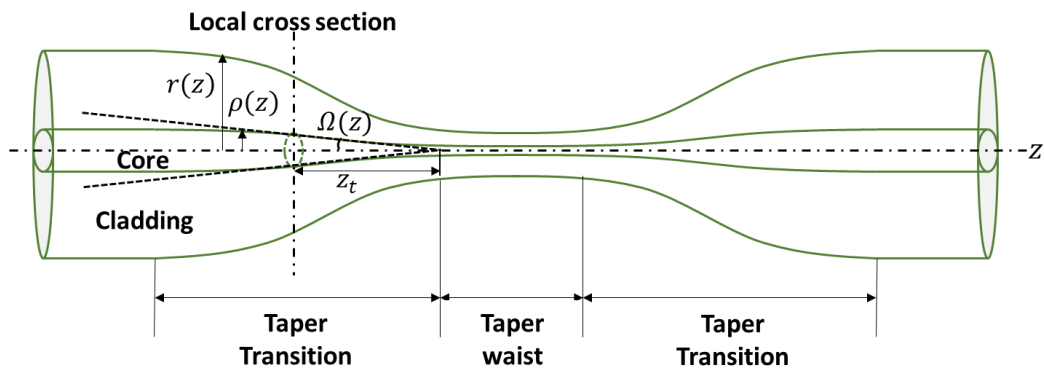


Figure 10. Schematic diagram of a tapered fiber.

Since adiabatic taper types are used for the research described in the thesis, it is useful to briefly introduce the principle which allows an adiabatic taper to be achieved. To achieve an adiabatic taper, the local beat length (z_b) is required to be smaller than the local taper length (z_t) [64]. As illustrated in Figure 10, since the fundamental mode LP_{01} would only effectively be coupled into the second

order mode LP₀₂, z_b and z_t can be expressed as

$$z_t = \frac{\rho}{\tan\Omega} \quad (1.12)$$

$$z_b = \frac{2\pi}{\beta_1 - \beta_2} \quad (1.13)$$

where $\rho = \rho(z)$, $\Omega = \Omega(z)$ are the local core radius and local taper angle respectively and $\beta_1 = \beta_1(r)$ and $\beta_2 = \beta_2(r)$ are the propagation constants of the fundamental mode and the second order local mode respectively. Assuming $z_b < z_t$, we have

$$\tan\Omega < \frac{\rho(\beta_1 - \beta_2)}{2\pi} \quad (1.14)$$

$$\tan\Omega = \left| \frac{d\rho}{dz} \right| \quad (1.15)$$

where $d\rho/dz$ is the rate of change of the local core radius. As can be seen from equations (1.14) and (1.15), the adiabatic tapered fiber can be fabricated by tapering a fiber at a smaller reduction rate in diameter but it results in a longer taper transition section. This equation could be also written as a function of the local cladding radius as

$$\left| \frac{dr}{dz} \right| < \frac{fr(\beta_1 - \beta_2)}{2\pi} \quad (1.16)$$

where $r = r(z)$ is the local cladding radius. To minimize the length of the taper transition in practice, a factor f (between 0 and 1) is introduced to specify by how much the left-hand side of the inequality (1.16) should be less than the right-hand side. The optimal profile is achieved when $f = 1$. The choice of the f value is dependent on the tolerable level of power loss in the specific application. Love and Henry [65] calculated the loss of a tapered SMF could be as low as 0.03 dB when $f = 0.5$. It is worthwhile to note that both the geometry of the transition and waist regions have an influence on the optical properties of

the tapered microfiber. However compared to the taper transition region, the waist region plays the key role in sensing due to a much larger exposed evanescent field.

Zhao *et al.* [66] reported an RI sensor based on a core-offset SMF structure, by further tapering down the offset SMF to a waist diameter of 80 μm . An RI sensitivity of 78.7 nm/RIU was achieved in the range of 1.333–1.374. Wang *et al.* demonstrated a high sensitivity RI sensor with a sensitivity of up to 1900 nm/RIU circa a RI of 1.44 by tapering the SMS structure down to 30 μm [67]. A high temperature sensor up to 1000 $^{\circ}\text{C}$ based on a tapered SMS fiber tip is also proposed by their group with an average sensitivity of 11.4 $\text{pm}/^{\circ}\text{C}$ [68]. André *et al.* [69] proposed tapered coreless fiber sensors for simultaneous measurement of strain and temperature with resolutions of $\pm 5.6 \mu\epsilon$ and $\pm 1.6 ^{\circ}\text{C}$ respectively. Finally Wang *et al.* [70] demonstrated a refractive index sensor with a significantly smaller temperature sensitivity by using a PCF based half-taper probe.

1.2 Aim, Objectives and Achievements

The primary aim of this thesis is to

Develop ultra-high sensitivity and high detection accuracy optical fiber sensors for a variety of measurands, utilizing SMS or modified SMS structures, combined with fiber surface modification techniques.

The specific objectives of this research are as follows:

- 1) Develop highly sensitive fiber sensors for applications in environmental and healthcare areas based on a traditional SMS fiber structure.

- 2) Develop and investigate techniques for increasing the sensitivity of a traditional SMS fiber structure utilizing fiber tapering and special fibers (such as SCSMF and HCF).
- 3) Develop a deeper understanding of such a modified SMS structures and to optimise the structures design to achieve ultra-high sensitivity and high detection accuracy to a range of physical parameters (e.g., refractive index, humidity, temperature, mechanical twist etc.); Experimentally investigate and verify the fiber structure designs and their applications.
- 4) Develop fiber sensor surface modification techniques with different coating materials for the realization of high sensitivity chemical sensors (e.g., detection of ammonia and VOC concentrations).

The key achievements of this research, outlined in this thesis include:

- 1) Developed of a simple novel breathing sensor using a traditional SMS fiber structure. The proposed sensor can differentiate between regular and irregular breath patterns. Compared to conventional electrical sensors, the proposed sensor offers the advantage of a capability of operating in strong magnetic field environments, such as those found in MRI machines.
- 2) A novel tapered SCSMF structure based sensor is proposed with much improved RI sensitivity (>19000 nm/RIU), which is over 10 times higher than that of the un-tapered structure [38]. The proposed structure can be directly used as a humidity sensor even without application of a hygroscopic coating on the fiber surface.
- 3) Based on the proposed tapered SCSMF structure, chemical sensors for ammonia and other VOCs have been developed by functionalising the fiber sensor surface with a silica sol-gel coating and a silica sol-gel coating

containing immobilized Nile red respectively. The theoretical minimum detectable ammonia concentration is as low as 4 ppb which represents an improvement of three orders of magnitude compared to similar refractometric fiber sensors. Furthermore high sensitivity VOCs sensors are demonstrated by coating a mixture of sol-gel silica and Nile red on the surface of two different types of tapered fiber sensors based on a SCSMF and a microfiber coupler (MFC) structure. The minimum detectable concentrations of ethanol and methanol for the MFC based fiber sensor are 77 ppb and 281 ppb respectively. Simultaneous measurement of two different VOC concentrations (ethanol and methanol) is also achieved by functionalising the tapered SCSMF with two different coating material recipes.

- 4) A comprehensive theoretical investigation of a sensor based on a special structure containing HCF has been carried out and verified experimentally. Compared to the previously reported SMS sensors, the HCF structure offers an order of magnitude improvement in spectral Q factor ($\sim 3.3 \times 10^4$) and a larger spectral extinction ratio (~ 26 dB). The HCF based structure can be used for temperature measurements in a wide range from room temperature up to 1000 °C with high sensitivity (up to 33.4 pm/°C). A partial silver coating (6.7 nm-thick) of the HCF surface allows the achievement of a high sensitivity (0.717 dB/°) in the measurements of twist angle, which is the highest twist sensitivity reported for intensity modulation based fiber sensors.

1.3 Research methodology

This thesis is presented as a series of linked journal publications, for this reason this section provides a brief overview of the methodology employed in this research. The methodology employed throughout the research undertaken typically consisted of a sequence of related steps 1 to 4 thus:

1) Development of an in-depth understanding of fundamental principles underpinning the operation of the SMS fiber sensors, relevant fabrication techniques and sensor applications.

Such studies were undertaken throughout the whole period of the PhD study, most frequently involving of the following topics:

- Light propagation characteristics inside various kinds of fibers;
- Operating principles of optical fiber sensors based on different sensing mechanisms;
- Characteristics of fiber coating materials and coating methodologies;
- Sensor fabrication including the corresponding coating materials preparation;
- Applications of optical fiber sensors.

2) Development of appropriate analytical models and numerical simulation program for theoretical predictions, used to assist in the designed experiments.

Based on the analytical and theoretical studies in Step 1, appropriate computer based models were developed, and then numerical predictions and simulations were performed using Matlab. All numerical/ simulation studies were performed on a personal computer with Intel® Core™ i3-3240 CPU @ 3.40 GHz, 4 GB

RAM and 500 GB hard disk storage.

3) Fabrication of novel SMS fiber structure based sensors and materials for surface functionalisation.

- Fibers used in experiments.

Corning[®] SMF-28, Corning[®] 62.5/125 and AFS 105/125 were used as the SMF and MMF in the experiments. SCSMF (SM450) purchased from Thorlabs, and HCF (CAP030/150/24T) purchased from Fiberguide industries were used for the fabrication of modified SMS structures.

- Fiber structure fabrication

The coating layers of the SMF, MMF and SCSMF were stripped with the help of a three-hole fiber stripping tool (FTS4), while the coating layer of the HCF was removed with heat. The stripped fibers were cleaned with Isopropyl alcohol (IPA) and then cleaved using a high precision cleaver from Fujikura (CT-30). A Sumitomo electric fusion splicer and Fujikura 70S splicer were used for joining the fiber sections.

- Fiber tapering setup

A schematic diagram of the fiber tapering setup is shown in Figure 11. The fiber tapering setup consists of two major parts: ceramic microheater (as a heat source) and the pulling rigs. The temperature at the centre of the microheater is controlled by a programmable DC current controller and it should be high enough (usually over 1100 °C) to sufficiently soften the silica fiber. When the fabrication (fusion splicing) of the untapered fiber structure is complete, the structure is inserted into the microheater slit and its ends are fixed onto two

translation stages to ensure the fiber is kept straight. The fiber section intended for tapering is placed into the centre of the heating zone of the microheater. Two programmed linear motorized translation motion stages (ALSQ150B-E01, Zaber) are used to stretch the fiber and precisely control the tapering process. After setting of the initial parameters of the customised computer control program, such as original fiber diameter, required microfibre waist diameter, microheater brushing length etc., and running the programme, microfibres with desired profiles for both the waist and the transition regions are fabricated.

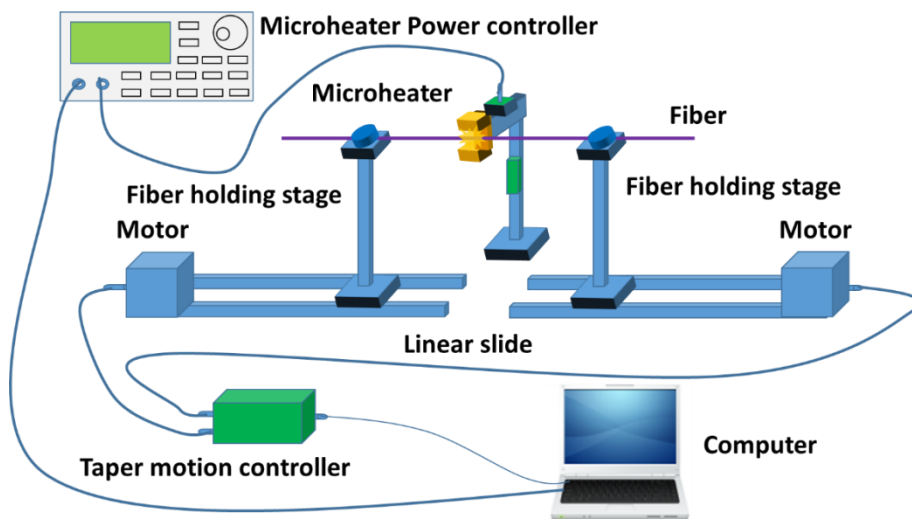


Figure 11. A schematic diagram of the fiber tapering setup.

- Coating materials preparation

All chemicals used in the experiments were purchased from Sigma-Aldrich. Since this thesis is presented as a series of linked journal publications, for the sake of brevity, the details of specific material preparations will be given in the core chapters of the thesis.

- Application of coatings

Two main coating methods were used in the experiments. A dip coating technique was employed in the preparation of chemical sensors while the

sputter-coating method (using a Quorum Technologies Q150RS machine) was employed for deposition of the partial silver coating in the twist sensing experiment.

4) Development of experimental setups for the characterisation of the developed sensors.

- Refractive index measurement

A series of refractive index liquids was prepared by mixing Dimethyl sulfoxide with deionized water. Liquids with different RIs were achieved by changing their mixing ratio, with the exact RI values measured using an Abbe refractometer. The prepared fiber structure was then fixed on a glass slide with a UV glue ensuring that the fiber sensor was always straight and the sensing section was positioned slightly above the slide surface to avoid any physical contact with the glass. During the test, the RI liquid under test was placed on the sensing region of the fiber structure to ensure that it was completely covered with the liquid.

- Relative humidity measurement

A humidity measurement setup (Electrotech Systems Inc., Model 5503-00 with Package F) shown in Figure 12 (a) was used for the humidity tests. The whole setup is composed of Humidity chamber (Model 5503-11), Humidity/Temperature controller (Model 5200-240-230, Figure 12 (b)), Dehumidification system (Model 5461, Figure 12 (c)), Ultrasonic humidification system (Model 5462, Figure 12 (d)), Integrated heating system (Model 5474 and Model 5473-150, Figure 12 (e)), and Thermoelectric cooling system (Model 573-150, Figure 12 (f)). This system can maintain the humidity level within the chamber to better than 0.1% RH from 5% to 100% RH for normal ambient

conditions. The chamber can operate over the temperature range of approximately 10°C to 55°C.

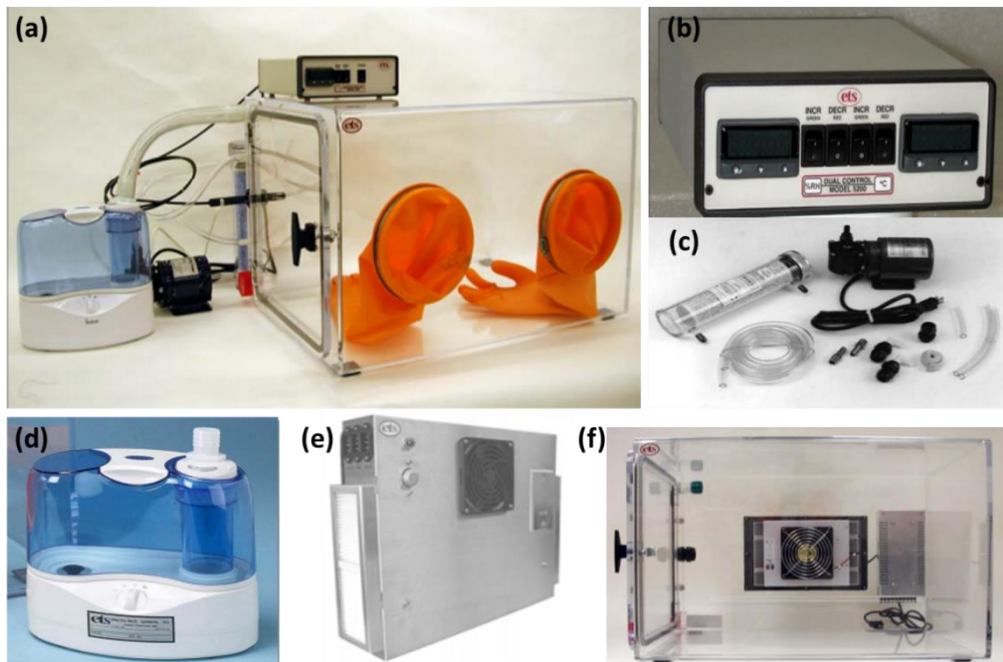


Figure 12. Diagram of the humidity testing setup: (a) an overall view of the humidity testing system; (b) Humidity/Temperature controller; (c) Dehumidification System; (d) Ultrasonic humidification system; (e) Integrated heating system; and (f) Thermoelectric cooling system.

- High temperature measurement

The ceramic microheater used for tapering was also used for the high temperature measurements. The fiber sensor head is placed into the centre of the heating zone of the microheater with its two ends fixed straight on two stages. The temperature of the microheater is controlled by a programmable DC current controller and referenced by a RS Pro Digital Thermometer (206-3738).

- Strain measurement

The fiber sensor is fixed on two translation stages (PT1, purchased from Thorlabs) which have a 25-mm travel range and a 10 μm resolution and is used for applying strain to the fiber sample.

- Twist angle measurement

Twisting of the fiber structure was carried out using two fiber rotators which had a 5° increment (HFR007, purchased from Thorlabs).

- Ammonia sensing in water

The functionalized fiber sensor was placed in a Polydimethylsiloxane (PDMS) mould with a narrow channel (~1.5 mm width) and the water/ammonia sample was pumped through the channel by a peristaltic pump (BT100-02, purchased from Baoding Qili Precision Pump Cooperation) at a speed of 20 r/min (resulting in the liquid flow rate of ~0.008 m/s in the PDMS channel). This enabled the water/ammonia sample to flow slowly through the volume surrounding the sensor. Liquids with different concentrations of ammonia were prepared by mixing an ammonia solution with deionized water. Ammonia concentration is calculated according to a specific ammonia mole ratio to water.

- VOCs concentration measurement

All VOCs tested in the experiment have a high vapor pressure even at room temperature. The VOC vapours are produced from chemical liquids by natural evaporation. Different volumes of VOCs liquids (ethanol/methanol) were dropped into the gas testing cylinder chamber (diameter is 23 mm, height is 11.5 mm) by a micro-syringe to realize different VOCs concentrations. The VOCs liquids evaporate naturally within the chamber, generating VOCs vapors with predictable concentrations which can be calculated according to a specific VOC mole ratio to air in the chamber.

1.4 Thesis organization

This thesis is presented as a series of linked journal publications prepared during the course of PhD study. As the research was carried out within a large research group and different labs in different universities, there are several authors for each publication. A signed statement from all the co-authors is included in Appendix A, confirming that the first author undertook all aspects of the research described in each paper, including preparation and submission of the paper, with the support and advice of the co-authors.

Chapter 1 is this introductory chapter which gives a background and introduction to the optical fiber sensors, research objectives, key achievements, and outlines the structure of the thesis.

Chapter 2 is based on one published journal paper. It presents a study of the optical fiber breathing sensor using a traditional bend SMS fiber structure to monitor breath state, such as a regular or irregular breath.

Chapter 3 is based on three published journal papers. It presents a series of experimental results related to several proposed sensors based on modified SMS fiber structures such as tapered SCSMF. At first, an ultra-high sensitivity RI sensor and a humidity sensor are proposed based on the tapered SCSMF. Then a high sensitivity sensor for ammonia in water is considered, fabricated by coating of the tapered SCSMF surface with a layer of sol-gel silica. Finally, high sensitivity VOCs sensors based on a tapered SCSMF and a microfiber coupler (MFC) are fabricated by coating a layer of silica based material containing immobilized Nile red on both fiber structures.

Chapter 4 is based on two published journal papers. It presents a series of experimental results for the sensor based on a modified SMS fiber structure with

a hollow core fiber. The sensor's spectral characteristics and its temperature performance are investigated both theoretically and experimentally. The proposed sensor structure also proved to be an excellent high temperature sensor. In addition, a high sensitivity twist sensor is demonstrated and fabricated by applying a partial silver coating on the HCF surface.

Chapter 5 summarizes the key results and achievements, draws the conclusions from this thesis and presents a brief overview of potential future research work and directions.

1.5 References

- [1] K. C. Kao and G. A. Hockham, "Dielectric-fibre surface waveguides for optical frequencies," *Proc. Inst. Electr. Eng.*, vol. 113, no. 7, pp. 1151–1158, 1966.
- [2] F. P. Kapron, D. B. Keck, and R. D. Maurer, "Radiation losses in glass optical waveguides," *Appl. Phys. Lett.*, vol. 17, no. 10, pp. 423–425, 1970.
- [3] F. Idachaba, D. U. Ike, and O. Hope, "Future trends in fiber optics communication," *Proc. World Congr. Eng.*, vol. I, pp. 2–6, 2014.
- [4] E. Udd and W. B. Spillman Jr., *Fiber Optic Sensors: An introduction for engineers and scientists*, John Wiley & Sons, 2011.
- [5] R. Bogue, "Fibre optic sensors: a review of today's applications," *Sens. Rev.*, vol. 31, no. 4, pp. 304–309, 2011.
- [6] N. Sabri, S. A. Aljunid, M. S. Salim, R. B. Ahmad, and R. Kamaruddin, "Toward optical sensors: Review and applications," in *Journal of Physics: Conference Series*, 2013, vol. 423, no. 1.
- [7] F. Smith, T. King, and D. Wilkins, *Optics and photonics: an introduction*. John Wiley & Sons, 2007.
- [8] K. Okamoto, *Fundamentals of optical waveguides*. Academic Press, 2006.
- [9] S. Li, C. Li, C. Song, *Optical waveguide theory essentials (Chinese edition)*, Beijing: Electronic Industry Press, 2013.
- [10] K. T. V. Grattan and T. Sun, "Fiber optic sensor technology: an overview,"

Sensors Actuators A Phys., vol. 82, no. 1–3, pp. 40–61, 2000.

- [11] B. H. Lee, Y. H. Kim, K. S. Park *et al.*, “Interferometric fiber optic sensors,” *Sensors*, vol. 12, no. 3, pp. 2467–2486, 2012.
- [12] Y. Du, X. Qiao, Q. Rong *et al.*, “A miniature Fabry-Pérot interferometer for high temperature measurement using a double-core photonic crystal fiber,” *IEEE Sensors J.*, vol. 14, no. 4, pp. 1069–1073, 2014.
- [13] S. Liu, Y. Wang, C. Liao *et al.*, “High-sensitivity strain sensor based on in-fiber improved Fabry-Perot interferometer,” *Opt. Lett.*, vol. 39, no. 7, pp. 2121–2124, 2014.
- [14] F. Guo, T. Fink, M. Han, L. Koester, J. Turner, and J. Huang, “High-sensitivity, high-frequency extrinsic Fabry-Perot interferometric fiber-tip sensor based on a thin silver diaphragm,” *Opt. Lett.*, vol. 37, no. 9, pp. 1505–1507, 2012.
- [15] T. Wei, Y. Han, Y. Li, H.-L. Tsai, and H. Xiao, “Temperature-insensitive miniaturized fiber inline Fabry-Perot interferometer for highly sensitive refractive index measurement,” *Opt. Express*, vol. 16, no. 8, pp. 5764–5769, 2008.
- [16] Y. Zhao, R. Lv, Y. Ying, and Q. Wang, “Hollow-core photonic crystal fiber Fabry-Perot sensor for magnetic field measurement based on magnetic fluid,” *Opt. Laser Technol.*, vol. 44, no. 4, pp. 899–902, 2012.
- [17] H. Y. Fu, H. Y. Tam, L. Y. Shao *et al.*, “Pressure sensor realized with polarization-maintaining photonic crystal fiber-based Sagnac interferometer,” *Appl. Opt.*, vol. 47, no. 15, pp. 2835–2839, 2008.
- [18] J. L. Y. Zhao, D. Wu, R. Lv, “Magnetic field measurement based on the sagnac interferometer with a ferrofluid-filled high-birefringence photonic crystal fiber,” *IEEE Trans. Instrum. Meas.*, vol. 65, pp. 1503–1507, 2016.
- [19] K. Naeem, B. H. Kim, B. Kim, and Y. Chung, “Simultaneous multi-parameter measurement using Sagnac loop hybrid interferometer based on a highly birefringent photonic crystal fiber with two asymmetric cores,” *Opt. Express*, vol. 23, no. 3, p. 3589–3601, 2015.
- [20] B. Song, H. Zhang, Y. Miao *et al.*, “Highly sensitive twist sensor employing Sagnac interferometer based on PM-elliptical core fibers,” *Opt. Express*, vol. 23, no. 12, pp. 15372–15379, 2015.
- [21] Q. Wu, Y. Semenova, P. Wang, and G. Farrell, “High sensitivity SMS fiber

- structure based refractometer--analysis and experiment.," *Opt. Express*, vol. 19, no. 9, pp. 7937–7944, 2011.
- [22] A. M. Hatta, G. Rajan, Y. Semenova, and G. Farrell, "SMS fibre structure for temperature measurement using a simple intensity-based interrogation system," *Electron. Lett.*, vol. 45, no. 21, pp. 20–21, 2009.
- [23] Q. Wu, Y. Semenova, P. Wang, A. M. Hatta, and G. Farrell, "Experimental demonstration of a simple displacement sensor based on a bent single-mode-multimode-single-mode fiber structure," *Meas. Sci. Technol.*, vol. 22, no. 2, pp. 025203, 2011.
- [24] Q. Wu, M. Yang, J. Yuan *et al.*, "The use of a bend singlemode-multimode-singlemode (SMS) fibre structure for vibration sensing," *Opt. Laser Technol.*, vol. 63, pp. 29–33, 2014.
- [25] C. A. J. W. L. Emkey, "Multimode fiber-lens optical coupler," 1987.
- [26] Y. Hibino, F. Hanawa, H. Nakagome, M. Ishii, and N. Takato, "High reliability optical splitters composed of silica-based planar lightwave circuits," *J. Light. Technol.*, vol. 13, no. 8, pp. 1728–1735, 1995.
- [27] A. L. Berman, "Optical combiner collimating apparatus," 1991.
- [28] T. Tanabe, M. Notomi, S. Mitsugi, A. Shinya, and E. Kuramochi, "Fast bistable all-optical switch and memory on a silicon photonic crystal on-chip," *Opt. Lett.*, vol. 30, no. 19, pp. 2575–2577, 2005.
- [29] T. M. K. Nosu, H. Ishio, "Optical multiplexer and demultiplexer," 1981.
- [30] L. B. Soldano and E. C. M. Pennings, "Optical multi-mode interference devices based on self-imaging: principles and applications," *J. Light. Technol.*, vol. 13, no. 4, pp. 615–627, 1995.
- [31] C. Tsao, *Optical fibre waveguide analysis*, Oxford University Press, 1992.
- [32] W. S. Mohammed, A. Mehta, and E. G. Johnson, "Wavelength tunable fiber lens based on multimode interference," *J. Light. Technol.*, vol. 22, no. 2, pp. 469–477, 2004.
- [33] O. Frazão, J. Viegas, P. Caldas *et al.*, "All-fiber Mach-Zehnder curvature sensor based on multimode interference combined with a long-period grating," *Opt. Lett.*, vol. 32, no. 21, pp. 3074–3076, 2007.
- [34] Y. Zhao, X. G. Li, F. C. Meng, and Z. Zhao, "A vibration-sensing system based on SMS fiber structure," *Sensors Actuators, A Phys.*, vol. 214, pp. 163–167, 2014.

- [35] A. M. Hatta, H. E. Permana, H. Setijono, A. Kusumawardhani, and Sekartedjo, "Strain measurement based on SMS fiber structure sensor and OTDR," *Microw. Opt. Technol. Lett.*, vol. 55, no. 11, pp. 2576–2578, 2013.
- [36] A. Hatta, Y. Semenova, G. Rajan, and G. Farrell, "A voltage sensor based on a singlemode- multimode-singlemode fiber structure," *Microw. Opt. Technol. Lett.*, vol. 52, no. 8, pp. 1887–1890, 2010.
- [37] Y. Zhao, Y. Jin, J. Wang, and X. Dong, "Detection of liquid-level variation using a SMS fiber structure," *Optik (Stuttg.)*, vol. 124, no. 18, pp. 3771–3773, 2013.
- [38] Q. Wu, Y. Semenova, P. Wang, *et al.*, "A comprehensive analysis verified by experiment of a refractometer based on an SMF28-small-core singlemode fiber (SCSMF)-SMF28 fiber structure," *J. Opt.*, vol. 13, no. 12, pp. 937–946, 2011.
- [39] Q. Wu, Y. Semenova, J. Mathew, P. Wang, and G. Farrell, "Humidity sensor based on a single-mode hetero-core fiber structure," *Opt. Lett.*, vol. 36, no. 10, pp. 1752–1754, 2011.
- [40] P. Wang, G. Brambilla, M. Ding *et al.*, "Enhanced refractometer based on periodically tapered small core singlemode fiber," *IEEE Sens. J.*, vol. 13, no. 1, pp. 180–185, 2013.
- [41] H. Fukano, T. Aiga, and S. Taue, "High-sensitivity fiber-optic refractive index sensor based on multimode interference using small-core single-mode fiber for biosensing," *Japanese J. Appl. Phys.*, vol. 53, no. 4 SPEC. ISSUE, 2014.
- [42] L. Xia, L. Li, W. Li, T. Kou, and D. Liu, "Novel optical fiber humidity sensor based on a no-core fiber structure," *Sensors Actuators, A Phys.*, vol. 190, pp. 1–5, 2013.
- [43] L. Ma, Z. Kang, Y. Qi, and S. Jian, "Fiber-optic temperature sensor based on a thinner no-core fiber," *Optik.*, vol. 126, no. 9–10, pp. 1044–1046, 2015.
- [44] Y. Qi, L. Ma, Z. Kang, Y. Bai, B. Yin, and S. Jian, "Highly sensitive curvature sensor based on a multicladding fiber sandwiched dual no-core fibers structure," *Appl. Opt.*, vol. 53, no. 28, pp. 6382–6388, 2014.
- [45] J. C. Knight, T. A. Birks, P. S. J. Russell, and D. M. Atkin, "All-silica

- single-mode optical fiber with photonic crystal cladding,” *Opt. Lett.*, vol. 21, no. 19, p. 1547-1549, 1996.
- [46] O. Frazão, J. L. Santos, F. M. Araújo, and L. a Ferreira, “Optical sensing with photonic crystal fibers,” *Laser Photon. Rev.*, vol. 2, no. 6, pp. 449–459, 2008.
- [47] W. Chen, S. Lou, L. Wang, H. Zou, W. Lu, and S. Jian, “Highly sensitive torsion sensor based on Sagnac interferometer using side-leakage photonic crystal fiber,” *IEEE Photonics Technol. Lett.*, vol. 23, no. 21, pp. 1639–1641, 2011.
- [48] H. M. Kim, T. H. Kim, B. Kim, and Y. Chung, “Temperature-insensitive torsion sensor with enhanced sensitivity by use of a highly birefringent photonic crystal fiber,” *IEEE Photonics Technol. Lett.*, vol. 22, no. 20, pp. 1539–1541, 2010.
- [49] O. Frazao, C. Jesus, J. M. Baptista, J. L. Santos, and P. Roy, “Fiber-optic interferometric torsion sensor based on a two-LP-mode operation in birefringent fiber,” *IEEE Photonics Technol. Lett.*, vol. 21, no. 17, pp. 1277–1279, 2009.
- [50] P. Zu, C. C. Chan, Y. Jin *et al.*, “A temperature-insensitive twist sensor by using low-birefringence photonic-crystal-fiber-based Sagnac interferometer,” *IEEE Photonics Technol. Lett.*, vol. 23, no. 13, pp. 920–922, 2011.
- [51] J. Villatoro, V. Finazzi, V. P. Minkovich, V. Pruneri, and G. Badenes, “Temperature-insensitive photonic crystal fiber interferometer for absolute strain sensing,” *Appl. Phys. Lett.*, vol. 91, no. 9, pp. 091109, 2007.
- [52] T. Li, X. Dong, C. C. Chan, K. Ni, S. Zhang, and P. P. Shum, “Humidity sensor with a PVA-coated photonic crystal fiber interferometer,” *IEEE Sens. J.*, vol. 13, no. 6, pp. 2214–2216, 2013.
- [53] S. Silva, J. L. Santos, F. X. Malcata, J. Kobelke, K. Schuster, and O. Frazão, “Optical refractometer based on large-core air-clad photonic crystal fibers.,” *Opt. Lett.*, vol. 36, no. 6, pp. 852–854, 2011.
- [54] L. Yuan, Z. Liu, and J. Yang, “Coupling characteristics between single-core fiber and multicore fiber.,” *Opt. Lett.*, vol. 31, no. 22, pp. 3237–3239, 2006.
- [55] P. Rugeland and W. Margulis, “Revisiting twin-core fiber sensors for

- high-temperature measurements.,” *Appl. Opt.*, vol. 51, no. 25, pp. 6227–32, 2012.
- [56] J. E. Antonio-Lopez, Z. S. Eznaveh, P. LiKamWa, A. Schülzgen, and R. Amezcua-Correa, “Multicore fiber sensor for high-temperature applications up to 1000°C.,” *Opt. Lett.*, vol. 39, no. 15, pp. 4309–4312, 2014.
- [57] R. M. Silva, M. S. Ferreira, J. Kobelke, K. Schuster, and O. Frazão, “Simultaneous measurement of curvature and strain using a suspended multicore fiber,” *Opt. Lett.*, vol. 36, no. 19, pp. 3939–3941, 2011.
- [58] C.-L. Lee, L.-H. Lee, H.-E. Hwang, and J.-M. Hsu, “Highly Sensitive Air-Gap Fiber Fabry–Pérot Interferometers Based on Polymer-Filled Hollow Core Fibers,” *IEEE Photonics Technol. Lett.*, vol. 24, no. 2, pp. 149–151, 2012.
- [59] C.-L. Lee, H.-Y. Ho, J.-H. Gu, T.-Y. Yeh, and C.-H. Tseng, “Dual hollow core fiber-based Fabry–Pérot interferometer for measuring the thermo-optic coefficients of liquids,” *Opt. Lett.*, vol. 40, no. 4, pp. 459–462, 2015.
- [60] M. S. Ferreira, L. Coelho, K. Schuster, J. Kobelke, J. L. Santos, and O. Frazão, “Fabry-Perot cavity based on a diaphragm-free hollow-core silica tube.,” *Opt. Lett.*, vol. 36, no. 20, pp. 4029–31, 2011.
- [61] R. Gao, D. F. Lu, J. Cheng, Y. Jiang, L. Jiang, and Z. M. Qi, “Humidity sensor based on power leakage at resonance wavelengths of a hollow core fiber coated with reduced graphene oxide,” *Sensors Actuators, B Chem.*, vol. 222, pp. 618–624, 2016.
- [62] R. Gao, Y. Jiang, and Y. Zhao, “Magnetic field sensor based on anti-resonant reflecting guidance in the magnetic gel-coated hollow core fiber,” *Opt. Lett.*, vol. 39, no. 21, pp. 6293–6296, 2014.
- [63] H. Sun, H. Luo, X. Wu *et al.*, “Spectrum ameliorative optical fiber temperature sensor based on hollow-core fiber and inner zinc oxide film,” *Sensors Actuators, B Chem.*, vol. 245, p. 423–427, 2017.
- [64] S. W. Harun, K. S. Lim, C. K. Tio, K. Dimiyati, and H. Ahmad, “Theoretical analysis and fabrication of tapered fiber,” *Optik.*, vol. 124, no. 6, pp. 538–543, 2013.
- [65] J. D. Love and W. M. Henry, “Quantifying loss minimisation in

- single-mode fibre tapers,” *Electron. Lett.*, vol. 22, no. 17, pp. 912–914, 1986.
- [66] Y. Zhao, X. Li, and L. Cai, “A highly sensitive Mach–Zehnder interferometric refractive index sensor based on core-offset single mode fiber,” *Sensors Actuators A Phys.*, vol. 223, pp. 119–124, 2015.
- [67] P. Wang, G. Brambilla, M. Ding, Y. Semenova, Q. Wu, and G. Farrell, “High-sensitivity, evanescent field refractometric sensor based on a tapered, multimode fiber interference,” *Opt. Lett.*, vol. 36, no. 12, pp. 2233–2235, 2011.
- [68] P. Wang, M. Ding, L. Bo *et al.*, “Fiber-tip high-temperature sensor based on multimode interference,” *Opt. Lett.*, vol. 38, no. 22, pp. 4617–4620, 2013.
- [69] R. M. André, C. R. Biazoli, S. O. Silva, M. B. Marques, C. M. B. Cordeiro, and O. Frazão, “Strain-temperature discrimination using multimode interference in tapered fiber,” *Photonics Technol. Lett.*, vol. 25, no. 2, pp. 155–158, 2013.
- [70] P. Wang, M. Ding, L. Bo *et al.*, “Photonic crystal fiber half-taper probe based refractometer,” *Opt. Lett.*, vol. 39, no. 7, pp. 2076–2079, 2014.

Chapter 2

SMS structure based interferometer as a breathing sensor

The primary aim of this research is to develop novel applications for fiber sensors based on an SMS structure, particularly in the field of medical care. This chapter contributes to achieving this aim by demonstrating how a simple SMS structure can be used to monitor different human breathing patterns.

Breath is one of the most important human vital signs, hence breath monitoring is widely used in assessing the physiological state of patients. At present the majority of commercial breath sensors available in the market are electronic sensors which cannot be used in strong electromagnetic field and radioactive environments, such as those experienced by patients during Magnetic Resonance Imaging (MRI) diagnostic examinations.

OFSs have intrinsic advantages of fast response, very compact size, immunity to electromagnetic interference and remote sensing capabilities and hence they are good candidates as breathing sensors, for example, for MRI environments.

This chapter presents an experimental demonstration and analysis of the breathing sensor. The sensor is based on the macro bending effect in an SMS structure as means to characterize the human inhalation and exhalation process. Utilizing a customized LabVIEW program for analysis, human breath rate and different kinds of breathing patterns are studied.

A simple optical fiber interferometer based breathing sensor¹

Abstract: A breathing sensor has been experimentally demonstrated based on a singlemode-multimode-singlemode (SMS) fiber structure which is attached to a thin plastic film in an oxygen mask. By detecting power variations due to the macro bending applied to the SMS section by each inhalation and exhalation process, the breath state can be monitored. The proposed sensor is capable of distinguishing different types of breathing conditions including regular and irregular breath state. The sensor can be used in a strong electric/magnetic field and radioactive testing systems such as Magnetic Resonance Imaging (MRI) systems and computed tomography (CT) examinations where electrical sensors are restricted.

Keywords: optical fiber interferometer, optical sensor, breath sensor

2.1 Introduction

Breathing rate is defined as the frequency of breaths taken within a certain amount of time. The typical breathing rate for a healthy adult at rest is between 12 and 20 breaths per minute. It is recognized as one of the most important human vital signs to assess physiological state. A lot of valuable information related to cardiac, neurological and pulmonary conditions can be obtained by analyzing the breathing data [71]. For example, patients' heart and lung diseases can be identified by monitoring breathing in a hospital setting.

¹ X. Li*, D. Liu*, R. Kumar*, W. P. Ng, Y. Fu, J. Yuan, C. Yu, Y. Wu, G. Zhou, G. Farrell, Y. Semenova and Q. Wu, "A simple optical fiber interferometer based breathing sensor," *Measurement Science and Technology*, vol. 28, pp. 035105, 2017. (*These authors have equal contributions to this paper).

There are various methods for breathing measurements such as monitoring the air exhaled through the nose and mouth, or external movement of the thoracic cavity/chest. Based on different working principles, a number of breath sensors have been proposed, such as sensors utilizing humidity or temperature measurements, capnometer and spirometer to monitor breathing behavior [72]. To date, most of the commercialized breath measurement devices are based on electronic sensors, which can be easily influenced by local electric/magnetic fields due to the presence of metallic parts or electrical conductive wires. Consequently, electronic breathing sensors are not suitable for applications associated with strong electric/magnetic environments [73], for example, in a magnetic resonance imaging (MRI) system. However, in many practical situations it is important to monitor the respiratory rate and apnea during the use of MRI.

Fiber optic sensors have intrinsic advantages of fast response, very compact size, immunity to electromagnetic interference and remote sensing capabilities and hence have recently attracted growing attention in applications for breath monitoring. For example, Krehel *et al.* [74] reported a textile-based respiratory sensing system by integrating polymeric optical fibers (POFs) into a carrier fabric to form a wearable sensing system. This respiratory sensing system was placed on a human torso and operated based on the measurement of light intensity changes in POFs as a result of applied pressure. Chen *et al.* [75] proposed a tapered-tip fiber-optic fluorescence oxygen sensor for monitoring human breathing. A POF based force change based breathing rate sensor was reported by Mohanty *et al.* [76]. Kang *et al.* [77] designed an optical fiber-based breathing sensor by applying a multi-layered inorganic nanocluster and polymer

thin films on the distal ends of optical fibers. The sensor detects the variation in relative humidity that occurs between inhaled and exhaled breath and features non-invasive, fast and reliable monitoring of respiratory airflow. Previously, we also reported a humidity based breathing sensor with an agarose infiltrated photonic crystal fiber interferometer [78]. A. Smith *et al.* [79] proposed a non-invasive temperature based respiration sensor to track the breathing cycle during respiratory gating. Respiration sensors utilizing optical fiber bending effects have been regarded as a promising technique and widely investigated [80-83], for example. J. Witt *et al.* [80] developed a monitoring system for continuous measurement of abdominal and thoracic respiratory movement using optical fiber sensors based on macrobending effects. All the above mentioned sensors either suffer from coating fabrication difficulties (time consuming, non-uniformity, limited life time and poor stability) or from a complexity of the sensing system. For example, a fiber Bragg grating (FBG) based breath sensor normally requires monitoring of the Bragg wavelength shift [84], so that the system suffers from a relatively high cost for both interrogation equipment (for example, a tunable laser system) and the FBG sensor itself.

Single mode-multimode-single mode (SMS) fiber structures have been intensively investigated as refractive index (RI), temperature and humidity sensors over the past decade [85-89]. In our previous report, we have proved that an SMS fiber structure is sensitive to macro bending [90-91]. In this letter, for the first time we propose a simple, cost effective breathing sensor based on an SMS fiber structure, which monitors the power variations (instead of wavelength shift for an FBG sensor), showing a fast and good response to different types of breathing conditions (regular, irregular, slow and urgent breath state). The

proposed breath sensor does not require any coating (and hence has long life-time) and is mechanically robust

2.2 Principle and experimental setup

Figure 13(a) shows a schematic diagram of the proposed SMS fiber structure. Light entering from a single mode fiber (SMF) to the multimode fiber (MMF, typically has a step-index profile), excites multiple modes propagating along the MMF section. The field in the MMF section will be distributed symmetrically with the respect to the fiber axis due to the symmetrical refractive index (RI) profile distribution. However, if the MMF is bent, the RI distribution is no longer symmetric so that even a minor bend within the MMF section will introduce significant power variations at the output of the SMS fiber structure [92]. If such an SMS sensor is embedded within a flexible membrane positioned near the patient's mouth, the breathing process will introduce macro bends to the SMS structure and hence will result in light power variations at the output of the SMS fiber structure. By monitoring the light power variation rate, the breathing rate can be measured. In our experiments, a short section of a multimode fiber (AFS105/125Y with a core diameter of 105 μm and cladding diameter of 125 μm) with a length of circa 20 mm was fusion spliced between two singlemode (SMF-28) fibers and attached to a thin plastic film within an oxygen mask as shown in Figure 13(b). The SMS fiber was straight and fixed on a plastic film which was wrapped around two thin support rods. The distance between the SMS based breathing sensor and patient's nose was set to approximately 50 mm and can be adjust in real applications depending on the condition of the patient. When the patient is breathing, the air flowing from their nose/mouth will induce

pressure on the thin plastic film and hence will bend the SMS sensor, resulting in power variations at the output of the sensor.

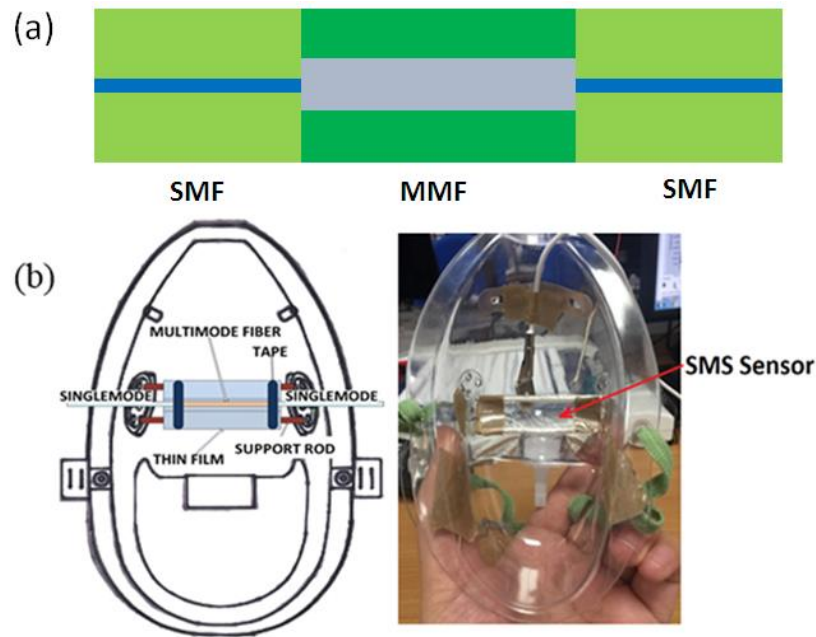


Figure 13. (a) Schematic diagram of an SMS fiber structure and (b) a schematic diagram and a photograph of the real prototype of the oxygen mask with embedded SMS.

Figure 14 illustrates the schematic diagram of the experimental setup used for breath state monitoring. The broadband optical source (Thor Labs S5FC 1550P) used in the experiment is a superluminescent diode with a central wavelength of 1550 nm. Light transmitted through the SMS structure is converted into an electrical signal by a photo-detector and acquired with a data acquisition system (NI-ELVIS II), and then analyzed using a program based on the Lab-View software.

2.3 Results and discussion

Figure 15 illustrates the transmission spectral response during the inhalation and exhalation process. The inhalation and exhalation cycles will result in different forces on the plastic film which in turn will induce different bend radii in the SMS fiber structure (due to the different forces applied to the plastic film) and hence different spectral responses of are recorded at the Photodetector.

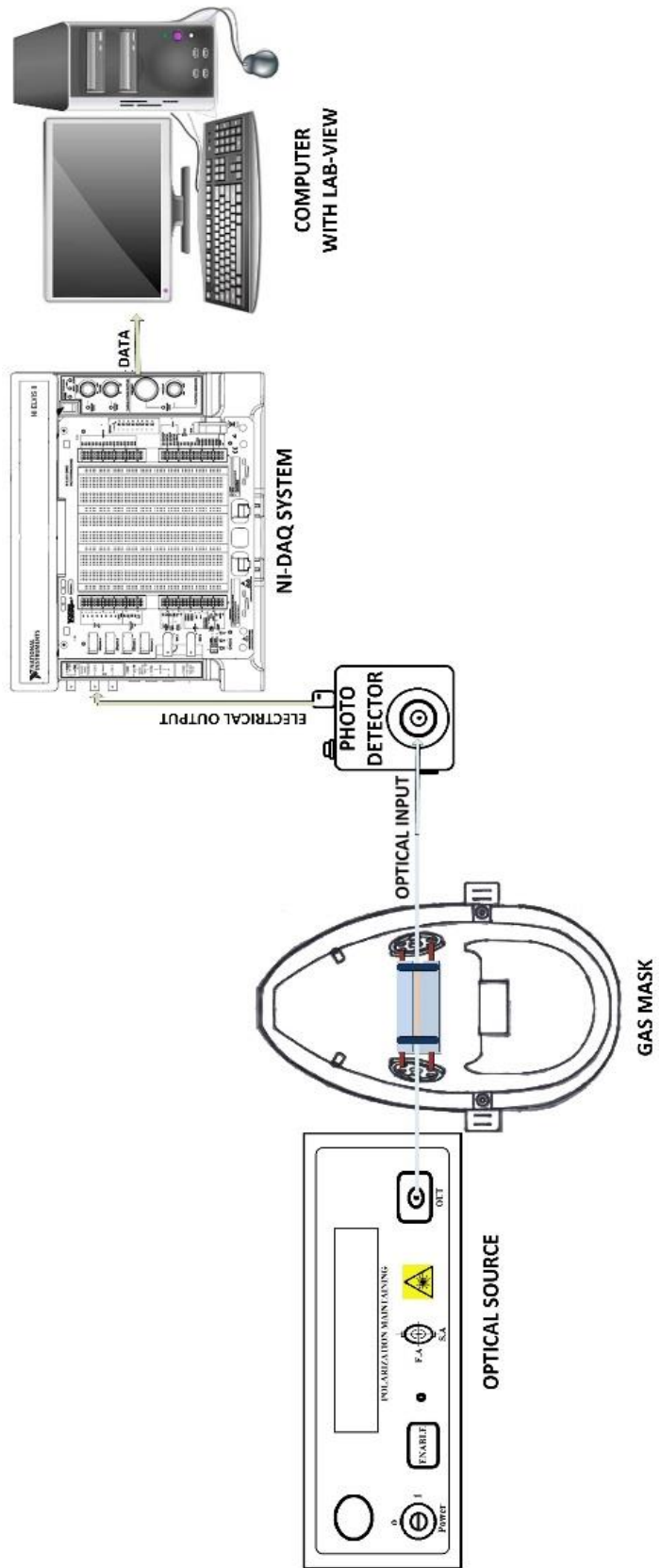


Figure 14. Schematic diagram of the breath monitoring experimental setup.

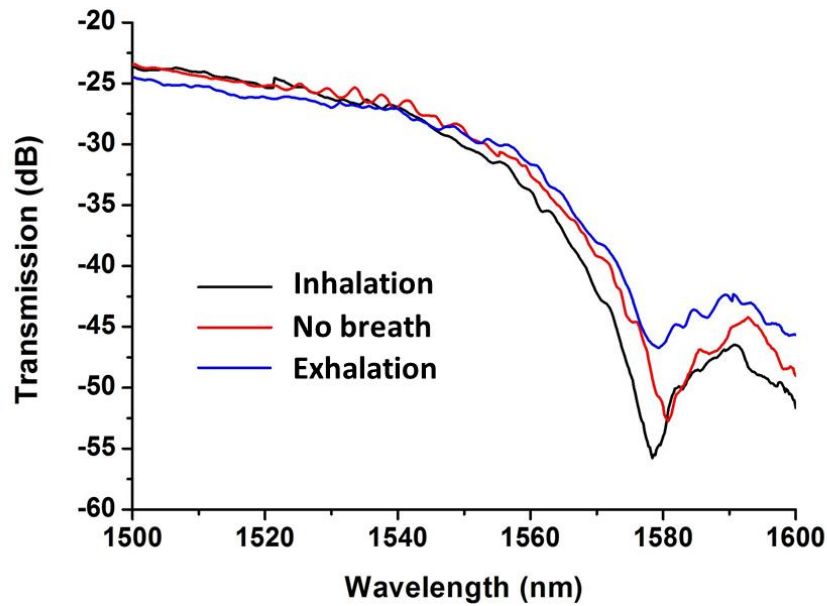


Figure 15. Spectral responses of the SMS breath sensor during inhalation and exhalation process.

Figure 16 illustrates the breath pattern for a regular breath state tested during 30 seconds. The upper plot (black line) shows the voltage change (representing the transmitted power variations detected by the photodetector) corresponding to the real time breathing response. During the exhale cycle, the air flow from the patient's nose will introduce bent to the SMS sensor, resulting in a power variation transmitted to the photodetector, therefore the valleys and peaks of the photodetector response in Figure 16 represent inhalation and exhalation cycles respectively. It is noted that due to the fact that the SMS sensor itself is bound to a thin plastic film it is difficult to ensure it is attached in a perfectly straight position. In addition, the power detected by the photodetector doesn't remain constant due to inevitable environmental fluctuations such as air flow, vibration, incomplete recovery of the plastic film shape, etc. It is hence impossible to set a fixed value as the threshold for determining either inhalation or exhalation states. However, this problem can be solved by setting a dynamic threshold as an average value of all the adjacent peak and valley pairs as shown in Figure 16

with a red spot line plot. The lower plot in the Figure 16 is the breathing cycle indicator calculated from the breathing pattern in the upper plot using a dynamic threshold. In the experiment, we define the value lower than the threshold as breathing state '0' which corresponds to an inhalation, while the value higher than the threshold - as breathing state '1' which corresponds to an exhalation. It is clear from the Figure 16 that the SMS fiber structure based breathing sensor can be easily used for monitoring the regular breathing process.

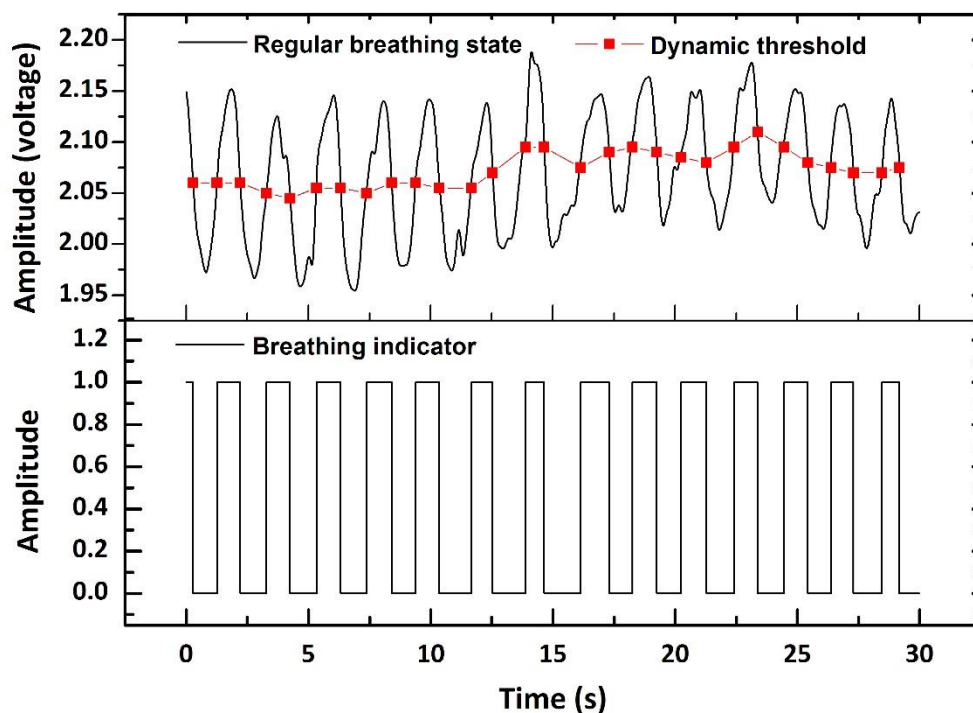


Figure 16. Experimentally recorded breathing pattern and dynamic threshold in real time (upper plot) and the corresponding breath analysis program response (lower plot) to a regular breathing pattern.

In order to demonstrate that our breathing sensor system is capable of monitoring various breathing states in real time, three more breathing behaviors were tested and the corresponding breathing patterns were shown in Figure 17, Figure 18 and Figure 19 with respect to irregular, urgent and slow breathing. One can see that our sensor can easily distinguish between the above different types of breathing conditions.

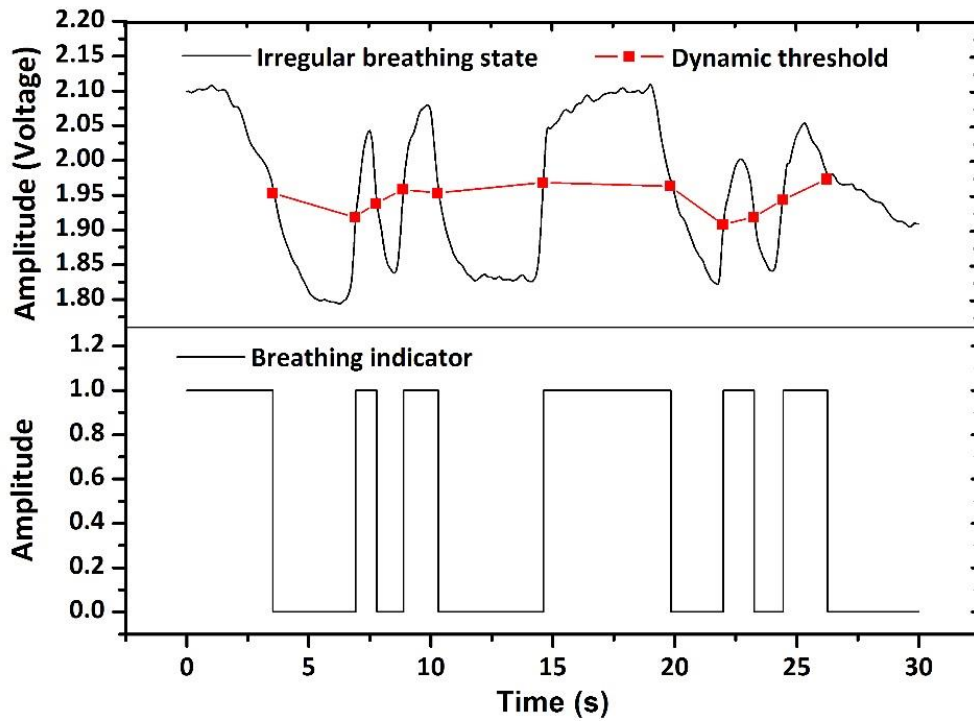


Figure 17. Experimentally recorded breathing pattern and dynamic threshold in real time (upper plot) and the corresponding breath analysis program response (lower plot) to an irregular breathing pattern.

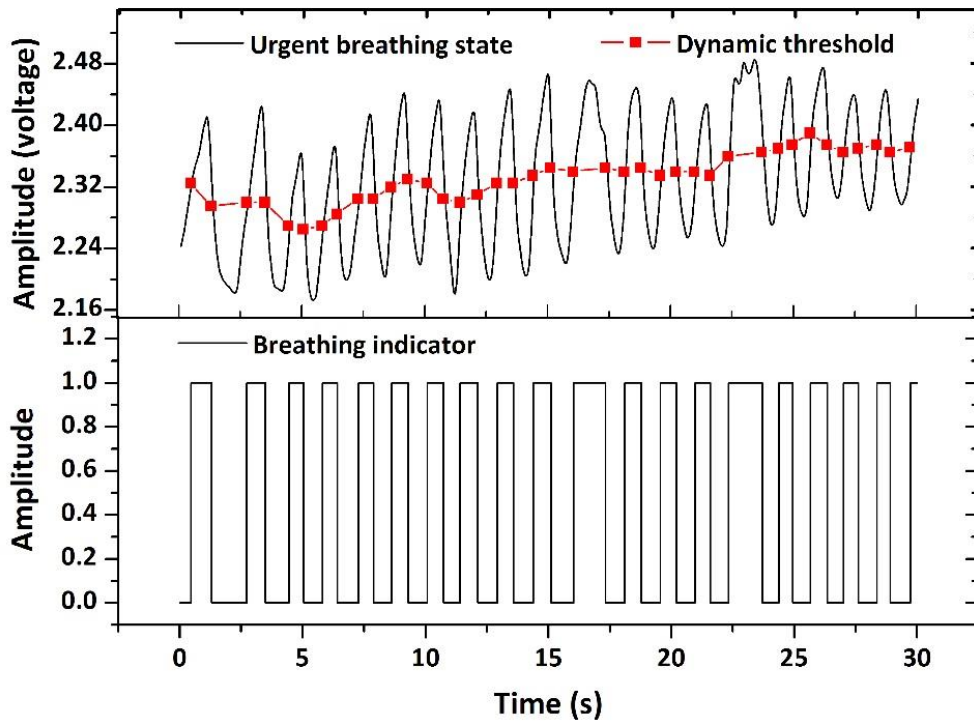


Figure 18. Experimentally recorded breathing pattern and dynamic threshold in real time (upper plot) and the corresponding breath analysis program response (lower plot) to an urgent breathing pattern.

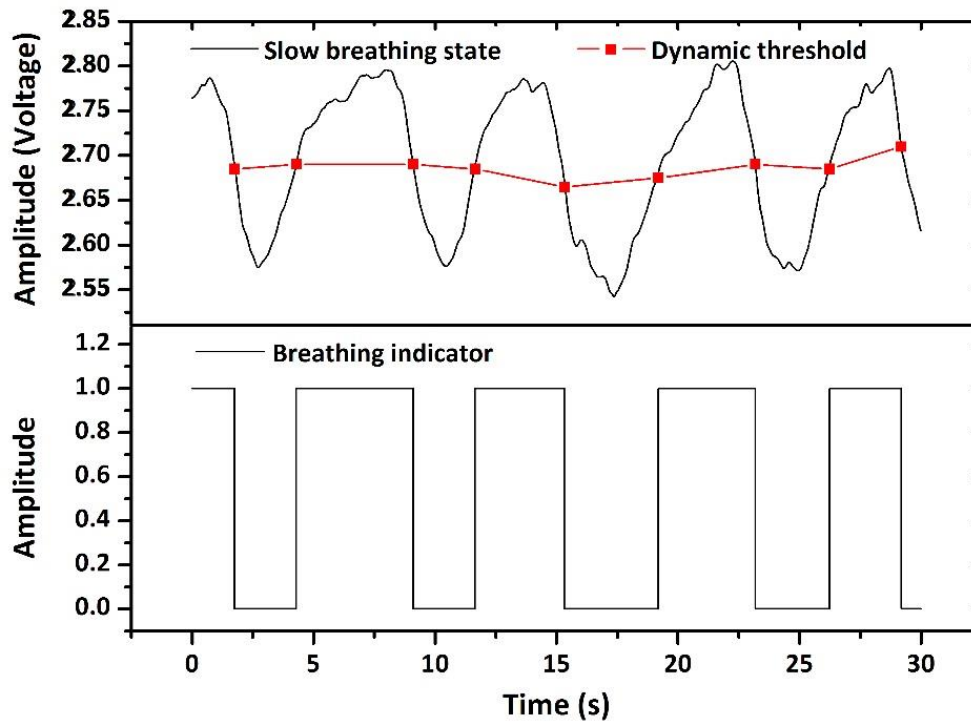


Figure 19. Experimentally recorded breathing pattern and dynamic threshold in real time (upper plot) and the corresponding breath analysis program response (lower plot) to a slow breathing pattern.

2.4 Conclusion

A simple SMS fiber structure based breathing sensor has been proposed. The sensor can be used in strong electric/magnetic field and radioactive environments such as during MRI and CT examinations where traditional electronic sensors could not be applied. By detecting the transmitted optical power variations due to fiber bending resulting from inhalation and exhalation cycles, people's breathing state can be monitored in real time. The proposed sensor can help to easily distinguish between the different types of breathing conditions from a regular and irregular breathing to an urgent and slow breathing patterns. It features advantages of easy fabrication, low cost, fast response and potentially good resistance to environmental contamination.

2.5 References

- [71] S. R. Braun, *Clinical Methods: The history, physical, and laboratory examinations*, Butterworth Publishers, 1990.
- [72] F. Q. Al-Khalidi, R. Saatchi, D. Burke, H. Elphick, and S. Tan, “Respiration rate monitoring methods: A review,” *Pediatric Pulmonology*, vol. 46, no. 6, pp. 523–529, 2011.
- [73] M. F. Dempsey and B. Condon, “Thermal injuries associated with MRI,” *Clinical Radiology*, vol. 56, no. 6, pp. 457–465, 2001.
- [74] M. Krehel, M. Schmid, R. M. Rossi, L. F. Boesel, G. L. Bona, and L. J. Scherer, “An optical fibre-based sensor for respiratory monitoring,” *Sensors (Switzerland)*, vol. 14, no. 7, pp. 13088–13101, 2014.
- [75] R. Chen, F. Formenti, A. Obeid, C. E. W. Hahn, and A. D. Farmery, “A fibre-optic oxygen sensor for monitoring human breathing,” *Physiol. Meas.*, vol. 34, no. 9, pp. N71–N81, 2013.
- [76] L. Mohanty and K. S. C. Kuang, “A breathing rate sensor with plastic optical fiber,” *Appl. Phys. Lett.*, vol. 97, no. 7, pp. 073703, 2010.
- [77] Y. Kang, H. Ruan, Y. Wang, F. J. Arregui, I. R. Matias, and R. O. Claus, “Nanostructured optical fibre sensors for breathing airflow monitoring,” in *Measurement Science and Technology*, 2006, vol. 17, no. 5, pp. 1207–1210.
- [78] J. Mathew, Y. Semenova, and G. Farrell, “A miniature optical breathing sensor,” *Biomed. Opt. Express*, vol. 3, no. 12, pp. 3325–3331, 2012.
- [79] D. H. A. Smith, S. Kim, C. Serago, K. Hintenlang, R. Pooley, “Development of an MR and CT compatible non-invasive temperature based optical fiber respiration sensor for use in radiotherapy,” in *World Congress on Medical Physics and Biomedical Engineering*, 2015, pp. 603–606.
- [80] J. Witt, F. Narbonneau, M. Schukar, K. Krebber, J. Jonckheere, M. Jeanne, D. Kinet, B. Paquet, A. Deprè, L.T. d'Angelo, T. Thiel, R. Logier, “Medical textiles with embedded fiber optic sensors for monitoring of respiratory movement,” *IEEE Sens. J.*, vol. 12, no. 1, pp. 246–254, 2012.
- [81] X. Yang, Z. Chen, C. S. M. Elvin, L. H. Y. Janice, S. H. Ng, J. T. Teo, R. Wu, “Textile fiber optic microbend sensor used for heartbeat and

- respiration monitoring,” *IEEE Sens. J.*, vol. 15, no. 2, pp. 757–761, 2015.
- [82] H. feng Hu, S. jia Sun, R. qing Lv, and Y. Zhao, “Design and experiment of an optical fiber micro bend sensor for respiration monitoring,” *Sensors Actuators, A Phys.*, vol. 251, pp. 126–133, 2016.
- [83] Y. C. H. Di, S. Sun, “Respiration measurement using fibre-optic deformation sensor,” *J. Mod. Opt.*, vol. 64, no. 6, pp. 1–7, 2016.
- [84] L. Dziuda, F. W. Skibniewski, M. Krej, and J. Lewandowski, “Monitoring respiration and cardiac activity using fiber Bragg grating-based sensor,” *IEEE Trans. Biomed. Eng.*, vol. 59, no. 7, pp. 1934–1942, 2012.
- [85] Q. Wu, Y. Semenova, P. Wang, and G. Farrell, “High sensitivity SMS fiber structure based refractometer--analysis and experiment.,” *Opt. Express*, vol. 19, no. 9, pp. 7937–7944, 2011.
- [86] G. Sun, G. Wu, F. Wang, R. Tang, and G. Qiu, “High-stress resistance fiber refractometer based on MMF sandwiched between two SMF half-tapers,” *IEEE Photonics Technol. Lett.*, vol. 28, no. 12, pp. 1336–1339, 2016.
- [87] J. An, Y. Jin, M. Sun, and X. Dong, “Relative humidity sensor based on SMS fiber structure with two waist-enlarged tapers,” *IEEE Sens. J.*, vol. 14, no. 8, pp. 2683–2686, 2014.
- [88] S. M. Tripathi, A. Kumar, R. K. Varshney, Y. B. P. Kumar, E. Marin, and J.-P. Meunier, “Strain and temperature sensing characteristics of Single-Mode–Multimode–Single-Mode structures,” *J. Light. Technol.*, vol. 27, no. 13, pp. 2348–2356, 2009.
- [89] I. Del Villar, A. B. Socorro, J. M. Corres, F. J. Arregui, I. R. Matias, and S. Member, “Optimization of sensors based on multimode interference in Single-Mode – Multimode – Single-Mode structure,” *J. Light. Technol.*, vol. 31, no. 22, pp. 3460–3468, 2013.
- [90] Q. Wu, Y. Semenova, P. Wang, A. M. Hatta, and G. Farrell, “Experimental demonstration of a simple displacement sensor based on a bent single-mode-multimode-single-mode fiber structure,” *Meas. Sci. Technol.*, vol. 22, no. 2, pp. 025203, 2011.
- [91] Q. Wu, M. Yang, J. Yuan, H. P. Chan, Y. Ma, Y. Semenova, P. Wang, C. Yu and G. Farrell, “The use of a bend singlemode-multimode-singlemode (SMS) fibre structure for vibration sensing,” *Opt. Laser Technol.*, vol. 63,

pp. 29–33, 2014.

- [92] R. T. Schermer and J. H. Cole, “Improved bend loss formula verified for optical fiber by simulation and experiment,” *IEEE J. Quantum Electron.*, vol. 43, no. 10, pp. 899–909, 2007.

Chapter 3

Tapered SCSMF based interferometer sensors

In a traditional SMS structure, the evanescent field propagates within the cladding of the MMF having no contact with the surroundings and hence cannot be used for sensing of the surrounding RI. To address this problem, a modified SMS structure based on an SCSMF has previously been proposed and analyzed by a number of researchers [93]. However for an SCSMF structure, the interaction between the evanescent field and the surrounding environment occurs only within a narrow region close to the sensor's surface. This in turn limits the sensor's sensitivity and accordingly its application in bio-chemical fields where detection of a very small variation in RI of the analyte is required.

To address the challenge of low sensitivity in an SCSMF structure, a tapered SCSMF is utilized, with the analysis and applications of this structure described in the three published journal papers which make up this chapter. In summary a highly sensitive RI sensor is developed based on a tapered SCSMF structure, and its applications in relative humidity measurements, for detection of ammonia concentration in water and for monitoring of VOCs concentrations in air are investigated and experimentally demonstrated.

In the first publication presented in this chapter, a highly sensitive RI sensor is fabricated by tapering of an SCSMF based fiber structure. It is noted that a systematic investigation of the tapered SCSMF structure in section 3.1 is based on three fiber tapers with different taper waist diameters and their sensitivity

performance at different RI ranges. The fiber sample with the highest RI sensitivity is then chosen and it is demonstrated that humidity measurement can take place without functionalizing any humidity sensitive (or hygroscopic) material onto the tapered fiber structure surface. It is important to note that the final wavelength shift of the spectral dip at different RH concentrations (especially when RH concentration > 80%) is a combined effect of RI change at the fiber surface, fiber bending and extra strain introduced by the water vapor.

Implementing an optical fiber based chemical sensor will usually require that some additional coating material is deposited on the fiber surface. In the second publication of this chapter the use of sol-gel silica as an effective coating layer for the detection of ammonia concentration in water is proposed and demonstrated for the first time. Fiber samples with different taper waist diameters and coating thickness are investigated under various ammonia concentrations in water. In addition, the repeatability of the measurements and sensor's selectivity to some other ions and molecules in water are tested.

In the last publication that makes up this chapter, sensing of VOCs in air using optical fiber sensors coated with a sol-gel silica layer containing immobilized Nile red is reported based on a tapered SCSMF and a microfiber coupler (MFC). The sensor's performance under different VOCs concentrations is presented. Two different coating recipes are also studied while a 2×2 matrix has been employed to achieve simultaneous measurement of ethanol and methanol concentrations.

3.1 High sensitivity refractive index sensor based on a tapered SCSMF structure²

Abstract: A high sensitivity refractive index (RI) sensor based on a tapered small core singlemode fiber (SCSMF) structure sandwiched between two traditional singlemode fibers (SMF28) is reported. The microheater brushing technique was employed to fabricate the tapered fiber structures with different waist diameters of 12.5 μm , 15.0 μm and 18.8 μm . Experiments demonstrate that the fiber sensor with a waist diameter of 12.5 μm offers the best sensitivity of 19212.5 nm/RIU (RI unit) in the RI range from 1.4304 to 1.4320. All sensors fabricated in this work show good linearity in terms of the spectral wavelength shift versus changes in RI. Furthermore, the sensor with the best sensitivity to RI was also used to measure relative humidity (RH) without any coating materials applied to the fiber surface. Experimental results show that the spectral wavelength shift changes exponentially as the RH varies from 60% to 95%. A maximum sensitivity of 18.3 nm per relative humidity unit (RHU) was achieved in the RH range from 90.4% to 94.5% RH.

OCIS codes: (060.2280) Fiber design and fabrication; (060.2310) Fiber optics; (060.2370) Fiber optics sensors; (060.4005) Microstructured fibers.

3.1.1 Introduction

In the past few decades, optical fiber sensors have been extensively studied for chemical, biotechnology and environmental applications because of their unique properties, such as compact size, immunity to electromagnetic interference,

² D. Liu, A. K. Mallik, J. Yuan, C. Yu, G. Farrell, Y. Semenova, and Q. Wu, "High sensitivity refractive index sensor based on a tapered small core single-mode fiber structure," *Optics Letters*, vol. 40, no. 17, pp. 4166–4169, 2015.

multiplexing and remote sensing capabilities. Optical fiber sensors show great potential for applications involving measurements of gas and liquid concentrations, compound materials solidification monitoring and biomolecules detection, where sensing of the surrounding refractive index (SRI) is used as an underlying principle [94-95]. To date, a number of approaches have been proposed for refractive index (RI) sensors, including fiber Bragg gratings [96], surface plasmon resonance [97], singlemode-multimode-singlemode (SMS) fiber structures [98], optical ring resonators [99] and optical microfiber couplers [100]. Among these structures, SMS fiber structure based sensors are attractive given the additional advantages of low cost and ease of fabrication. However, in order to fabricate an SMS based RI sensor, a chemical etching process is required to remove the cladding from the multimode fiber section, which may introduce some problems with surface roughness of the etched fiber and also safety concerns [98].

A small core singlemode fiber (SCSMF) is a good candidate to replace the multimode fiber section in an SMS fiber structure, with the advantage that etching is not required. In our previous work, we have proved theoretically and experimentally that a SCSMF based fiber structure can act as a high sensitivity RI sensor with a maximum sensitivity of 1808 nm/RIU [93]. Furthermore we have demonstrated as an application of the structure, a humidity sensor utilizing a coating with a maximum sensitivity of 430 nm/RHU [101]. Such sensitivities are still inadequate in some applications, particularly in bio-sensing which require detection of extremely small RI variations. Recently, micro- and nano-fiber sensors have attracted significant interest as they offer a range of advantages such as large evanescent fields, high-nonlinearity, low loss

connections to standard fibers and strong mode confinement [102]. For example, Yadav *et al.* reported an RI sensor with a sensitivity of 1500 nm/RIU based on a tapered single mode fiber [103]. Most recently Zhu *et al.* developed a highly sensitive RI sensor with a sensitivity of 6008 nm/RIU by coating a Al₂O₃ nanofilm on a tapered fiber [104]. Xu *et al.* have demonstrated an RI sensor with a sensitivity of 6523 nm/RIU based on cascaded microfiber knot resonators (CMKRs) with Vernier effect [105].

In this letter, following on our previous work, we report that by tapering the SCSMF structure, an improved RI sensor is possible with a sensitivity that is an order of magnitude higher than the untapered device we reported in [93]. The maximum demonstrated sensitivity was estimated as 19212.5 nm/RIU in the RI range from 1.4304 to 1.4320. All the sensor samples studied in this work show good linearity of the wavelength shift vs. surrounding RI change. Furthermore, one of the sensors, with the highest RI sensitivity, is also chosen to show the tangible benefit of the much improved RI sensitivity is that we show it is possible to implement a relative humidity (RH) sensor without the need for any additional humidity sensitive coatings on the fiber surface.

3.1.2 Theory and Experiment

In a typical SMF28-SCSMF-SMF28 fiber structure, cladding modes are excited within the cladding of the SCSMF section due to the core diameter mismatch between SMF28 and SCSMF. Multimode interference for these cladding modes occurs within the SCSMF section. It is well known, that the propagation constant of the cladding mode (corresponding to effective RI) is influenced by the RI of the surrounding environment. Therefore, a change in the SRI for the sensor will

affect the multimode interference and in turn this will result in changes in the spectral response which can be monitored by an optical spectrum analyzer (OSA). Thus, the SRI can be measured by monitoring the variations of the spectral response assuming a suitable calibration has taken place. This type of sensor is often referred to as an “evanescent sensor”.

Typically an increase in the portion of the evanescent field exposed to the surrounding environment results in a higher sensitivity for the sensor [102]. A simple, non-tapered SCSMF structure has a relatively large diameter (typically 125 μm) resulting in a relatively small portion of the evanescent field being in contact with the surrounding environment and hence such a sensor has relatively low sensitivity. One of the solutions to improve the sensitivity is to use a tapered SCSMF which has a smaller waist diameter as reported in our previous work [106]. In this paper we have systematically investigated the tapered SCSMF structure for RI sensing where the diameters of the SCSMF are tapered down to 12.5 μm , 15.0 μm and 18.8 μm .

In our experiments, a section of SCSMF (SM450) with a length of circa 22.5 mm was fusion spliced between two SMF-28 fibers. The SCSMF section was then tapered using a microheater brushing technique as shown in Figure 20(a) [107]. The fiber tapering process was controlled by a customized computer programmer which realized a synchronized motion of two translation stages with fiber holders applying accurately calculated strain to the SCSMF. By adjusting the input parameters of the computer program, it is possible to achieve different diameters of the tapered fiber, such as the length of the transition regions and minimum waist diameter.

In our experiment, three SCSMF sensor samples were fabricated with

different tapered waist diameters (18.8 μm , 15.0 μm , and 12.5 μm). The waist diameter was measured by a microscope. The prepared sensor samples are referred hereinafter to as S-18.8, S-15.0 and S-12.5. For each taper, the taper waist length is the same with a length of approximately 3.5 mm. The taper transition lengths for S-18.8, S-15.0 and S-12.5 are circa 8 mm, 8.5 mm and 9 mm respectively. In each case the tapered SCSMF structure was fixed on a glass slide ensuring that the fiber sensor was always straight and the sensing section was slightly above the slide to avoid any physical contact with the glass surface.

Figure 20(b) illustrates a schematic diagram of the RI measuring system and a tapered fiber structure, also showing a microscopic image of the taper waist for S-12.5. Light from a broadband light source (Thorlabs S5FC1005S) 1450-1650 nm is launched into the tapered SCSMF structure while the transmitted light is measured by an OSA (Agilent 86142B). The RI liquid can be placed on the glass slide so that the tapered SCSMF fiber section is immersed in the liquid. All tests were conducted at room temperature.

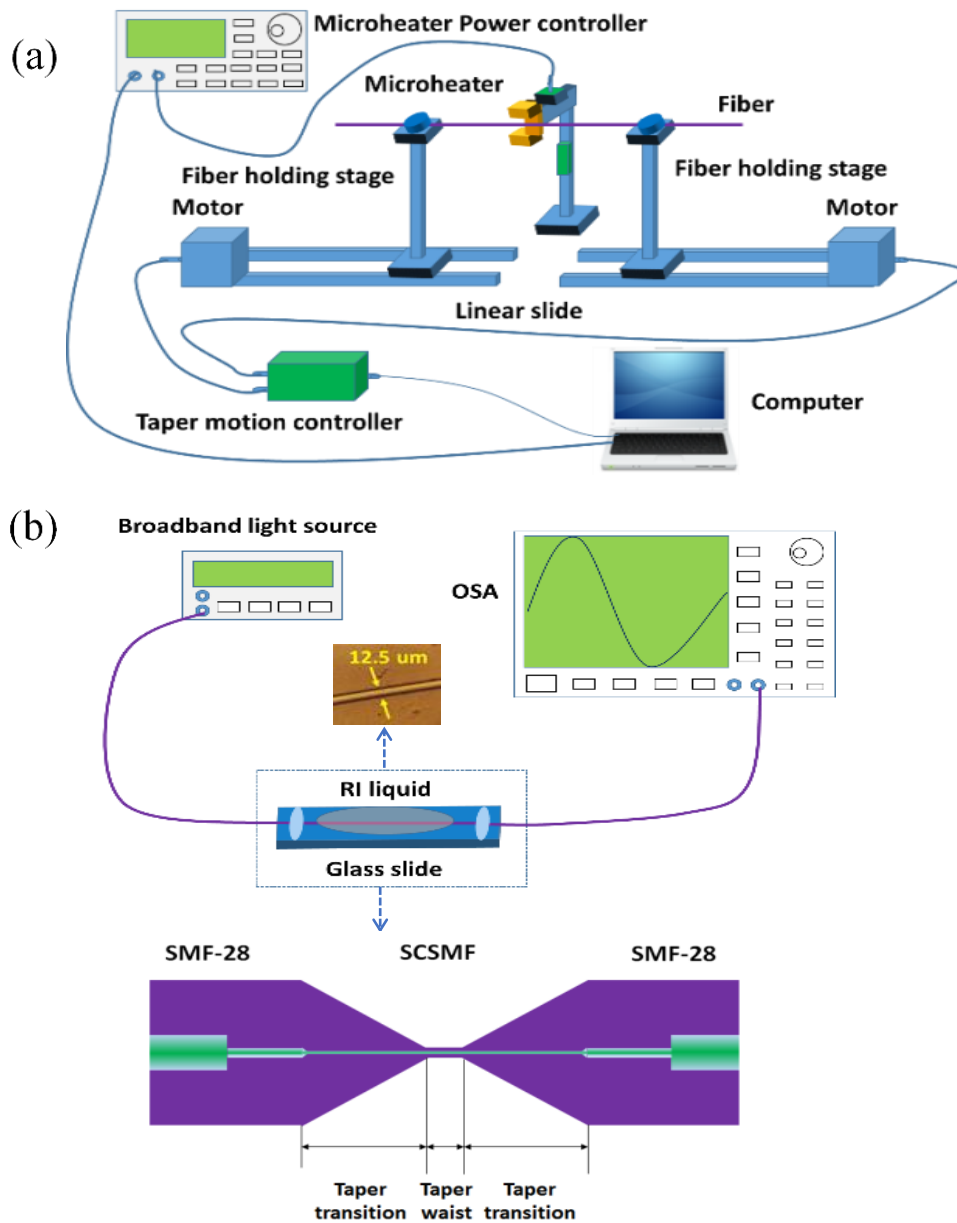


Figure 20. Schematic diagram of (a) micro fiber tapering setup and (b) RI sensing system setup.

3.1.3 Refractive index sensing performance

Figure 21 shows three examples of the measured spectral responses for the S-12.5 sensor immersed in various liquids with calibrated RI values. The RI values ranges are (a) 1.3405 to 1.3463, (b) 1.3748 to 1.3837 and (c) 1.4304 to 1.4311. The spectral dip moves monotonically towards longer wavelengths as the SRI increases in every case. The S-18.8 and S-15.0 sensors have different

spectral responses but the direction of the wavelength shift with increasing SRI is the same. The spectral responses for the S-18.8 and S-15.0 sensors are not shown here for the sake of brevity.

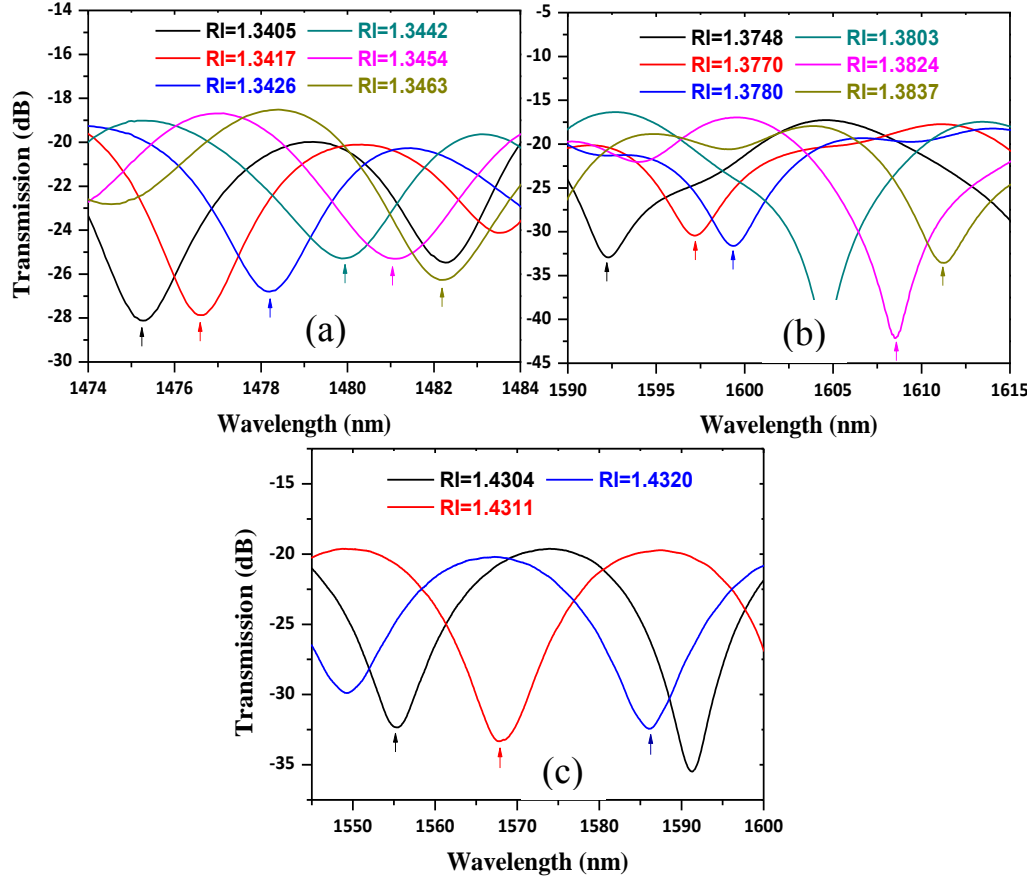


Figure 21. Measured spectral responses of S-12.5 in different RI ranges: (a) 1.3405-1.3463; (b) 1.3748-1.3837; (c) 1.4304-1.4320.

As shown in Figure 22 and Table 1, for all the three samples, the linear correlative coefficients R^2 are greater than 0.992, which indicates the wavelength shift exhibits good linear relationship with the RI change over a small RI range. The maximum sensitivities for S-18.8, S-15.0, S-12.5 are 4722.9 nm/RIU (RI=1.4249-1.4319), 8353.6 nm/RIU (RI=1.4256-1.4312) and 19212.5 nm/RIU (RI=1.4304-1.4320), respectively. Taking into account that the OSA has a wavelength resolution of 0.01 nm, the RI sensor based on S-12.5 has a RI resolution of 5.025×10^{-7} which to the best of our knowledge is significantly

higher than previously reported [108-112]. It is noted that in this study, the central wavelength of the spectral dip is determined as the 3 dB mean wavelength, which is a more reliable parameter compared to the central peak wavelength.

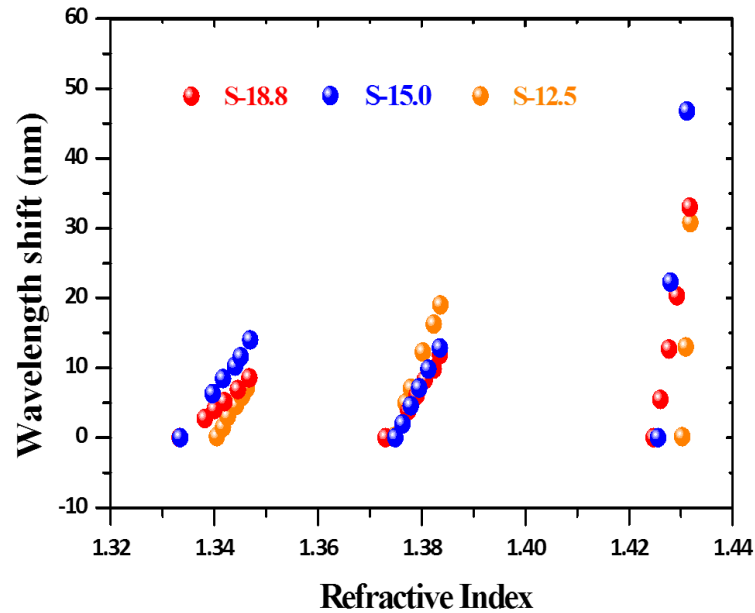


Figure 22. Measured spectral wavelength shift vs. RI for three different tapered SCSMF structure based sensors S-18.8, S-15.0, S-12.5.

Although the proposed sensor has very high RI sensitivity, this sensor suffers from the disadvantage of a narrow RI measurement range due to its limited free spectral range (typically 15 nm depending on the RI measurement range). One possible solution to overcome this problem is to combine a relatively low sensitivity RI sensor (for example, an SCSMF sensor without tapering) with the proposed tapered SCSMF. The lower sensitivity RI sensor would then be used to determine the approximate RI range of the analyte. Then the appropriate sensor would be applied to measuring a highly accurate RI value for the analyte.

Table 1. Sensors sensitivities and linear fit correlative coefficients for different tapered waist diameters.

Sensors	S-18.8			S-15.0			S-12.5		
RI range	1.3333	1.3775	1.4249	1.3334	1.3749	1.4256	1.3405	1.3748	1.4304
	-	-	-	-	-	-	-	-	-
	1.3468	1.3836	1.4319	1.3469	1.3835	1.4312	1.3463	1.3837	1.4320
Linear fit correlative coefficient	0.9956	0.9924	0.9968	0.9958	0.9989	0.9940	0.9949	0.9992	0.9990
Sensitivity (nm/RIU)	634.8	1313.1	4722.9	1038.5	1496.5	8353.6	1198.3	2123.6	19212.5

It is noted that reducing the tapered waist diameter of such a fiber sensor might result in a higher RI sensitivity. However, a tapered fiber with a smaller waist diameter is more fragile compared to that of a larger waist diameter. Moreover, the tapered SCSMF sensor with a smaller waist diameter has a smaller free spectral range which results in a smaller RI measurement range. By considering the tradeoff between the measurement range, sensitivity and mechanical stability of the sensor, a minimum tapered waist diameter of 12.5 μm was selected for our experiments.

3.1.4 Humidity sensing performance

Most of the optical fiber based evanescent RH sensors reported to date require the coating an additional humidity sensitive (or hygroscopic) material on the surface of the fiber sensor. Such humidity sensitive materials include polyvinyl alcohol (PVA), polyimide (PI), poly (methyl methacrylate) (PMMA) and nano-porous TiO_2 and SiO_2 films [113-115]. The underlying operating principle of these types of RH sensors is that the RI of the hygroscopic material coated on the surface of the sensor changes in response to changes in the humidity. The RI

change results in a sensor spectral response variation and hence the RH can be determined. However, sensors coated with humidity sensitive materials suffer from a number of disadvantages: 1) the coating of the fiber with a humidity sensitive material requires an additional fabrication step which is difficult to control (usually due to the layer non-uniformity, etc.); 2) the coating materials have limited lifetimes and are subject to contamination.

Dispensing with the need for a coating for an RH sensor is a very useful development and given the increase in RI sensitivity of the underlying sensor demonstrated already, here we explore whether it is possible to implement an RH sensor without the need for any additional humidity sensitive coatings on the fiber surface.

A schematic diagram of the RH testing system is shown in Figure 23. In the experiment, an RI sensor with a tapered waist diameter of 12.5 μm was placed in a RH chamber with normal air pressure (Electro Tech Systems inc., Model 5503-00 with Package F). Both the humidity and temperature can be controlled by using this system. The maximum available resolution of this RH control system is 0.1 RH% and all tests were carried out at a fixed temperature of 20.5 ± 0.5 $^{\circ}\text{C}$.

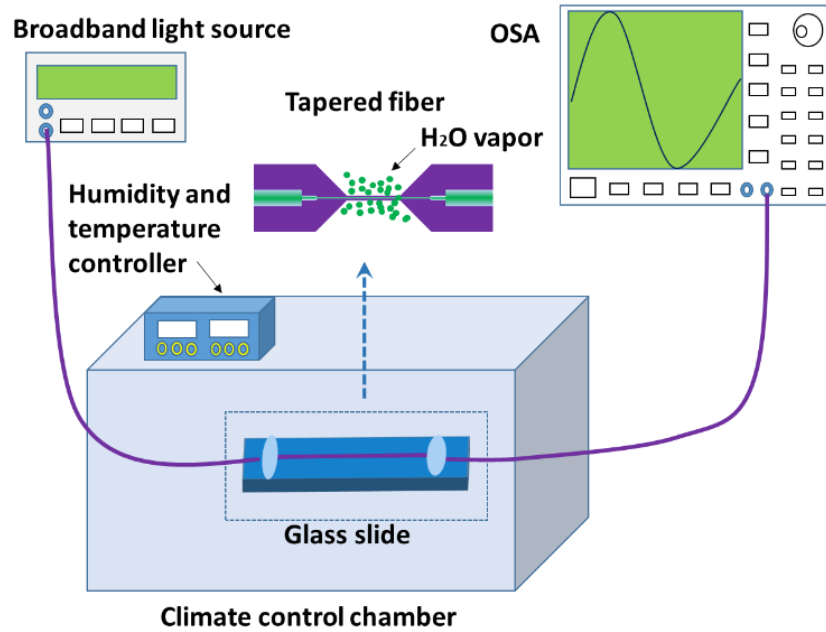


Figure 23. A schematic diagram of the setup for RH sensing experiment.

As shown above, sample S-12.5 has the highest RI sensitivity and hence it was selected for this RH sensing demonstration. In our experiments, the RH within the chamber was increased gradually from 60% to 95% RH. Figure 24(a) shows the spectral response of the sensor at different RH values. It is observed that as the RH increases from 60% to 95%, the central wavelength of the spectral dip shifts to a longer wavelength monotonically. The wavelength shift vs. RH change is plotted in Figure 24(b). It is clear that the wavelength shift changes exponentially with the increase of RH in the RH range from 60.4% to 94.5%. The total wavelength shift from 60.4% to 94.5% is circa 2.0 nm and the maximum sensitivity of 18.3 nm/RHU was achieved in the RH range from 90.4% to 94.5%. The RH sensitivity achieved in this experiment is over four times higher than that of the previously reported RH sensor based on a bare fiber structure without a hygroscopic coating layer [116].

As to the source of the RH induced spectral shift, it is known that water vapour can be adsorbed on a silica surface and that this in turn will change the

local RI. With an increase of the RH, more water vapour is adsorbed on the fiber surface, which increases the effective RI. In the simple demonstration carried out here, a further contributing factor to the spectral shift is that since the tapered SCSMF is suspended slightly above the glass slide, an increase in the adsorbed water vapour can increase stress and introduce a bend to the tapered SCSMF section due to increased weight and this alters light propagation within the fiber and this in turn leads to an additional source of spectral shift.

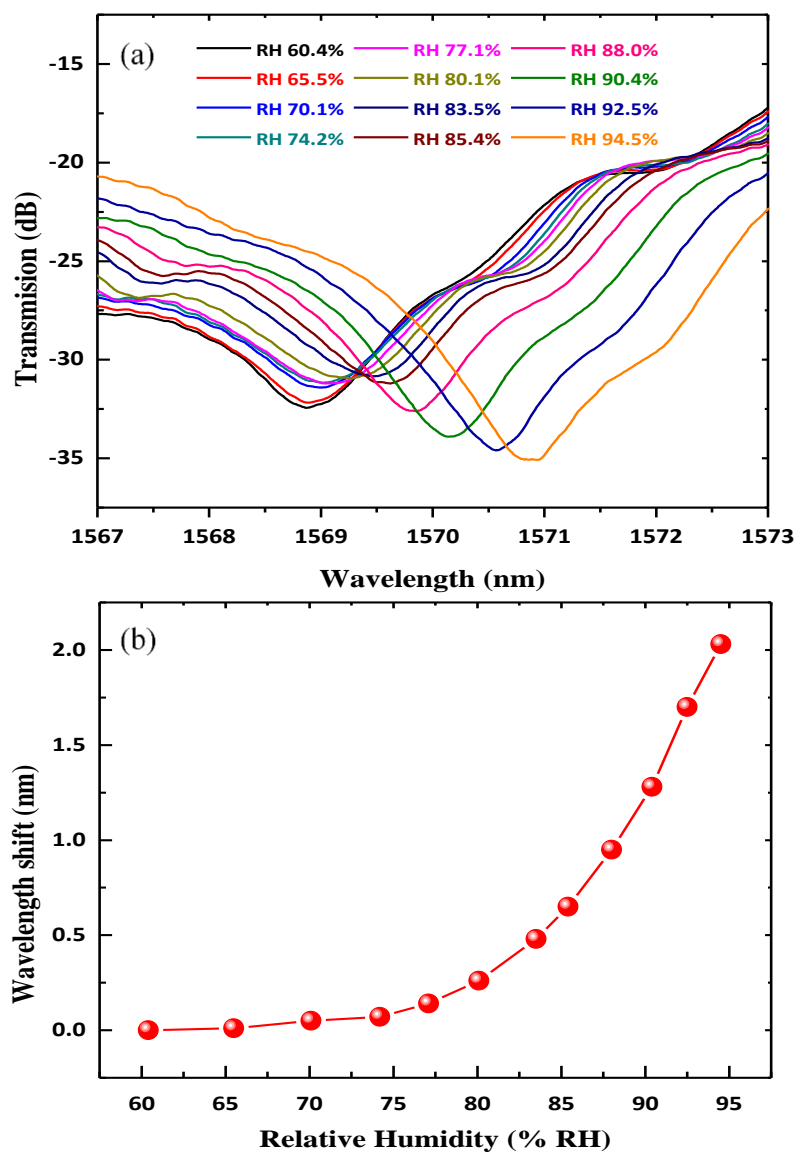


Figure 24. (a) Measured spectral responses at different RH values for S-12.5; (b) wavelength shift vs. RH.

3.1.5 Conclusion

In conclusion, three tapered SCSMF fiber structures with different waist diameters (12.5 μm , 15.0 μm , and 18.8 μm) were fabricated by using the microheater brushing technique. These structures were used for RI sensing. Experimental results show that all the samples have very high RI sensitivity and that the RI sensor with a tapered waist diameter of 12.5 μm gives the highest sensitivity of 19212.5 nm/RIU in the RI range from 1.4304 to 1.4320. All sensors have a linear wavelength shift response vs. RI changes. The sample with a tapered waist diameter of 12.5 μm was used to test its RH sensing properties without any additional coating on the surface of the fiber. Experimental results indicate that the wavelength shift changes exponentially with the increase of RH in the RH range from 60% to 95% RH. A maximum RH sensitivity of 18.3 nm/RHU was achieved in the RH range from 90.4% to 94.5%.

3.1.6 References

- [93] Q. Wu, Y. Semenova, P. Wang, and G. Farrell, "A comprehensive analysis verified by experiment of a refractometer based on an SMF28-small-core singlemode fiber (SCSMF)-SMF28 fiber structure," *J. Opt.*, vol. 13, no. 12, pp. 937–946, 2011.
- [94] J. Wo, G. Wang, Y. Cui, Q. Sun, R. Liang, P. P. Shum, and D. Liu, "Refractive index sensor using microfiber-based Mach–Zehnder interferometer," *Opt. Lett.*, vol. 37, no. 1, pp. 67–69, 2012.
- [95] J. Villatoro and D. Monzón-Hernández, "Low-cost optical fiber refractive-index sensor based on core diameter mismatch," *J. Light. Technol.*, vol. 24, no. 3, pp. 1409–1413, 2006.
- [96] W. Liang, Y. Huang, Y. Xu, R. K. Lee, and A. Yariv, "Highly sensitive fiber Bragg grating refractive index sensors," *Appl. Phys. Lett.*, vol. 86, no. 15, pp. 151122, 2005.

- [97] J. Homola, S. S. Yee, and G. Gauglitz, "Surface plasmon resonance sensors: review," *Sensors Actuators, B Chem.*, vol. 54, no. 1, pp. 3–15, 1999.
- [98] Q. Wu, Y. Semenova, P. Wang, and G. Farrell, "High sensitivity SMS fiber structure based refractometer--analysis and experiment.," *Opt. Express*, vol. 19, no. 9, pp. 7937–7944, 2011.
- [99] V. Zamora, A. Díez, M. V Andrés, and B. Gimeno, "Refractometric sensor based on whispering-gallery modes of thin capillarie.," *Opt. Express*, vol. 15, no. 19, pp. 12011–12016, 2007.
- [100] L. Bo, P. Wang, Y. Semenova, and G. Farrell, "High sensitivity fiber refractometer based on an optical microfiber coupler," *IEEE Photonics Technol. Lett.*, vol. 25, no. 3, pp. 228–230, 2013.
- [101] Q. Wu, Y. Semenova, J. Mathew, P. Wang, and G. Farrell, "Humidity sensor based on a single-mode hetero-core fiber structure," *Opt. Lett.*, vol. 36, no. 10, p. 1752–1754, 2011.
- [102] G. Brambilla, F. Xu, P. Horak, Y. Jung, F. Koizumi, N. P. Sessions, E. Koukharenko, X. Feng, G. S. Murugan, J. S. Wilkinson and D. J. Richardson, "Optical fiber nanowires and microwires: fabrication and applications," *Adv. Opt. Photonics*, vol. 1, no. 1, pp. 107–161, 2009.
- [103] T. K. Yadav, R. Narayanaswamy, M. H. Abu Bakar, Y. M. Kamil, and M. A. Mahdi, "Single mode tapered fiber-optic interferometer based refractive index sensor and its application to protein sensing," *Opt. Express*, vol. 22, no. 19, pp. 22802–22807, 2014.
- [104] S. Zhu, F. Pang, S. Huang, F. Zou, Y. Dong, and T. Wang, "High sensitivity refractive index sensor based on adiabatic tapered optical fiber deposited with nanofilm by ALD," *Opt. Express*, vol. 23, no. 11, pp. 13880–13888, 2015.
- [105] Z. Xu, Q. Sun, B. Li, Y. Luo, W. Lu, D. Liu, P. Shum, L. Zhang, "Highly sensitive refractive index sensor based on cascaded microfiber knots with Vernier effect," *Opt. Express*, vol. 23, no. 5, pp. 6662–6672, 2015.
- [106] C. C. O. and G. F. Q. Wu, Y. Ma, Y. Semenova, J. Yuan, L. Bo, P. Wang, X. Sang, M. Teng, C. Yu, "A high sensitivity refractometer based on a tapered SCSMF structure and its application to biosensing," *OFS23*, 2014.
- [107] G. Brambilla, V. Finazzi, and D. J. Richardson, "Ultra-low-loss optical

- fiber nanotapers,” *Opt. Express*, vol. 12, no. 10, pp. 2258-2263, 2004.
- [108] Z. Tian, S. S. H. Yam, and H. P. Loock, “Single-mode fiber refractive index sensor based on core-offset attenuators,” *IEEE Photonics Technol. Lett.*, vol. 20, no. 16, pp. 1387–1389, 2008.
- [109] A. Iadicicco, A. Cusano, A. Cutolo, R. Bernini, and M. Giordano, “Thinned fiber Bragg gratings as high sensitivity refractive index sensor,” *IEEE Photonics Technol. Lett.*, vol. 16, no. 4, pp. 1149–1151, 2004.
- [110] Z. Tian, S. S.-H. Yam, and H. P. Loock, “Refractive index sensor based on an abrupt taper Michelson interferometer in a single-mode fiber,” *Opt. Lett.*, vol. 33, no. 10, pp. 1105–1107, 2008.
- [111] Y. Wang, D. N. Wang, M. Yang, W. Hong, and P. Lu, “Refractive index sensor based on a microhole in single-mode fiber created by the use of femtosecond laser micromachining,” *Opt. Lett.*, vol. 34, no. 21, pp. 3328–3330, 2009.
- [112] C. Guan, X. Tian, S. Li, X. Zhong, J. Shi, and L. Yuan, “Long period fiber grating and high sensitivity refractive index sensor based on hollow eccentric optical fiber,” *Sensors Actuators, B Chem.*, vol. 188, pp. 768–771, 2013.
- [113] P. Wang, G. Brambilla, M. Ding, Y. Semenova, Q. Wu, and G. Farrell, “High-sensitivity, evanescent field refractometric sensor based on a tapered, multimode fiber interference,” *Opt. Lett.*, vol. 36, no. 12, pp. 2233–2235, 2011.
- [114] A. Gaston, F. Perez and J. Sevilla, “Optical Fiber Relative-Humidity Sensor with Polyvinyl Alcohol Film,” *Appl. Opt.*, vol. 43, no. 21, pp. 4127–4132, 2004.
- [115] L. Alwis, T. Sun, and Grattan Kenneth V., “Analysis of polyimide-coated optical relative humidity sensor,” *IEEE Sens. J.*, vol. 13, no. 2, pp. 767–771, 2013.
- [116] W. Zhang and D. J. Webb, “Humidity responsivity of poly(methyl methacrylate)-based optical fiber Bragg grating sensors,” *Opt. Lett.*, vol. 39, no. 10, pp. 3026–3029, 2014.

3.2 High sensitivity sol-gel silica coated optical fiber sensor for detection of ammonia in water³

Abstract: A high sensitivity ammonia sensor based on a tapered small core singlemode fiber (SCSMF) structure for measurement of ammonia concentration in water is reported. Two tapered SCSMF fiber structures with different waist diameters of 23 μm and 13.5 μm are fabricated by using a customized microheater brushing technique. The silica based material prepared by the sol-gel method is used as a coating applied to the surface of the tapered fiber structures. To investigate the influence of the coating thickness on the sensitivity to ammonia in water, silica coatings with different thicknesses (2-pass and 8-pass coatings) are deposited on the surface of the fiber sensor with a waist diameter of 23 μm . Experiments demonstrate that the sensor with a thicker (8-pass) silica coating shows better sensitivity of 0.131 nm/ppm to ammonia compared to that of 0.069 nm/ppm for the thinner silica coating (2-pass). To further improve the sensor sensitivity, the taper waist diameter is reduced. For an 8-pass coating (249nm at the taper waist section) applied to a tapered SCSMF structure based fiber sensor with a reduced waist diameter of 13.5 μm . Experimental results show that the sensitivity to ammonia is significantly improved to 2.47nm/ppm. The best measurement resolution for ammonia concentration in water is estimated to be 4 ppb while the response and recovery times are less than 2 and 5 minutes respectively. The proposed sensor also offers good performance in terms of repeatability and good selectivity for sensing ammonia compared to that of other common ions and organic molecules in water.

³ D. Liu, W. H., A. K. Mallik, J. Yuan, C. Yu, G. Farrell, Y. Semenova, and Q. Wu, "High sensitivity sol-gel silica coated optical fiber sensor for detection of ammonia in water," Optics Express, vol. 24, no.21, pp. 24179–24187, 2016.

OCIS codes: (060.2280) Fiber design and fabrication; (060.2310) Fiber optics; (060.2370) Fiber optics sensors; (060.4005) Microstructured fibers; (160.6030) Silica.

3.2.1 Introduction

Ammonia plays a critical role in many applications; it has been widely used in various industrial processes, agricultural activity and in a number of biological systems [117-118]. However, excess ammonia has a toxic effect on the health of plants, animals as well as human beings, and hence it is essential to quantitatively and qualitatively sense the concentration of ammonia in water to prevent environmental pollution. Recently, a number of sensing techniques were proposed to measure ammonia concentration, such as an electro-chemical method [119], metal oxide semiconductor detectors [120], a ratiometric fluorescence sensor [121], and fiber optic based sensors [122-124]. Among these techniques, fiber optic based sensors have been attracting greater attention because of their unique properties, including miniature size, immunity to electromagnetic interference, remote sensing capabilities, and the possibility of operation at room temperature.

Implementing ammonia sensor based on an optical fiber will usually require that some additional coating material is deposited on the fiber surface. By monitoring the changes in optical properties of the fiber coating resulting from the physical or chemical reactions between ammonia and the coating material, the level of ammonia concentration can be detected. A number of optical fiber based ammonia sensors have been reported to date and can be divided into two categories depending on the physical principle of operation. One category of

sensors are based on detecting refractive index (RI) changes that result in wavelength shifts or power level changes in the transmission response spectrum of the sensor caused by the reactions between ammonia and coating materials (Type I); the other category of sensors are based on either measurement of absorption or fluorescence of traditional dye indicators (Type II). The coating materials used in Type I sensors are usually porous materials or nanomaterials, such as nano-assembled mesoporous coating of alternate layers of poly(diallyldimethylammonium chloride) (PDDA) and SiO₂ thin films [125-126], ZnO nanostructures [122] and ITO (In₂O₃ + SnO₂ in the ratio 90:10) [123]. The coating materials commonly employed in the Type II sensors involve polyaniline nanofibers [124] or organic dye (such as bromocresol purple (BCP)) immobilized porous silica membranes [127]. Sensors of Type I often suffer from inadequately low sensitivity at low ammonia gas concentrations (the detection limit is typically in the order of ppm), which may be attributed to the limited sensitivity of the fiber structure to the changes of the coating's RI or the coating material's poor absorption of ammonia. Sensors of Type II show excellent properties both in terms of ammonia gas sensitivity and low detection limit (typically in the order of ppb), but dye indicators do have some limitations such as high cost, limited lifetime, and low tolerance to the presence of ultraviolet light [128].

Numerous studies have been carried out on ammonia sensing in a gaseous environment, but research on ammonia sensing in water is relatively rare. One of the possible reasons is that sensing ammonia in water imposes much higher requirements on the sensor in terms of its stability and repeatability because preserving the coating's properties in water can be a challenging task. Most previously reported optical fiber sensors for ammonia sensing in water have been

based on a Type II operating principle. For example, Tao *et al.* reported an optical fiber probe for ammonia sensing in water by coating a BCP immobilized porous silica membrane and a thin PDMS layer on the surface of a bent optical fiber core. The lowest ammonia detection limit achieved in this work was 5 ppb [129]. Duong *et al.* proposed a fluorescence based ammonia sensor which features a short response time, high reversibility and long-term stability for a range of ammonia concentrations 1-60 ppm [130]. All of the previously reported sensors above have achieved good ammonia sensitivity in water but they suffer from the limitations of Type II dye based sensors mentioned previously. There is a previously reported sensor based on a Type I operating principle [126], which reported a SnO₂ thin film coated fiber sensor for detecting ammonia in water, but the sensor has a limited resolution of only 2 ppm. In this work, we describe a sensor of Type I to detect ammonia concentration in water, which does not suffer from the limitations of Type II sensors and addresses the challenge of achieving high sensitivity (sensitivity is improved by three orders of magnitude compared with [126]).

SMS (single mode-multimode-single mode) fiber structures are commonly used as the basis for a variety of sensor types, with chemical etching of the multimode fiber required in some applications. In our previous reports, we have proved that a small core singlemode fiber (SCSMF) is a good candidate to replace the multimode fiber section in an SMS fiber structure, with the advantage that chemical etching is not required [131-133]. Most recently, we reported a tapered SCSMF structure, which has a very high RI sensitivity of 19212.5 nm/RIU (RI unit) in the RI range from 1.4304 to 1.4320 [134]. In this work, we propose and demonstrate a highly sensitive optical fiber sensor based on a

tapered SCSMF structure. The sensor's operation is based on the Type I principle for the measurement of ammonia concentration in water, without the need for coating with dye materials. The proposed sensing structure was obtained by coating a thin layer of sol-gel silica on the tapered SCSMF structure surface. Compared with other coating nanomaterials, silica shows better adhesion to the fiber surface because both the optical fiber sensor and sol-gel silica are made of silica material.

Although the effect of adsorption of ammonia on the silica surface is well known [135-136], to the best of our knowledge there are no reports to date of the use of this effect in fiber optic sensors of Type I (silica is commonly used in sensors of Type II, but it is not used as the sensing materials). In this letter we experimentally demonstrate a novel sensor for detecting ammonia concentration in water fabricated by tapering of an SCSMF structure waist down to 13.5 μm and subsequently applying a silica coating upon its surface.

Adsorption of ammonia by the silica material results in a change of the silica coating RI which in turn leads to the spectral shift of the transmission response of the fiber sensor. Thus ammonia concentration can be measured by detecting the variations of the sensor's spectral response assuming a suitable calibration has taken place.

3.2.2 Experimental setup and sensor fabrication

In this experiment, two tapered SCSMF structures with tapered waist diameters of 23.0 μm (denoted as S-23) and 13.5 μm (denoted as S-13.5) were fabricated by using a customized microheater brushing technique [137].

A silica sol solution for the coating layer was prepared as follows: 1) 10 ml

of hydrolyzing tetraethylorthosilicate (TEOS) was mixed with 5 ml ethanol using magnetic stirring for 20 min at room temperature; 2) then 1 ml 0.1 mol/L HCl solution was added into the mixture followed with further stirring for 240 min; 3) the obtained silica sol solution was sealed in a small bottle and stored in a refrigerator during the experimental trials. Each sensor sample was fabricated by applying a thin layer of silica on the tapered fiber surface by passing the tapered SCSMF section through a drop of the silica sol solution using a motor controlled translation stage. A single pass of the silica drop from one side of the fiber to the other side is defined as a one-pass coating. By repeating the one pass coating process, different silica coating thicknesses can be realized. It should be noted that after each pass the coating was left to dry for ten minutes before the next coating layer was applied. When the desired number of coating passes were completed, the fiber sensor was cured firstly at room temperature for 24 hours and then heated at 120°C for two hours, followed by an additional 24 hour period of drying at room temperature. Before the ammonia test, the coated sensors were immersed in water overnight to eliminate the influence of water penetrating into the silica coating on the sensor performance. It is noted that all water used in this experiment is deionized water. Various ammonia concentrations in water were prepared by mixing “ammonia solution 0.88” with deionized water.

Figure 25(a) illustrates a schematic diagram of the silica-coated ammonia sensor and Fig. 25(b) shows a schematic diagram of the test system for ammonia sensing in water. The functionalized fiber ammonia sensor was placed in a PDMS mould with a narrow channel and the water/ammonia sample was pumped through the channel by a peristaltic pump at a speed of 20 r/min. This

enabled the water/ammonia sample to flow slowly through the volume surrounding the sensor. Light from a broadband light source (Thorlabs S5FC1005S) is launched into the tapered SCSMF structure and the transmitted light is measured by an optical spectrum analyzer (OSA) (Agilent 86142B). All the tests were conducted at room temperature.

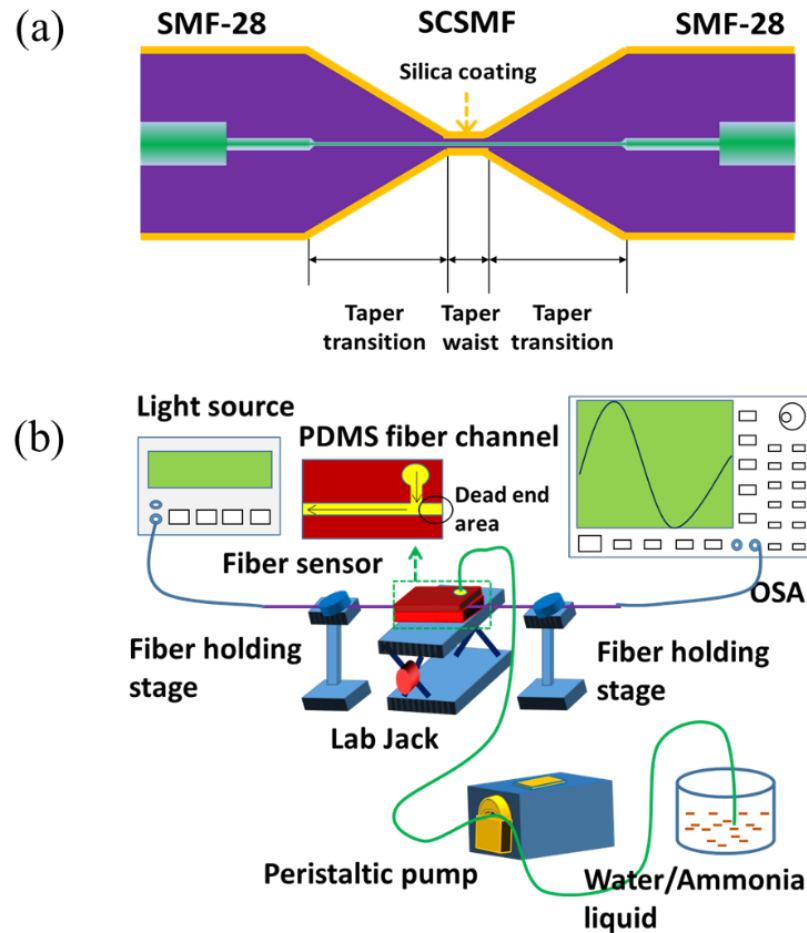


Figure 25. Schematic diagram of: (a) Tapered SCSMF structure and (b) Experimental setup for ammonia sensing in water.

3.2.3 Results and discussion

Figure 26 shows the measured spectral shift for the S-23 taper with two different coating thicknesses (2-pass and 8-pass coating) for various ammonia concentrations in water. In our experiment, the sensor's sensitivity S is defined as $S = \Delta\lambda/C$, where $\Delta\lambda$ represents the corresponding spectral wavelength shift

under different ammonia concentrations and C is the ammonia concentration in water. It is noted that in this study, the spectral shift is determined as the shift of the 3 dB mean wavelength of the selected spectral dip in the SCSMF transmission spectrum. From Fig. 26 it can be seen that as the ammonia concentration in water increases, the wavelength of the spectral dip shifts to a longer wavelength. Sensors with 2-pass and 8-pass coatings have sensitivities of 0.069 nm/ppm and 0.131 nm/ppm respectively at an ammonia concentration of 2.6 ppm, while at a concentration of 65 ppm, the sensitivities are 0.018 nm/ppm and 0.059 nm/ppm respectively. The results indicate sensor with a thicker sol-gel coating (8-pass coating in Fig. 26) has a higher sensitivity in the whole range of the tested ammonia concentrations. For both silica coating thicknesses, the sensitivity of the ammonia sensor decreases as the ammonia concentration increases.

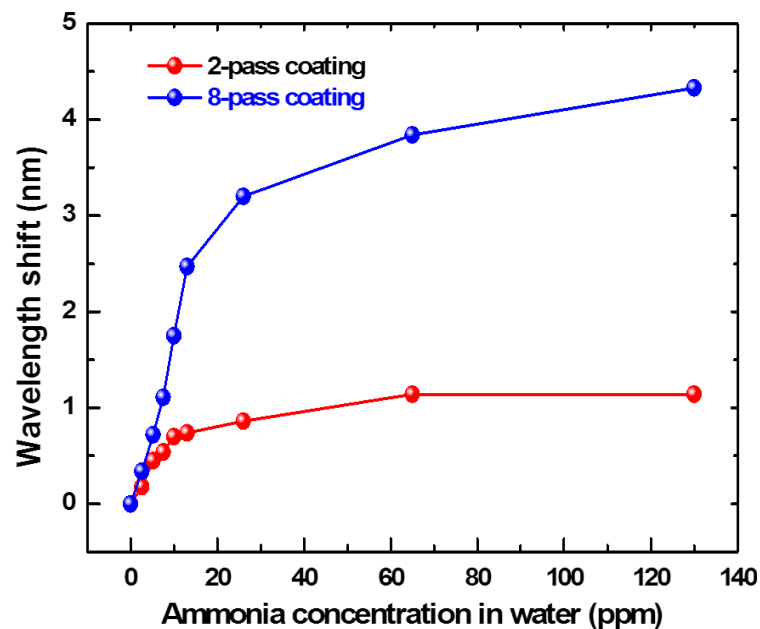


Figure 26. Measured spectral dip shift vs. ammonia concentration in water for S-23 with different coatings.

Decreasing the tapered waist diameter is a common strategy used in tapered

fiber sensor to improve sensitivity. Thus in this work we investigated whether an improvement in the sensitivity could be achieved by tapering the SCSMF section to a smaller diameter of 13.5 μm with 8-pass coating by the silica sol-gel. Figure 27(a) shows the measured spectral responses for the S-13.5 sensor at different ammonia concentrations in water and Fig. 27(b) shows the dependency of the measured wavelength shift vs. ammonia concentration. As one can see from Fig. 27(b), compared to the sensor S-23, the alternative sensor S-13.5 has significantly higher sensitivity. When the ammonia concentration is 2.6 ppm, the measured dip wavelength shift with respect to its position corresponding to pure water is 6.43 nm compared to that of 0.34 nm for the previous sensor shown in Fig. 26. As the ammonia concentration increases, the dip wavelength shifts to longer wavelength monotonically. However the shift rate decreases as ammonia concentration increases, which indicates that the sensor has higher sensitivity as well as better resolution for lower ammonia concentrations. The sensitivity is estimated to be 2.47nm/ppm at 2.6 ppm and 0.67nm/ppm at 65 ppm. Assuming the OSA has a wavelength resolution of 0.01 nm, the best resolution of the developed sensor at 2.6 ppm ammonia concentration could be as low as 4 ppb. It is worth pointing out that while reducing the tapered waist diameter of such a fiber sensor even more might result in a higher sensitivity, a tapered fiber with a smaller waist diameter is more fragile compared to that with a larger waist diameter, which could limit the sensor stability, depending on the packaging technology used in an actual application.

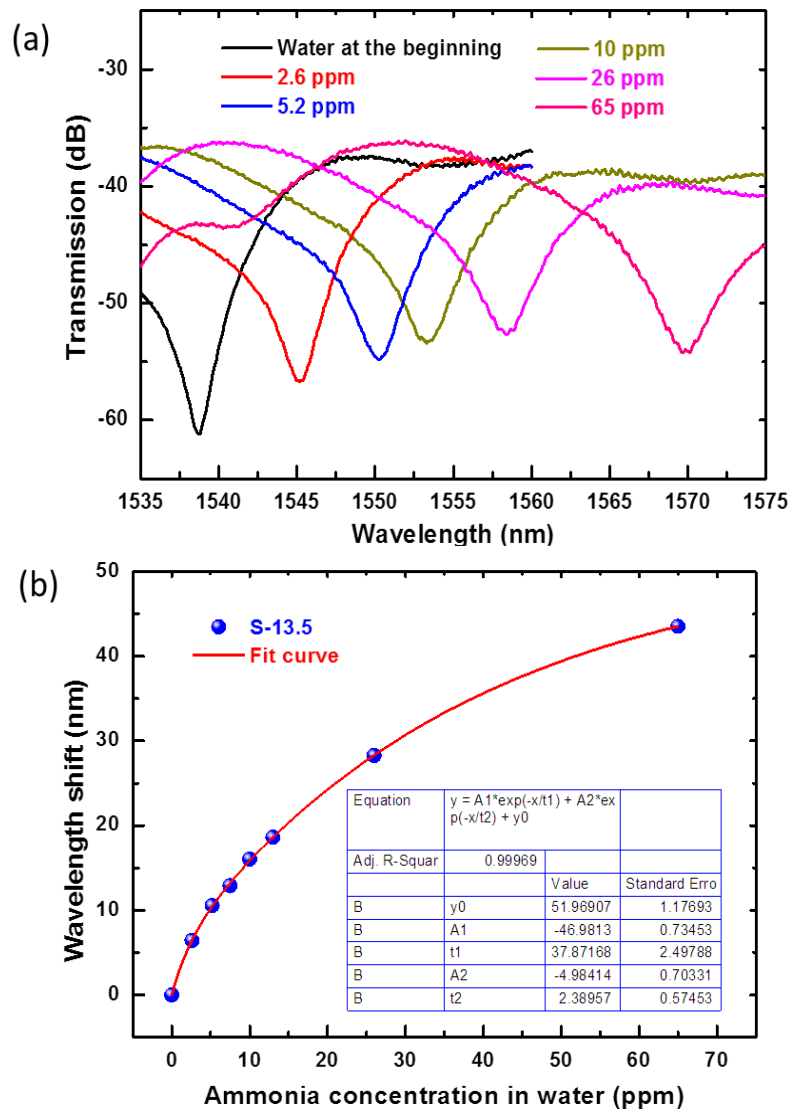


Figure 27. (a) Measured spectral response of S-13.5 at different ammonia concentrations in water; (b) Measured spectral wavelength shift vs. ammonia concentration in water (varies from 2.6 ppm to 65 ppm) for S-13.5 with 8-pass coating; measured data fitted with nonlinear function parameters of which are listed in the inset table.

The response and recovery times are illustrated for a range of ammonia concentrations in Fig. 28. The response time is defined as the time that takes the sensor to reach 90% of its full response and the recovery time as the time to fall down to 10% of the full response. The sensor's response time is estimated to be less than 2 minutes, while the recovery time is estimated to be less than 5 minutes. It should be noted that in our experiment the water/ammonia liquid sample is being constantly pumped through the PDMS channel to avoid

mechanical instabilities of the fiber sensor associated with replacement of the liquid sample. It is estimated that it takes about 30 s to fully replace the liquid sample within the PDMS channel of the adopted geometry and pumping speed. Most importantly, there is a "dead end" area (shown in Fig. 25 (b)) within the channel where liquid is never replaced but continuously dissolving into the new input water/ammonia liquid sample every time we replace it. Hence, it takes a longer time to eliminate the difference between the former liquid sample and the new one in the dead end of the channel and to equalize the ammonia concentration. Due to these shortcomings of our setup, the actual response and recovery times may well be even shorter.

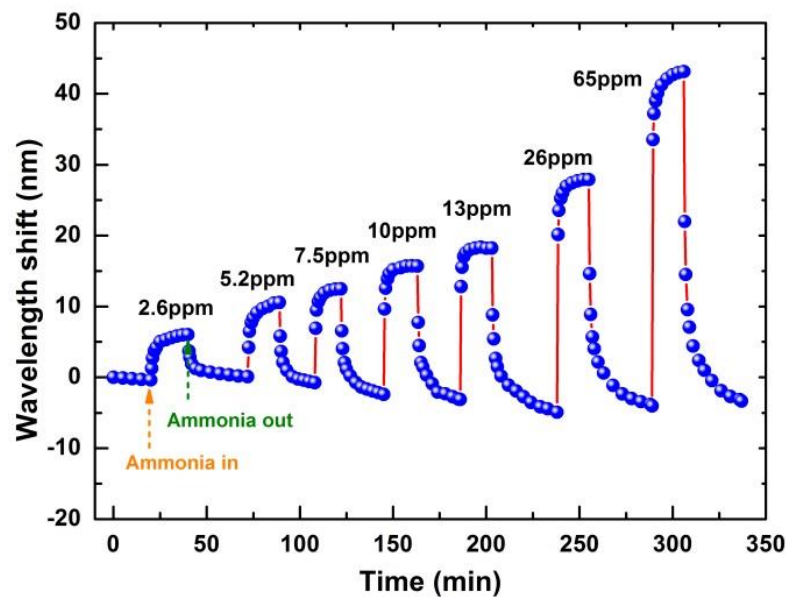


Figure 28. Sensor's response and recovery at different ammonia concentrations.

The morphology of the silica coating is also investigated using a scanning electron microscope (SEM) using a separate sample but with same fabrication parameters. The SEM images of a fiber sensor with a waist diameter of 13.5 μm coated with silica coating are shown in Fig. 29. One can see from the image that the silica coating is smooth at the taper waist section, while the taper transition section is mostly smooth but with some small cracks (as shown in the inset SEM

images Fig. 29(b)). From the cross-section SEM image, the coating thickness at the taper waist is estimated to be 249 nm as shown in the inset SEM image Fig. 29(a). It is noted that the position of the spectral dip in pure water after each ammonia sample measurement gradually moved to a shorter wavelength. One possible explanation for this is that the silica coating is being gradually removed from the fiber surface due to the cracks and non-ideal bonding to the fiber surface (as shown in Fig. 29) after long term immersion in the ammonia/water solution. In addition, the continuous flow of the liquid may also accelerate the separation of silica from the fiber surface. Furthermore, silica coating seems easier to be removed by a flow of the liquid sample from the fiber section with larger diameter, containing the cracks shown in Fig. 29(b). A possible solution to the problem of coating deterioration is the application of an additional protection layer over the silica coating, such as a thin layer of PDMS, which is known to perform well in water for the protection of both the silica coating and the dye [129].

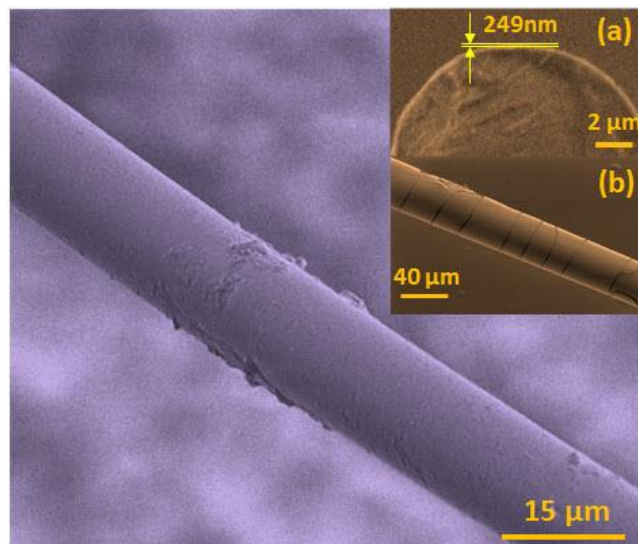


Figure 29. Silica coating morphology at the taper waist. The inset SEM images show (a) cross section at the taper waist; (b) taper transition section.

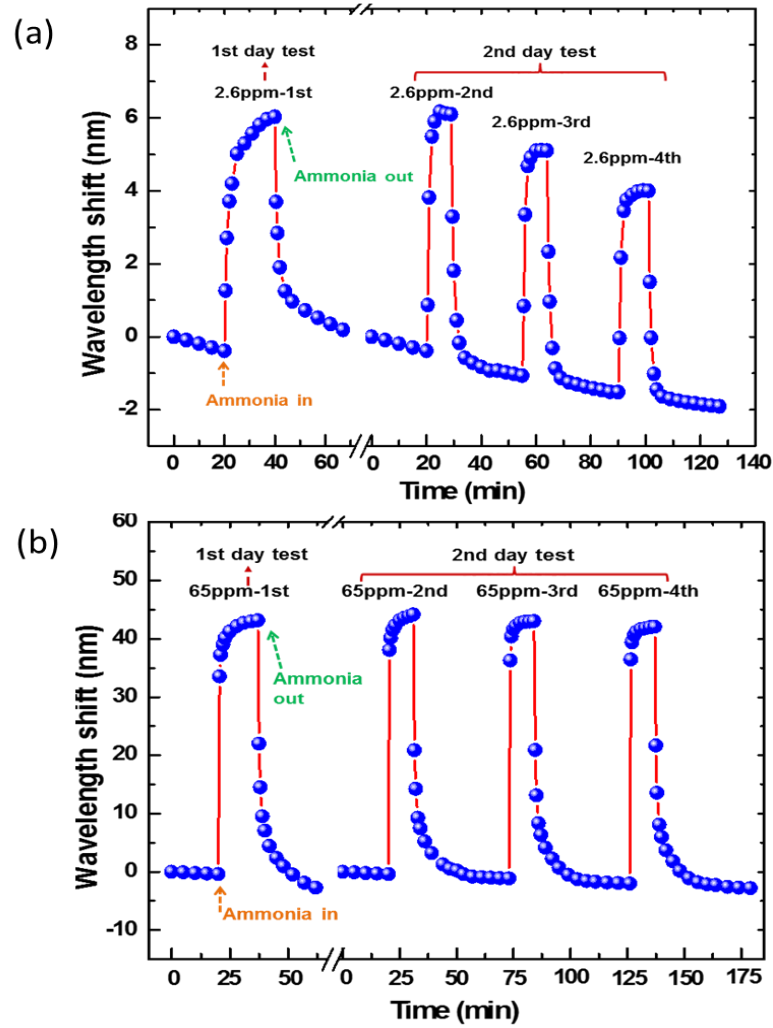


Figure 30. Sensor's response illustrating reversibility and repeatability of measurements for S-13.5 at low and high ammonia concentrations: (a) 2.6 ppm; (b) 65 ppm.

Table 2. Wavelength shift of the spectral dip for the S-13.5 sensor for a series of repeat tests at 2.6 ppm and 65 ppm ammonia concentrations in water.

	1-st test (nm)	2nd test (nm)	3rd test (nm)	4th test (nm)
2.6 ppm	6.43	6.51	6.17	5.47
65 ppm	43.53	44.56	44.14	44.09

The reproducibility of measurements for the ammonia sensor at low and high concentrations has also been investigated and the experimental results are shown in Fig. 30. The dip wavelength shifts are also summarized in Table 2. The reproducibility measurements were performed 24 hours later following the

experiments with various ammonia concentrations (we refer to the previous experiment as the “1st day test” while to the reproducibility measurement as the “2nd day test”). Figure 30 shows that our sensor exhibits good reproducibility. However it is worth noting that during the "2nd day test", when the sensor was tested three times within a short time frame (30 minutes between the tests), the wavelength shift (and hence sensitivity) decreases slightly after each consequent test for both low and high ammonia concentrations. This might be due to the fact that some residual ammonia molecules are not fully desorbed from the silica coating during the 30 min gap between these tests.

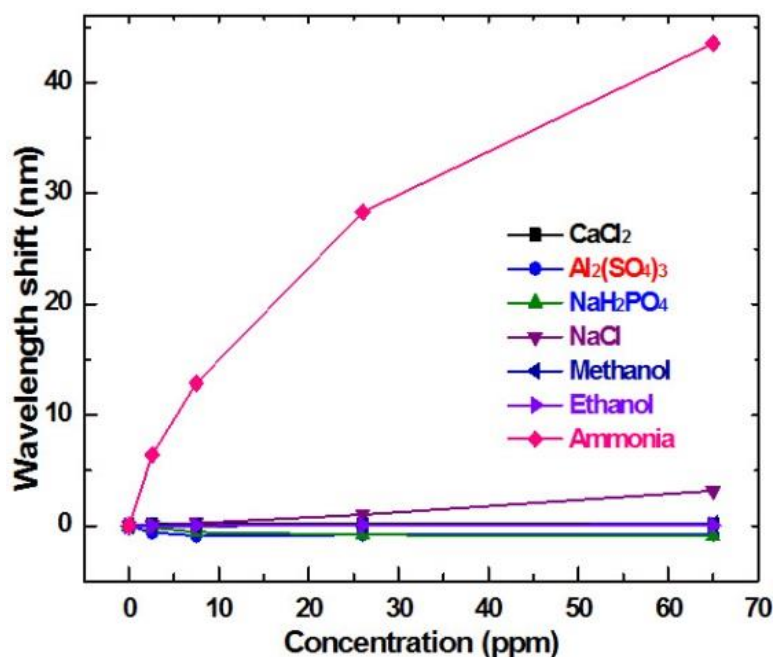


Figure 31. Sensor’s sensitivity to a range of ions and molecules including methanol, ethanol, CaCl₂, NaCl, Al₂(SO₄)₃, NaH₂PO₄ and ammonia in water.

A key parameter for an ammonia sensor is its cross sensitivity to other chemical compounds. Thus the sensor’s sensitivity to some other common ions in water and some organic molecules was also investigated. The presence of methanol, ethanol, CaCl₂, NaCl, Al₂(SO₄)₃ and NaH₂PO₄ in water was tested separately, and the experimental results are shown in Fig. 31. It is clear that silica

coating shows very low sensitivity to those ions and molecules in comparison with that to ammonia, which indicates that our sensor exhibits good selectivity to ammonia.

3.2.4 Conclusion

In conclusion, a novel ammonia sensor is proposed and experimentally investigated based on a silica-coated tapered SCSMF fiber structure. Two tapered SCSMF fiber structures with different taper waist diameters of 13.5 μm and 23 μm were fabricated using the microheater brushing technique. Silica sol-gel was prepared and coated on the fiber surface as a sensing layer for detecting ammonia concentration in water. The influence of the coating thickness on the sensitivity to ammonia in water is investigated by characterizing two sensors with different coating thickness (2-pass and 8-pass coatings). Experiments demonstrate that the sensor with a thicker (8-pass) silica coating shows better sensitivity of 0.131 nm/ppm to ammonia compared to 0.069 nm/ppm for a thinner (2-pass) silica coating. A sensor with improved sensitivity was prepared by tapering the SCSMF to a smaller waist diameter of 13.5 μm . The experimental results confirm that the sensor with an 8-pass coating offers an improved sensitivity of 2.47 nm/ppm compared to that of 0.131 nm/ppm for the sensor with a 23 μm waist diameter. The coating thickness (8-pass) was independently estimated using SEM images as 249 nm at the taper waist section for the sensor with a 13.5 μm waist diameter. The best resolution of the ammonia sensor is estimated to be as low as 4 ppb while the response and recovery times are less than 2 and 5 minutes respectively. The best resolution of the ammonia sensor is estimated as low as 4 ppb while the response and recovery times are less than 2 and 5 minutes respectively. In

addition, the sensor shows good repeatability and good selectivity to ammonia amongst a range of common ions in water and some organic molecules.

3.2.5 References

- [117] P. Warneck, *Chemistry of the Natural Atmosphere*, Academic Press, 1998.
- [118] S. Mukherjee, T. Sakorikar, A. Mukherjee, and A. Misra, "Water-responsive carbon nanotubes for selective detection of toxic gases," *Appl. Phys. Lett.*, vol. 106, no. 11, 2015.
- [119] A. L. Sharma, K. Kumar, and A. Deep, "Nanostructured polyaniline films on silicon for sensitive sensing of ammonia," *Sensors Actuators, A Phys.*, vol. 198, pp. 107–112, 2013.
- [120] S. K. Sinha, "Growth and ammonia sensing properties of $Zn_{1-x}Sn_xO$ nanofibers," *Sensors Actuators B Chem.*, vol. 219, pp. 192–198, 2015.
- [121] E. Jazan and H. Mirzaei, "Direct analysis of human breath ammonia using corona discharge ion mobility spectrometry," *J. Pharm. Biomed. Anal.*, vol. 88, pp. 315–320, 2014.
- [122] A. Og. Dikovska, G. B. Atanasova, N. N. Nedyalkov, P. K. Stefanov, P. A. Atanasov, E. I. Karakoleva, and A. Ts. Andreev, "Optical sensing of ammonia using ZnO nanostructure grown on a side-polished optical-fiber," *Sensors Actuators, B Chem.*, vol. 146, no. 1, pp. 331–336, 2010.
- [123] S. K. Mishra, D. Kumari, and B. D. Gupta, "Surface plasmon resonance based fiber optic ammonia gas sensor using ITO and polyaniline," *Sensors Actuators, B Chem.*, vol. 171–172, pp. 976–983, 2012.
- [124] S. A. Ibrahim, N. A. Rahman, M. H. Abu Bakar, S. H. Girei, M. H. Yaacob, H. Ahmad, and M. A. Mahdi, "Room temperature ammonia sensing using tapered multimode fiber coated with polyaniline nanofibers," *Opt. Express*, vol. 23, no. 3, pp. 2837–2845, 2015.
- [125] S. Korposh, R. Selyanchyn, W. Yasukochi, S. W. Lee, S. W. James, and R. P. Tatam, "Optical fibre long period grating with a nanoporous coating formed from silica nanoparticles for ammonia sensing in water," *Mater. Chem. Phys.*, vol. 133, no. 2–3, pp. 784–792, 2012.
- [126] M. Pisco, M. Consales, S. Campopiano, R. Viter, V. Smyntyna, M.

- Giordano and A. Cusano, "A novel optochemical sensor based on SnO₂ sensitive thin film for ppm ammonia detection in liquid environment," *J. Light. Technol.*, vol. 24, no. 12, pp. 5000–5007, 2006.
- [127] W. Cao and Y. Duan, "Optical fiber-based evanescent ammonia sensor," *Sensors Actuators, B Chem.*, vol. 110, no. 2, pp. 252–259, 2005.
- [128] B. Culshaw, "Optical fiber sensor technologies: opportunities and-perhaps-pitfalls," *J. Light. Technol.*, vol. 22, no. 1, pp. 39–50, 2004.
- [129] S. Tao, L. Xu, and J. C. Fanguy, "Optical fiber ammonia sensing probes using reagent immobilized porous silica coating as transducers," *Sensors Actuators, B Chem.*, vol. 115, no. 1, pp. 158–163, 2006.
- [130] H. D. Duong and J. II Rhee, "A ratiometric fluorescence sensor for the detection of ammonia in water," *Sensors Actuators, B Chem.*, vol. 190, pp. 768–774, 2014.
- [131] Q. Wu, Y. Semenova, P. Wang, G. Farrell, "A comprehensive analysis verified by experiment of a refractometer based on an SMF28-small-core singlemode fiber (SCSMF)-SMF28 fiber structure," *J. Opt.*, vol. 13, no. 12, pp. 125401, 2011.
- [132] Q. Wu, Y. Semenova, J. Mathew, P. Wang, and G. Farrell, "Humidity sensor based on a single-mode hetero-core fiber structure," *Opt. Lett.*, vol. 36, no. 10, p. 1752, 2011.
- [133] Q. Wu, Y. Semenova, P. Wang, and G. Farrell, "High sensitivity SMS fiber structure based refractometer--analysis and experiment.," *Opt. Express*, vol. 19, no. 9, pp. 7937–7944, 2011.
- [134] D. Liu, A. K. Mallik, J. Yuan, C. Yu, G. Farrell, Y. Semenova, and Q. Wu, "High sensitivity refractive index sensor based on a tapered small core single-mode fiber structure," *Opt. Lett.*, vol. 40, no. 17, pp. 4166–4169, 2015.
- [135] J. E. Mapes and R. P. Eischens, "The infrared spectra of ammonia chemisorbed on cracking catalysts," *J. Phys. Chem.*, vol. 58, no. 12, pp. 1059–1062, 1954.
- [136] G. a. Blomfield and L. H. Little, "Chemisorption of Ammonia on Silica," *Can. J. Chem.*, vol. 51, pp. 1771–1781, 1973.
- [137] G. Brambilla, V. Finazzi, and D. J. Richardson, "Ultra-low-loss optical fiber nanotapers," *Opt. Express*, vol. 12, no. 10, pp. 2258–2263, 2004.

3.3 High sensitivity optical fiber sensors for simultaneous measurement of methanol and ethanol⁴

Abstract: High sensitivity volatile organic compounds (VOCs) sensors based on a tapered small core single mode fiber (TSCSMF) and a microfiber coupler (MFC) are reported. The TSCSMF had a waist diameter of $\sim 5.1 \mu\text{m}$ and the MFC had a waist diameter of $\sim 1.9 \mu\text{m}$ each and both were fabricated using a customized microheater brushing technique. Silica based materials containing immobilized Nile red prepared by sol-gel method with two different recipes (recipe I and recipe II) are investigated. Initially recipe I based coating materials were applied to the surfaces of the TSCSMF and MFC. The experimental results show that the sensor based on an MFC shows much better sensitivities of -0.130 nm/ppm and -0.036 nm/ppm to ethanol and methanol than those of the TSCSMF based sensor. The corresponding minimum detectable concentration change of the MFC based sensor are calculated to be $\sim 77 \text{ ppb}$ and $\sim 281 \text{ ppb}$ to ethanol and methanol respectively. Both sensors are demonstrated fast response times of less than 5 minutes, while the recovery times varied from 7 minutes to 12 minutes. In addition, another TSCSMF based sample ($\sim 7.0 \mu\text{m}$) coated with a mixed layer of sol silica and Nile red prepared by recipe II was fabricated to achieve simultaneous measurement of ethanol and methanol, employing a second-order matrix approach.

Keywords: Volatile organic compounds, optical fiber sensor, tapered fiber, sol-gel silica, Nile red.

⁴ D. Liu, R. Kumar, F. Wei, W. Han, A. K. Mallik, J. Yuan, S. Wan, X. He, Z. Kang, F. Li, C. Yu, G. Farrell, Y. Semenova and Q. Wu, "High sensitivity optical fiber sensors for simultaneous measurement of methanol and ethanol", *Sensors and Actuators B: Chemical*, vol. 271, pp. 1-8, 2018.

3.3.1 Introduction

Volatile organic compounds (VOCs) are the major pollutants for indoor environments, as a result of their presence in many household products (e.g. paints, wax and furniture) and combustion processes (e.g. heating and smoking). Inhaling excess VOCs and their degradation products may cause respiratory system damage or even cancer [138-139]. Studies show that VOCs may be also related to global warming, stratospheric ozone depletion and photochemical ozone [140]. The growing awareness of the negative impact of VOCs on both human health and the global environment has been attracting increasing efforts to improve the detection, monitoring and analysis of VOCs. So far, a number of sensing techniques have been proposed to monitor the concentration of VOCs, such as semi-conductor metal oxides detectors [141], surface acoustic wave methods [142], chemiresistors [143], colorimetric sensors [144], infrared attenuated total reflection (IR-ATR) spectroscopy [145] and fiber optics sensors [146-147]. Among these techniques, fiber optic sensors have been attracting significant attention due to their well-known advantages, such as compact size, real-time operation, immunity to electromagnetic interference and remote sensing capabilities.

Deposition of additional materials on the fiber surface is usually required to implement an optical fiber based VOCs sensor. To date, a range of sensitive materials for various VOCs have been proposed, including hydrophobic ethylene/propylene (60/40) co-polymer [145], chemical dyes with solvatochromic properties [146], semiconductor metal oxides (TiO₂, ZnO, ITO) [148-150], zeolite thin film [151], polymethyl methacrylate (PMMA) film [152], poly (dimethylsiloxane) (PDMS) film [153] vapochromic materials [154], metal

based nanomaterials [155], and p-sulphanatocalix arene [156]. Among these, ethylene/propylene (60/40) co-polymer, solvatochromic dye materials, and semiconductor metal oxides have been found to possess relatively high sensitivities to VOCs (providing detection resolution in the level of ppb) and as a result semiconductor metal oxides have been widely used in commercial chemical vapor sensors. However, a significant disadvantage of these materials is that while they normally operate well at a high temperature (200-500 °C) they display a very limited gas sensitivity at room temperature (usually with a detection resolution of tens or hundreds of ppm [148-149]). As an alternative recently, Khan et. al. [146] have proposed a highly sensitive VOCs sensor based on a side-polished single-mode fiber with a coating layer incorporating a solvatochromic dye material (Nile red) with N, N-dimethylacetamide (DMAC) and polyvinylpyrrolidone (PVP). However the sensor proposed by Khan et al suffer from the disadvantage of a narrow measurement range (less than 9 ppb), compounded by a complex fabrication process and demodulation scheme.

Porous silica prepared by the sol-gel method offers chemical and thermal stability, an inert nature and transparency over a wide range of wavelengths, which has been widely used in optical fiber based chemical sensors either as assistant materials for the purpose of immobilization of specific sensitive materials [157] or as a chemically sensitive material in itself [158-159]. In addition, the textural properties such as the pore size, pore ratio, refractive index and even morphology of porous silica can be tuned by customizing a wide range of preparation parameters including water/precursor/solvent molar ratio, pH and temperature during both the fabrication and the subsequent drying process [160-161]. To take full advantage of porous silica materials and the highly

sensitive dye materials (Nile red) for sensing VOCs, we propose here a coating mixture of Nile red immobilized sol-gel silica suitable for VOCs detection.

Previously, we have demonstrated that both a tapered small core single mode fiber (TSCSMF) and a microfiber coupler (MFC) are highly sensitive to surrounding refractive index change and have been developed as high sensitivity ammonia sensors [158, 162-163]. In this work we report high sensitivity VOCs sensors based on both TSCSMF and MFC structures coated with a layer consisting of a mixture of Nile red and sol-gel silica. Besides we also demonstrate simultaneous measurement of methanol and ethanol concentrations in air by using two TSCSMF based sensors functionalized with different coating layers based on different recipes.

3.3.2 Theory and operating principle of the sensors

3.3.2.1. Operation principle for the TSCSMF and MFC

The TSCSMF is based on the coupling of multiple modes within a single fiber structure while in the MFC, the coupling of modes occurs between two individual fibers, which results in the different directions for the spectral shifts induced by the same environmental changes. Specifically, in our experiment, a red shift and a blue shift in the transmission spectra are observed with the increase of gas concentrations for the TSCSMF and MFC fiber sensors, respectively. The detailed operation principle of TSCSMF and MFC could be found in the previous reports, which is not listed here for the sake of brevity [158, 162-165].

3.3.2.2. Operating principle for Nile red

Nile red has been widely used as a solvent polarity indicator and for the measurement of solvent strength [166-167]. It is a dye material with positive solvatochromism properties, which indicates that a molecule in the first excited state is better stabilized by solvation than a molecule in the ground state, with increasing solvent polarity. The strength of intermolecular solute/solvent interactions and the dipole moment in the ground state and the excited state are dependent on the chemical structure and physical properties of the solute/solvent molecules [166]. In our experiment, when Nile red comes into contact with VOCs, the dipole moment changes from its ground state to an excited state due to the changed charge transfer between the donor (diethyl amino) and acceptor (carbonyl oxygen) moieties of Nile red. As a consequence, the energy band gap between the ground and the first excited state changes, further resulting in a change in the relative permittivity of the constituent molecules and hence a change in the refractive index of the dye material [168]. For use within a sensor, small changes in refractive index of the coating layer can be monitored by the tapered fiber structures used.

3.3.3 Experiments

3.3.3.1 Nile red immobilized sol-gel silica fabrication

The solution mixture of Nile red and sol-gel silica used for the coating was prepared as follows: (1) 10 ml of hydrolyzing tetraethylorthosilicate (TEOS) was mixed with 5 ml of ethanol for 20 minutes using magnetic stirring at room temperature; (2) 1 ml 0.1 mol/L HCl solution was added into the mixture followed by further stirring for a certain amount of time, that is 40 minutes to

produce recipe I and 120 minutes to produce recipe II; (3) 10 mg of Nile red was mixed with 6 ml of the sol solution obtained in step (2) under stirring for one more hour, after which the final sol solution was ready for the coating process. Due to the sol-gel process within the solution, a different stirring time results in different solution viscosity and hence a different refractive index, texture properties, coating thickness and a different Nile red concentration.

3.3.3.2 TSCSMF/ MFC fiber structures fabrication and dip coating process

In our experiment, two different fiber structures based on a TSCSMF and a MFC were fabricated by a customized microheater brushing technique; the detailed fabrication process can be found in [162-163]. Figure 32a and b illustrate the schematic diagrams of the proposed TSCSMF and MFC structures.

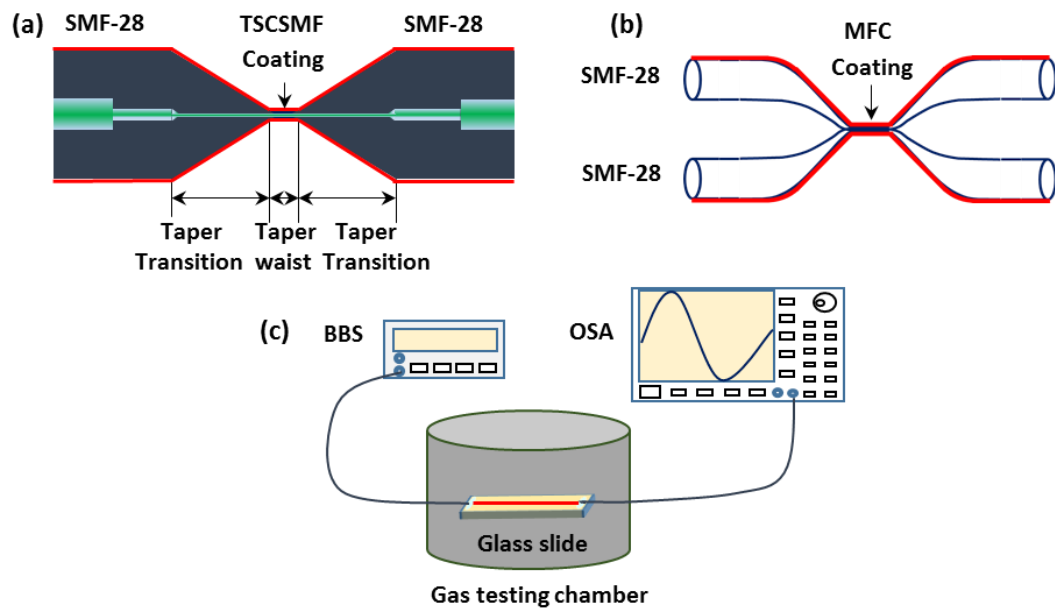


Figure 32. Schematic diagram of: (a) TSCSMF, (b) MFC and (c) experimental setup for VOCs sensing.

A thin layer which has Nile red immobilized within silica gel (recipe I) was coated on the tapered fiber surface by a dip coating method, where a motor controlled translation stage was employed to pass a drop of the coating solution

through each tapered fiber structure sample. A single pass coating cycle is defined as a one-pass coating. By repeating the one-pass coating process, different silica coating thicknesses can be realized. It should be noted that after each pass, the coating was left to dry for 6 minutes before the next coating layer was applied. After repeating the one-pass dip coating process a number of times, the functionalized fiber sensor was cured at room temperature for three days before use.

3.3.3.3 Experimental setup for VOCs sensing

Figure 32c shows a schematic diagram of the experimental setup for VOCs sensing. Light from a broadband light source is launched into the fiber sensor structure and the transmitted light is measured by an optical spectrum analyzer (OSA). In order to realize different VOCs concentrations, different volumes of VOCs liquids (ethanol/methanol) were introduced into the gas testing cylinder chamber (which has a diameter of 23 mm and a height of 11.5 mm) using a micro-syringe. The VOCs liquids evaporate naturally within the chamber, generating VOCs gas vapors with predictable concentrations which can be calculated according to a specific VOC mole ratio to air in the chamber. When the gas vapor is absorbed by the coating layer, the physical properties (refractive index and thickness) of the coating materials change, resulting in the variation of the measured spectral response of the sensor at different gas concentrations. Once the spectrum variation is calibrated, the concentration of the VOC can be determined. In the experiments, all tests were conducted at room temperature.

3.3.4 Results and discussion

3.3.4.1 Scanning electron microscope (SEM) and Energy-dispersive X-ray spectroscopy (EDS) analysis

Figure 33a illustrates an SEM image of the functionalized TSCSMF. As one can see from the figure, some small particles are attached to the fiber surface. These particles are clusters of undissolved Nile red ($C_{20}H_{18}N_2O_2$) which is confirmed by the EDS analysis on both a particle and smooth surface where increased carbon atoms in weight of 21.8% are detected on the particle compared to that of 10.18% on the smooth fiber surface. A very small amount of copper and zinc atoms were also detected due to the use of a copper sheet to support the fiber. SEM images of an MFC sample after its coating are presented in Fig. 33b and c, showing similar coating features for the TSCSMF. The measure diameters of the TSCSMF and MFC are found to be $\sim 5.1 \mu\text{m}$ and $\sim 1.9 \mu\text{m}$ (for each tapered SMF), respectively.

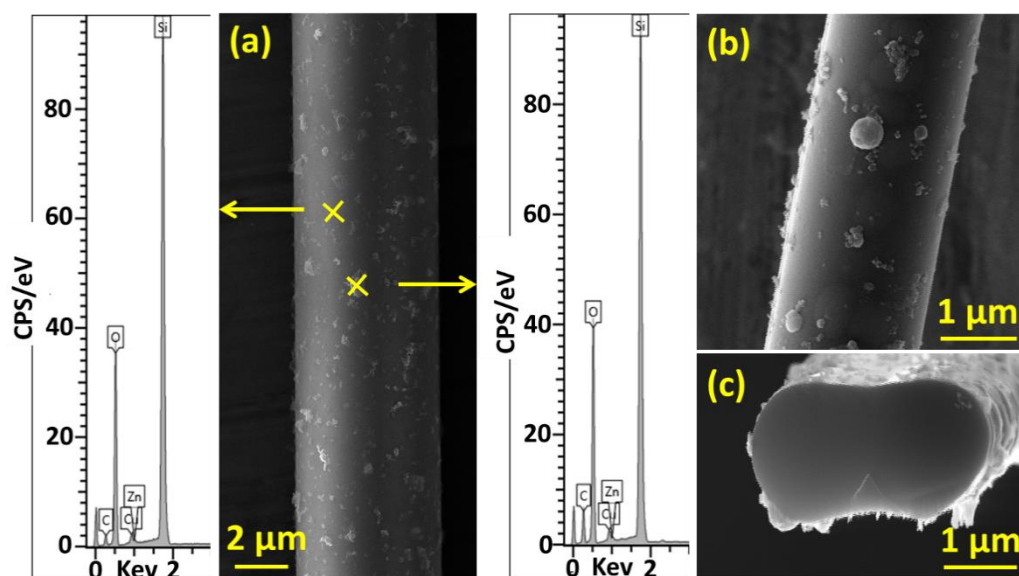


Figure 33. SEM images of (a) TSCSMF, (b) MFC and (c) the cross section of MFC after coating with Nile red immobilized sol-gel silica (recipe I). EDS results on the coating surface of TSCSMF sample are also shown in (a).

3.3.4.2 Spectral response to VOCs for the sensors based on the TSCSMF and MFC.

Examples of the measured spectral responses for the 8-pass coating TSCSMF sensor and the 4-pass coating MFC sensor exposed to different ethanol concentrations are shown in Fig. 34a and b. Different numbers of coating passes were chosen for the different sensor types since from previous experience it was found that a thicker coating would result in a higher sensitivity [158], but in practice it was found that the MFC is too fragile to be coated more than 8 times due to its smaller tapered waist diameter compared to the SCSMF. It is also noted that even with the same number of coating passes, the actual coating thickness achieved can be different because of variations in the tapered diameter [169]. As can be seen from Fig. 34a, the spectral dip wavelength of the TSCSMF based sensor shifts toward a longer wavelength (red shift) as the VOC's concentration increases. In contrast, a blue shift is observed for the MFC based sensor as shown in Fig. 34b.

The spectral responses for the measurement of the other VOC used, methanol, are not shown here for the sake of brevity since they have similar spectral responses but different wavelength shift values. Figure 34c and d summarize the measured wavelength shifts at different concentrations of ethanol and methanol. In the figures, we define a red shift as a positive wavelength shift while the blue shift as a negative wavelength shift. The wavelength shifts versus gases concentrations show good linearity for both sensors, but the sensor based on an MFC exhibits better sensitivities of -0.130 nm/ppm and -0.036 nm/ppm to ethanol and methanol respectively, compared to those of 0.018 nm/ppm and 0.005 nm/ppm for the TSCSMF based sensor. This is reasonable since that

smaller taper waist diameter of the MFC leads to an increase in the portion of the evanescent field exposed to the surrounding environment and hence results in a higher sensitivity for the sensor. Furthermore the sensor's sensitivity S is defined as $S = \Delta\lambda / C$, where C is the VOCs concentration and $\Delta\lambda$ represents the corresponding spectral wavelength shift for different VOCs concentrations. Assuming an OSA has a wavelength resolution of 0.01 nm, the minimum detectable concentration change of the MFC for ethanol and methanol are about 77 ppb and 281 ppb, which is over one magnitude higher than the previous reports in which the minimum detectable concentration change at a level of ppm were achieved [147, 151-154].

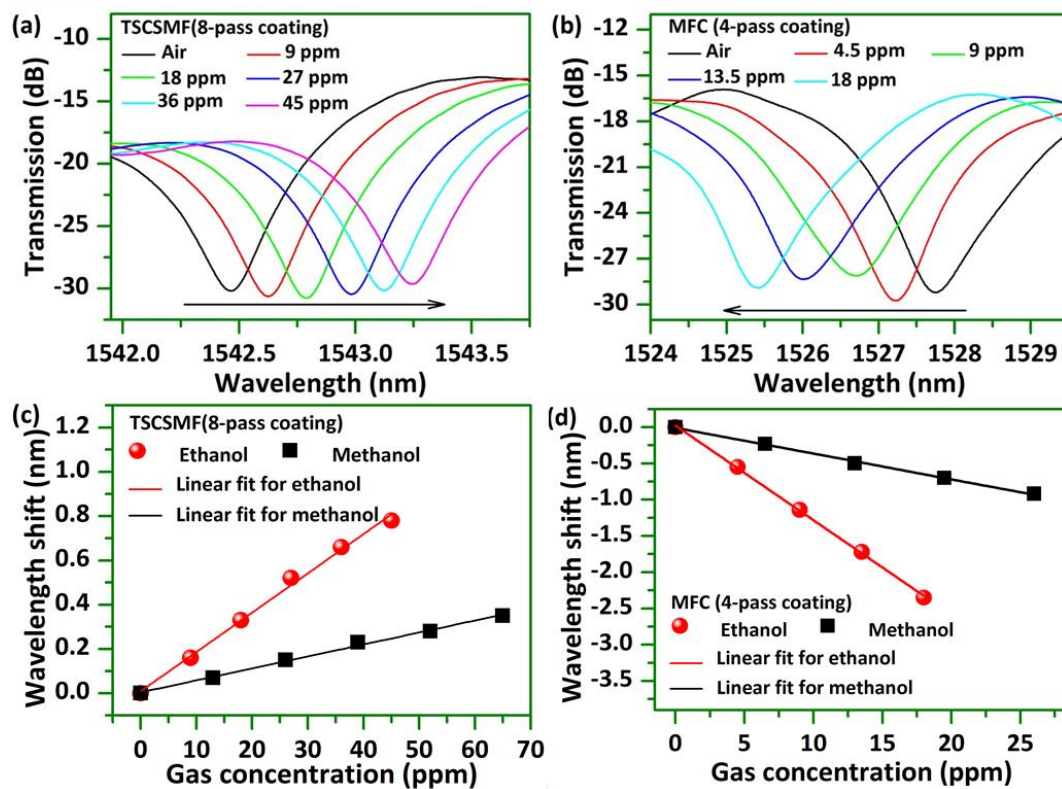


Figure 34. Normalized measured spectral response at different concentrations of ethanol for (a) TSCSMF with 8-pass coating and (b) MFC with 4-pass coating; Measured corresponding wavelength shifts for different VOCs and concentrations for (c) TSCSMF with 8-pass coating and (d) MFC with 4-pass coating.

The response and recovery times of sensors to both ethanol and methanol are also investigated at selected gas concentrations and examples are illustrated in Fig. 35. The response time is defined as the time during which the sensor's response reaches 90% of its full response in terms of wavelength shift and the recovery time as the time it takes for it to fall to 10% of the full response. The sensor based on a TSCSMF (Fig. 3a) shows a faster response time of 2 minutes and a recovery time of 8 minutes. For the measurement of the response of the TSCSMF to ethanol, it is apparent that the response overshoots initially (data points circled with a purple dashed line). We believe this can be attributed to the fast contact and reaction between the sensor head and the gas under test whose concentration is initially uneven throughout the chamber due to combined effects of spatial variations in liquid evaporation and gas diffusion, after the VOCs liquid drops are introduced into the chamber. To achieve a more stable change of gas concentration surrounding the sensor head, in tests for the MFC based sensor, a flat steel sheet was placed between the sensor head and the liquid drop point in the chamber to avoid an overly fast interaction. As shown in Fig. 35b, no evidence of overshoot is observed, the MFC based sensor shows faster response of less than 5 minutes to both ethanol and methanol, but a longer recovery time of about 12 minutes is required for methanol compared with that for ethanol. It should be noted that the actual sensor response times are likely to be shorter than our measured results, due to the time taken by the liquids to evaporate within the chamber and for the VOCs to be evacuated from the volume space of the chamber.

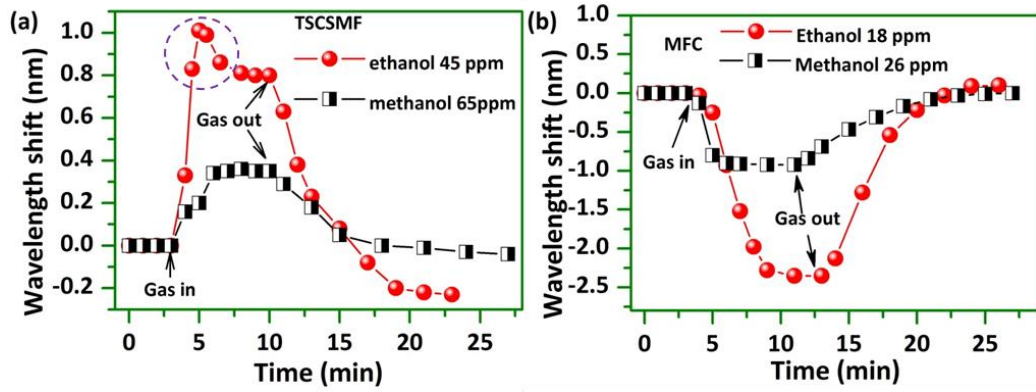


Figure 35. Spectral response and recovery of (a) TSCSMF based sensor with 8-pass coating and (b) MFC based sensor with 4-pass coating to ethanol and methanol at selected gas concentrations.

3.3.4.3 Measurement Repeatability

Selected ethanol concentrations were chosen to perform the repeatability tests for both sensors and the experimental results are shown in Fig. 36. The corresponding dip wavelength shifts are summarized in Table 3 which shows a very minor wavelength shift variation recorded for three tests carried at fixed time intervals, demonstrating that both sensors show good repeatability. It is noted that after each round of tests, the wavelength dip of both sensors does not return to the original wavelength, which is possibly due to the reaction between the VOCs and coating materials, resulting in changes in the coating materials. However, the sensors for each test round do have similar relative wavelength shifts, following the introduction of the VOCs. This is subject of further investigation at present.

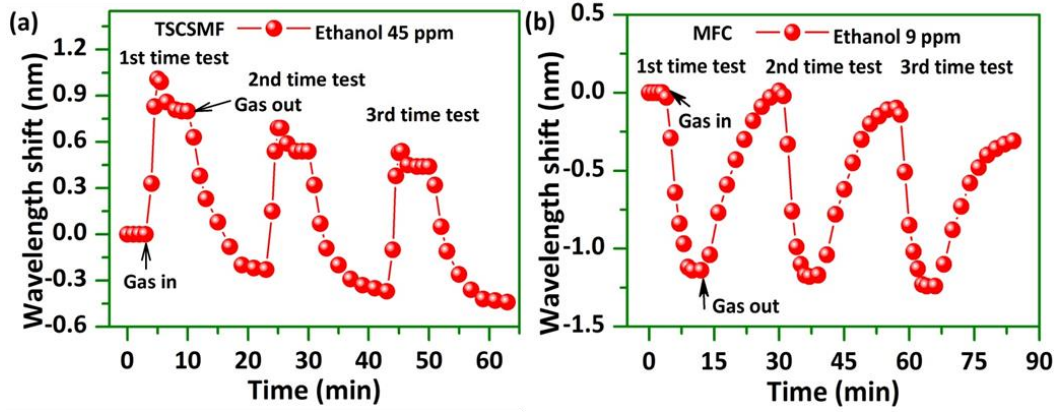


Figure 36. Sensors' response and recovery illustrating reversibility and reproducibility of measurements for both sensors at selected ethanol concentrations of 45 ppm and 9 ppm: (a) TSCSMF; (b) MFC.

Table 3. Spectral dips wavelength shifts for the TSCSMF and MFC based sensors for a series of repeat tests at selected ethanol concentrations.

	1st test (nm)	2nd test (nm)	3rd test (nm)
TSCSMF	0.8	0.78	0.81
MFC	-1.14	-1.18	-1.15

3.3.4.4 Simultaneous measurement for methanol and ethanol

As it was shown in above sections, both TSCSMF and MFC based sensors display linear wavelength shifts in response to variations of the tested gases concentrations. A key question is whether or not these two sensors working together can be used to simultaneously detect ethanol and methanol. To investigate this it is useful to develop a second-order matrix showing the relationship between spectral wavelength shifts and gases concentrations as shown by equation (3.1).

$$\begin{bmatrix} \Delta W_T \\ \Delta W_M \end{bmatrix} = \begin{bmatrix} k_{00} & k_{01} \\ k_{10} & k_{11} \end{bmatrix} \cdot \begin{bmatrix} C_e \\ C_m \end{bmatrix} \quad (3.1)$$

where ΔW_T and ΔW_M are the wavelength shifts of the TSCSMF and MFC

sensors and C_e and C_m correspond to the gas concentrations of ethanol and methanol respectively. The sensor based on TSCSMF has sensitivity coefficients of k_{00} and k_{01} to ethanol and methanol respectively, while for the sensor based on an MFC, the sensitivity coefficients to ethanol and methanol are k_{10} and k_{11} respectively.

From our previous experiments detecting ethanol and methanol separately, the sensitivity values are known to be $k_{00}=0.018$ nm/ppm, $k_{01}=0.005$ nm/ppm, $k_{10} = -0.130$ nm/ppm and $k_{11} = -0.036$ nm/ppm. The ratios $k_{00}/k_{10} = -0.138$ and $k_{01}/k_{11} = -0.139$ are very close, which indicates that these two sensors cannot be used for simultaneous measurement of ethanol and methanol because there would be no unique solution for the matrix. This is most likely because both sensors were coated with materials with the same texture which may show similar absorption properties to the tested VOCs.

To address this problem, a coating mixture prepared with method of recipe II (stirring for a longer time) is employed as a new coating material applied to a new TSCSMF based sample surface. A relatively large tapered waist diameter of $7.0 \mu\text{m}$ is chosen in this case and the fiber surface was coated with a layer formed by 4-pass coating. Due to a longer stirring time applied in the recipe II based coating material, the resulting solution has higher viscosity and higher Nile red concentration, compared to the material prepared in accordance with recipe I. Higher viscosity leads to a thicker coating with larger amount of Nile red, which is confirmed by the SEM image shown in Fig. 37, where a number of large clusters of Nile red particles are observed.

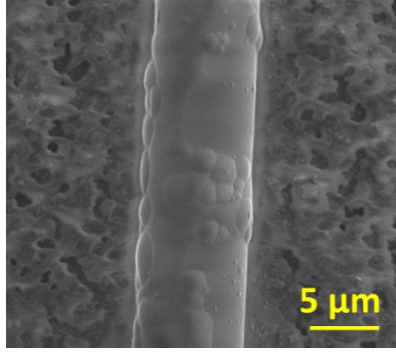


Figure 37. A SEM images of the new TSCSMF sample after coating with recipe II based material.

Figure 38a shows examples of the measured spectral responses at different ethanol concentrations. The spectral responses for methanol are similar and hence are not shown here for the sake of brevity. Figure 38b summarizes the measured wavelength shift versus different VOCs concentrations, which shows good linearity as well. The measured sensitivities of the new coated TSCSMF sensor are 0.004 nm/ppm to methanol, and 0.007 nm/ppm to ethanol.

When both of the prepared TSCSMF sensors are used, the sensitivity coefficients in the matrix in equation (3.1) are: $k_{00}=0.018$ nm/ppm, $k_{01}=0.005$ nm/ppm, $k_{10}=0.007$ nm/ppm, $k_{11}=0.004$ nm/ppm. It is clear that the values of $k_{00}/k_{10} = 2.571$ and $k_{01}/k_{11} = 1.25$ are now sufficiently different than the previous case, so that the matrix above can be used for simultaneous measurement of ethanol and methanol concentrations.

According to equation (3.1), the wavelength shifts of the two sensors can be calculated as:

$$\begin{bmatrix} \Delta W_T \\ \Delta W_M \end{bmatrix} = \begin{bmatrix} 0.018 & 0.005 \\ 0.007 & 0.004 \end{bmatrix} \cdot \begin{bmatrix} C_e \\ C_m \end{bmatrix} \quad (3.2)$$

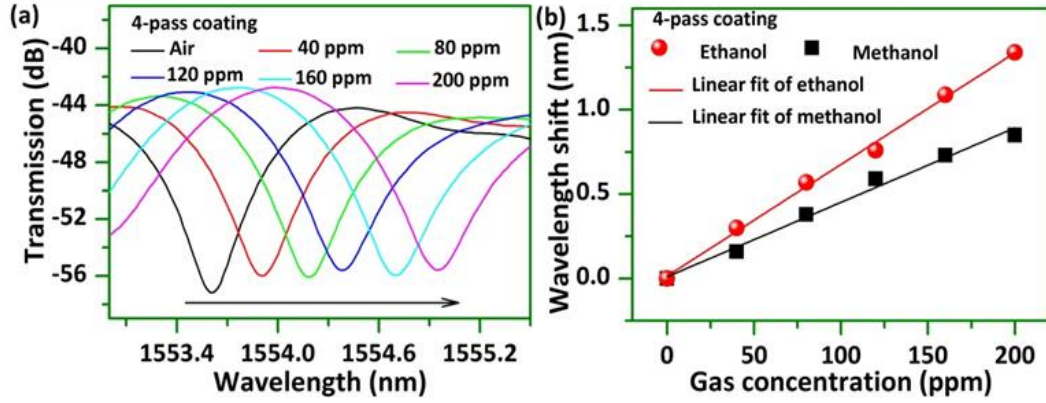


Figure 38. (a) Normalized measured spectral responses at different concentrations of ethanol for a TSCSMF based 4-pass coating sensor; and (b) corresponding measured wavelength shifts for different VOCs and concentrations.

Solving the matrix for the VOCs concentrations we obtain:

$$\begin{bmatrix} C_e \\ C_m \end{bmatrix} = \begin{bmatrix} 108 & -135 \\ -189 & 486 \end{bmatrix} \cdot \begin{bmatrix} \Delta W_T \\ \Delta W_M \end{bmatrix} \quad (3.3)$$

As can be seen from the above matrix, by measuring the wavelength shifts for both TSCSMF sensors, two different gases concentrations can be calculated. Using this method, multiple VOCs detection can potentially be realized if a larger number of sensors coated with different recipes are used.

Finally it should be noted that, similar to many other sensors, the proposed sensor suffers from cross sensitivity issues, for example, to temperature, humidity and non-target gases which will introduce measurement errors. However with the technique proposed in this paper, it is possible to use different coating materials to measure the sensors' response to specific influences and then use the commonly report technique to construct a matrix with specific cross-sensitivity coefficients and to realize accurate measurements of the target gases concentrations.

3.3.5 Conclusions

In conclusion, TSCSMF and MFC based optical fiber sensors for the detection of methanol and ethanol are proposed and experimentally demonstrated. Coating mixtures of sol-gel silica and Nile red with two different preparation recipes are investigated. Coatings prepared by recipe I were applied to both TSCSMF and MFC samples surfaces. Experimental results show that the sensor based on an MFC shows much better sensitivity of -0.130 nm/ppm to ethanol and -0.036 nm/ppm to methanol than those of the TSCSMF based sensor. The corresponding minimum detectable concentration change are up to 77 ppb and 281 ppb for ethanol and methanol respectively. The response and recovery behaviors in time of the sensors were also investigated. The response time is demonstrated to be less than 5 minutes, while the recovery time varies from 7 minutes to 12 minutes depending on the type of gas and gas concentrations. Both sensors are also proved to have good repeatability of performance. In addition, to investigate the potential for simultaneous measurement of two VOCs, another TSCSMF structure coated with a layer by recipe II was fabricated. A second-order matrix technique was then employed to permit simultaneous measurement of methanol and ethanol concentrations by utilizing both TSCSMF based sensors prepared with different coating recipes.

3.3.6 References

- [138] K. Demeestere, J. Dewulf, B. De Witte, and H. Van Langenhove, "Sample preparation for the analysis of volatile organic compounds in air and water matrices," *Journal of Chromatography A*, vol. 1153, no. 1–2. pp. 130–144, 2007.
- [139] K. Cherif, J. Mrazek, S. Hleli, V. Matejec, A. Abdelghani, M. Chomat, N.

- Jaffrezic-Renault, I. Kasik, "Detection of aromatic hydrocarbons in air and water by using xerogel layers coated on PCS fibers excited by an inclined collimated beam," in *Sensors and Actuators, B: Chemical*, 2003, vol. 95, no. 1–3, pp. 97–106.
- [140] G. Orellana and D. Haigh, "New trends in fiber-optic chemical and biological sensors," *Curr. Anal. Chem.*, vol. 4, no. 4, pp. 273–295, 2008.
- [141] D. Liu, T. Liu, H. Zhang, C. Lv, W. Zeng, and J. Zhang, "Gas sensing mechanism and properties of Ce-doped SnO₂ sensors for volatile organic compounds," *Mater. Sci. Semicond. Process.*, vol. 15, no. 4, pp. 438–444, 2012.
- [142] M. J. Fernández, J. L. Fontecha, I. Sayago, M. Aleixandre, J. Lozano, J. Gutiérrez, I. Gfacia, C. Cané, and M. C. Horrillo, "Discrimination of volatile compounds through an electronic nose based on ZnO SAW sensors," *Sensors Actuators, B Chem.*, vol. 127, no. 1, pp. 277–283, 2007.
- [143] B. Li, G. Sauve', M.C. Iovu, M. Jeffries-EL, R. Zhang, J. Cooper, S. Santhanam, L. Schultz, J.C. Revelli, A.G. Kusne, T. Kowalewski, J.L. Snyder, L.E. Weiss, G.K. Fedder, and D.N. Lambeth, "Volatile organic compound detection using nanostructured copolymers," *Nano Lett.*, vol. 6, no. 8, pp. 1598–1602, 2006.
- [144] N. A. Rakow and K. S. Suslick, "A colorimetric sensor array for odour visualization," *Nature*, vol. 406, no. 6797, pp. 710–713, 2000.
- [145] R. Lu, W. Li, B. Mizaikoff, A. Katzir, Y. Raichlin, G. Sheng and H. Yu, "High-sensitivity infrared attenuated total reflectance sensors for in situ multicomponent detection of volatile organic compounds in water," *Nature Protocols*, vol. 11, no. 2, pp. 377–386, 2016.
- [146] M. R. R. Khan, B. H. Kang, S. H. Yeom, D. H. Kwon, and S. W. Kang, "Fiber-optic pulse width modulation sensor for low concentration VOC gas," *Sensors Actuators, B Chem.*, vol. 188, pp. 689–696, 2013.
- [147] C. Elosua, I. Vidondo, F. J. Arregui, C. Bariain, A. Luquin, M. Laguna, I. R. Matias, "Lossy mode resonance optical fiber sensor to detect organic vapors," *Sensors Actuators, B Chem.*, vol. 187, pp. 65–71, 2013.
- [148] M. G. Manera, G. Leo, M. L. Curri, P. D. Cozzoli, R. Rella, P. Siciliano, A. Agostiano, L. Vasanelli, "Investigation on alcohol vapours/TiO₂ nanocrystal thin films interaction by SPR technique for sensing

- application,” *Sensors Actuators, B Chem.*, vol. 100, no. 1–2, pp. 75–80, 2004.
- [149] A. Dikovska, G. Tanasova, N. Nedyalkov, P. Stefanov, P. Atanasov, E. Karakoleva, A. Andreev, “Optical sensing of ammonia using ZnO nanostructure grown on a side-polished optical-fiber,” *Sensors Actuators, B Chem.*, vol. 146, no. 1, pp. 331–336, 2010.
- [150] S. K. Mishra, D. Kumari, and B. D. Gupta, “Surface plasmon resonance based fiber optic ammonia gas sensor using ITO and polyaniline,” *Sensors Actuators, B Chem.*, vol. 171–172, pp. 976–983, 2012.
- [151] X. Ning, C. Zhao, F. Shi, and S. Jin, “Multipoint chemical vapor measurement by zeolite thin film-coated Fresnel reflection-based fiber sensors with an Array-Waveguide Grating,” *Sensors Actuators, B Chem.*, vol. 227, pp. 533–538, 2016.
- [152] C. Yu, Y. Wu, C. Li, F. Wu, J. Zhou, Y. Gong, Y. Rao, and Y. Chen, “Highly sensitive and selective fiber-optic Fabry-Perot volatile organic compounds sensor based on a PMMA film,” *Opt. Mater. Express*, vol. 7, no. 6, pp. 2111–2116, 2017.
- [153] X. Ning, J. Yang, C. L. Zhao, and C. C. Chan, “PDMS-coated fiber volatile organic compounds sensors,” *Appl. Opt.*, vol. 55, no. 13, pp. 3543–3548, 2016.
- [154] C. Bariáin, I. R. Matías, I. Romeo, J. Garrido, and M. Laguna, “Detection of volatile organic compound vapors by using a vapochromic material on a tapered optical fiber,” *Appl. Phys. Lett.*, vol. 77, no. 15, pp. 2274–2276, 2000.
- [155] Y. Q. Chen and C. J. Lu, “Surface modification on silver nanoparticles for enhancing vapor selectivity of localized surface plasmon resonance sensors,” *Sensors Actuators, B Chem.*, vol. 135, no. 2, pp. 492–498, 2009.
- [156] J. Hromadka, M. C. Partridge, S. W. James, F. Davis, D. Crump, S. Korposh, R. Tatam, “Multi-parameter measurements using optical fibre long period gratings for indoor air quality monitoring,” *Sensors Actuators, B Chem.*, vol. 244, pp. 217–225, 2017.
- [157] S. Tao, L. Xu, and J. C. Fanguy, “Optical fiber ammonia sensing probes using reagent immobilized porous silica coating as transducers,” *Sensors Actuators, B Chem.*, vol. 115, no. 1, pp. 158–163, 2006.

- [158] D. Liu, W. Han, A. K. Mallik, J. Yuan, C. Yu, G. Farrell, Y. Semenova, and Q. Wu, "High sensitivity sol-gel silica coated optical fiber sensor for detection of ammonia in water," *Opt. Express*, vol. 24, no. 21, pp. 24179–24187, 2016.
- [159] J. C. Echeverría, M. Faustini, and J. J. Garrido, "Effects of the porous texture and surface chemistry of silica xerogels on the sensitivity of fiber-optic sensors toward VOCs," *Sensors Actuators, B Chem.*, vol. 222, pp. 1166–1174, 2016.
- [160] J. Estella, J. C. Echeverría, M. Laguna, and J. J. Garrido, "Silica xerogels of tailored porosity as support matrix for optical chemical sensors. Simultaneous effect of pH, ethanol:TEOS and water:TEOS molar ratios, and synthesis temperature on gelation time, and textural and structural properties," *J. Non. Cryst. Solids*, vol. 353, no. 3, pp. 286–294, 2007.
- [161] J. Estella, J. C. Echeverría, M. Laguna, and J. J. Garrido, "Effects of aging and drying conditions on the structural and textural properties of silica gels," *Microporous Mesoporous Mater.*, vol. 102, no. 1–3, pp. 274–282, 2007.
- [162] D. Liu, A. K. Mallik, J. Yuan, C. Yu, G. Farrell, Y. Semenova, and Q. Wu, "High sensitivity refractive index sensor based on a tapered small core single-mode fiber structure," *Opt. Lett.*, vol. 40, no. 17, pp. 4166–4169, 2015.
- [163] L. Sun, Y. Semenova, Q. Wu, D. Liu, J. Yuan, T. Ma, X. Sang, B. Yan, K. Wang, C. Yu, and G. Farrell, "High sensitivity ammonia gas sensor based on a silica-gel-coated microfiber coupler," *J. Light. Technol.*, vol. 35, no. 14, pp. 2864–2870, 2017.
- [164] Q. Wu, Y. Semenova, P. Wang, G. Farrell, "A comprehensive analysis verified by experiment of a refractometer based on an SMF28-small-core singlemode fiber (SCSMF)-SMF28 fiber structure," *J. Opt.*, vol. 13, no. 12, pp. 125401, 2011.
- [165] A. W. Snyder, "Coupled mode theory for optical fibers," *J. Opt. Soc. Am.*, vol. 62, no. 11, pp. 1267–1277, 1972.
- [166] C. Reichardt, "Solvatochromic dyes as solvent polarity indicators," *Chem. Rev.*, vol. 94, no. 8, pp. 2319–2358, 1994.
- [167] J. F. Deye, T. A. Berger, and A. G. Anderson, "Nile red as a

solvatochromic dye for measuring solvent strength in normal liquids and mixtures of normal liquids with supercritical and near critical fluids,” *Anal. Chem.*, vol. 62, no. 6, pp. 615–622, 1990.

- [168] M. R. R. Khan and S. W. Kang, “A high sensitivity and wide dynamic range fiber-optic sensor for low-concentration VOC gas detection,” *Sensors (Switzerland)*, vol. 14, no. 12, pp. 23321–23336, 2014.
- [169] M. Kubeckova, M. Sedlar, and V. Matejec, “Characterization of sol-gel derived coatings on optical fibers,” *J. Non. Cryst. Solids*, vol. 147–148, no. C, pp. 404–408, 1992.

Chapter 4

Hollow core fiber based interferometer sensors

It is well known that for an optical fiber sensor which utilizes that influence of a measurand on the position of a spectral dip or peak, the Q factor of the spectral dip or peak significantly influences the highest achievable measurement accuracy. In Chapter 3, high sensitivity fiber sensors were fabricated based on tapered fiber interferometers. However, the spectral Q factor for such sensors is still relatively low, typically in the order of $\sim 10^2$. Therefore, the primary aim of the research in this Chapter is to develop a fiber structure with a higher Q factor and explore its applications.

Fiber structures based on resonant structures, such as FPIs or whispering gallery mode resonators have high spectral Q factors. However, such devices usually suffer from a narrow measurement range. In addition, in such sensors there is a need to very precisely control the size of the microcavity, with control in the order of micrometers, as small variations in the cavity length or diameter will result in significant changes to the actual spectrum achieved by comparison to the intended spectrum. Most recently, a modified SMS structure prepared by incorporating a section of HCF between two SMFs was proposed with relatively large Q factor in the order of $\sim 10^3$ was achieved [170]. However the influence of the length of the HCF on transmission spectral dips' Q factors and transmission attenuation has not been investigated to date. In addition in the previous reports, the experimental results show a large variation in transmission dips' positions

with changes in the length of HCF structure, which disagrees with the theoretical calculation. The disparity may be attributed to the relatively large core diameter of the fiber chosen, which makes it difficult to fabricate and reproduce such an HCF based fiber structure. In this Chapter, two published journal papers are presented, with a more comprehensive investigation on the HCF based fiber structure and the problems mentioned above carried out to better understand this structure and explore its applications.

In the first publication of this chapter, light propagation inside the HCF based structure is studied experimentally, a theoretical model based on multiple beam interferences is also proposed. The developed high-Q (in the order of $\sim 10^4$) HCF structure is used for high temperature (up to 1000 °C) measurement. In comparison with commercial FBG temperature sensors, the proposed HCF based structure shows a competitive Q factor in its transmission spectrum but with an improved temperature sensitivity, a lower strain sensitivity and a wider working temperature range. The demonstrated sensor has the additional advantages of low cost and a simple and flexible fabrication process that offers a great potential for practical applications.

The proposed HCF based structure not only offers a spectrum with high Q feature, but also a large extinction ratio which is influenced by the reflection coefficients at the inner and outer interfaces between the air and the silica cladding. In the second publication of this chapter, the development of a novel twist sensor is investigated by introducing a partial silver coating on the outer surface of the HCF to introduce the asymmetry of RI distribution and high birefringence. Different silver coating thicknesses have been studied; it is found that the normalized spectral dips after coating have a tendency moving to the

longer wavelength with the increase of the coating thickness. A maximum twist sensitivity of 0.717 dB/° has been experimentally demonstrated, which is the highest twist sensitivity reported to date for optical fiber sensors based on an intensity modulation technique.

4.1 Hollow core fiber based interferometer for high temperature (1000 °C) measurement⁵

Abstract: A simple, cost effective high temperature sensor (up to 1000 °C) based on a hollow core fiber (HCF) structure is reported. It is configured by fusion splicing a short section of HCF with a length of few millimeters between two standard single mode fibers (SMF-28). Due to multiple beam interference introduced by the cladding of the HCF, periodic transmission dips with high spectral extinction ratio and high quality (Q) factor are excited. However, theoretical analysis shows that minor variations of the HCF cladding diameter may result in a significant decrease in the Q factor. Experimental results demonstrate that the position of periodic transmission dips are independent of the HCF length, but spectral Q factors and transmission power varies with different HCF lengths. A maximum Q factor of 3.3×10^4 has been demonstrated with large free spectral range of 23 nm and extinction ratio of 26 dB. Furthermore, the structure is proved to be an excellent high temperature sensor with advantages of high sensitivity (up to 33.4 pm/°C), wide working temperature range (from room temperature to 1000°C), high resolution, good stability, repeatability, relatively

⁵ D. Liu*, Q. Wu*, C. Mei, J. Yuan, X. Xin, A. K. Mallik, F. Wei, W. Han, R. Kumar, C. Yu, S. Wan, X. He, B. Liu, G.D. Peng, Y. Semenova, and G. Farrell, "Hollow Core Fiber Based Interferometer for High Temperature (1000 °C) Measurement," *Journal of Lightwave Technology*, vol. 36, no. 9, pp.1583-1590, 2018. (*D. Liu and Q. Wu contributed equally to this work.)

low strain sensitivity ($0.46 \text{ pm}/\mu\epsilon$), low cost and a simple and flexible fabrication process that offers a great potential for practical applications. A thorough theoretic analysis of the HCF based fiber structure has been proposed. The experimental results are demonstrated to be well matched with our simulation results.

Index Terms—Temperature sensors, optical fiber sensors, optical spectroscopy, optical interferometry, optical fiber applications

4.1.1 Introduction

Optical fiber sensors have been widely studied due to their well-known advantages such as miniature size, immunity to electromagnetic interference, a high resistance to corrosive environments, fast response and remote sensing capabilities, which gives them a great potential to be used in many applications including refractive index sensing, bio-chemical sensing, large civil structures structural health monitoring, and gas exploration [171-175]. Some of these applications require the sensors to have the ability to work at very high temperatures with good stability and accuracy. Previously reported optical fiber based temperature sensors can be mainly categorized into two types depending on the physical principle of sensor operation. One type is grating based temperature sensors while the other type are sensors whose operation is based on interferometry. Among these different types of temperature sensors, fiber Bragg grating (FBG) based temperature sensors are the most developed and reliable temperature sensors in real-life applications because of their unique advantages of high quality factor (Q factor, usually larger than 10^4) and multiplexing features [176]. However, the traditional Type I grating based FBG introduced by

moderate UV exposures can be easily erased under high temperature, so it can only be used for relatively low temperature applications (usually below 200 °C). By utilizing an intensive UV laser source or femtosecond pulse duration infrared (fs-IR) laser source, other types of gratings can be inscribed. The working temperature of these kinds of grating sensors can be extended to over 1000 °C [177-179]. However, the fabrication process for such gratings is rather complicated and expensive [180]. Interferometer based temperature sensors, on the other hand, have the advantages of a relatively simple fabrication process, a much lower cost and can be fabricated for example by tapering or combining different optical fiber structures. Based on a variety of different fiber structure configurations, a number of interferometer based sensors have been proposed for high temperature sensing, such as those based on multimode fibers, thin core fibers, microcavities, microchannels, twin core, multi core fibers, and photonic crystal fibers (PCF) [181-187]. Multimode and thin core fiber based temperature sensors show poor spectral Q factors and hence the temperature measurement accuracy is relatively low. Microcavity and microchannel based Fabry-Perot interferometer (FPI) temperature sensors could achieve higher Q factors but with extremely smaller channel spacing and hence narrow measurement range [188]. Besides, the fabrication of such microcavities or microchannels typically requires high cost equipment such as a femtosecond laser. PCF based temperature sensors have also attracted lot of interest recently, but they suffer from the disadvantages of large insertion loss, low fringe visibility and high cost.

Hollow core fiber (HCF) is attracting more and more research interest, for example, as a means to incorporate an air-gap microcavity in the HCF to form an FPI for sensing applications [189-191]. In FPI based sensors there is a need to

very precisely control the size of the microcavity in the order of micrometers, as small variations in the cavity length will result in significant changes to the actual spectrum achieved by comparison to the intended spectrum. Moreover, most of the air gap FPI based temperature sensors have a very limited temperature sensitivity ($\sim 1 \text{ pm}/^\circ\text{C}$) [192-194] and contamination from dust and other pollutants is a significant issue for the long term stability of the sensor, due to a structure that is typically open to the environment [181]. Recently, functionalized HCF based interferometer structures has been reported for use as a biosensor, a magnetic field sensor, a humidity sensor and a displacement sensor [170,195-197]. These reports demonstrated very useful applications of a HCF based interferometer, but to date there has been a lack of in-depth analysis of the structure.

In this article, we propose and investigate a single HCF ($\sim 30 \text{ }\mu\text{m}$ inner diameter, $\sim 126 \text{ }\mu\text{m}$ outer diameter) based multiple beam interferometer for high temperature sensing, where a short section of HCF is fusion spliced between two traditional singlemode fibers (SMF28). The proposed structure demonstrates a high spectral extinction ratio (over 26 dB), high Q factor (3.3×10^4), wide working temperature range (up to 1000°C), a high temperature sensitivity of $34.3 \text{ pm}/^\circ\text{C}$ and a relatively low strain sensitivity of about $0.46 \text{ pm}/\mu\epsilon$. The demonstrated sensor has the advantages of low cost and a simple and flexible fabrication process that offers a great potential for practical applications.

4.1.2 Theoretical model and analysis

A schematic diagram of the proposed SMF28-HCF-SMF28 fiber structure is shown in Fig. 39(a). A microscope image is also presented in Fig. 39(b) to

illustrate the splice condition at the transition region between the SMF28 and HCF. When light is transmitted from the SMF28 to the HCF, the light energy within the SMF28 core is not fully guided mode within the HCF since the diameter of the air core ($\sim 30\ \mu\text{m}$) of the HCF is larger than that of the SMF28 ($\sim 8.2\ \mu\text{m}$) and the refractive index of the air core is much smaller than that of the silica cladding of the HCF. Light that reaches the silica cladding of the HCF propagates within the cladding, given that the cladding is surrounded an air with a lower refractive index. As illustrated in Fig. 39(a), the incident light from the SMF28 will be reflected at both the interface between the inner air/cladding and outer air/cladding, resulting in multiple beam interferences within the HCF. After experiencing the multiple beam interference in the HCF cavity light will ultimately be transmitted to the output SMF28. Since the fiber has a symmetric cylindrical structure, the light interference and transmission are illustrated in Fig. 39(a) but only for the top half of the structure for the sake of clarity.

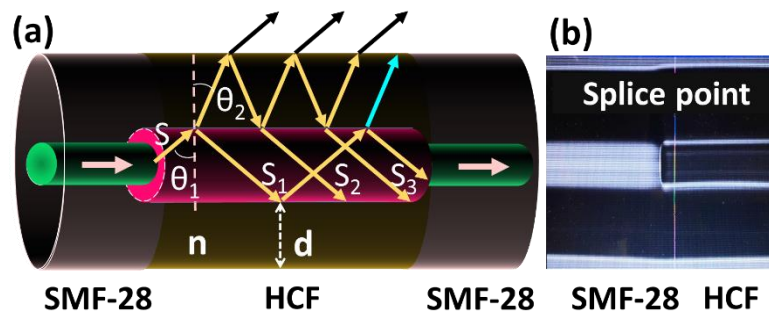


Figure 39. (a) A schematic diagram of the proposed SMF28-HCF-SMF28 fiber structure, and (b) a microscope image showing an example of the transition region between the SMF28 and HCF after splicing.

Assuming the input light (S) has an amplitude A with an incident angle θ_1 and a refractive angle θ_2 , the HCF cladding thickness is d and the refractive index is n , then the phase difference between the two adjacent reflected light rays

inside the air core of the HCF (S1, S2, S3...) is $\delta = \frac{4\pi}{\lambda} n d \cos\theta_2$. The complex amplitude of the reflected light S1, S2, S3... can be expressed as

$$r_1 A, t_1 t_2 r_2 A e^{i\delta}, t_1 t_2 r_2^3 A e^{i2\delta}, \dots, t_1 t_2 r_2^{2p-3} A e^{i(p-1)\delta}, \dots$$

where r_1, r_2 are the coefficients of reflection at the interfaces between the inner air/cladding and cladding/outer air respectively which can be calculated by the Fresnel equations:

$$TE \text{ mode } r_1 = \frac{\cos\theta_1 - n \cos\theta_2}{\cos\theta_1 + n \cos\theta_2}, r_2 = -r_1 \quad (4.1)$$

$$TM \text{ mode } r_1 = \frac{\cos\theta_2 - n \cos\theta_1}{\cos\theta_2 + n \cos\theta_1}, r_2 = -r_1 \quad (4.2)$$

t_1, t_2 are the coefficients of refraction at the interface between the inner air/cladding and cladding/outer air respectively.

$$t_1 = t_2 \quad (4.3)$$

$$t_1^2 + r_1^2 = 1 \quad (4.4)$$

If there are p reflected light rays, where $p = \frac{L}{2d \tan\theta_2}$, L is the length of the HCF fiber, then the amplitude of reflected light can thus be expressed as:

$$A_r = r_1 A + t_1 t_2 r_2 A e^{i\delta} + t_1 t_2 r_2^3 A e^{i2\delta} + \dots + t_1 t_2 r_2^{2p-3} A e^{i(p-1)\delta} + \dots \quad (4.5)$$

The intensity of light reflected by the HCF cladding is hence

$$I_r = |A_r|^2 \quad (4.6)$$

Simulations based on the above analysis were carried out. In the simulation, we assume the SMF28 has core and cladding refractive indices of 1.452 and 1.449 at a wavelength of 1550 nm respectively and a core diameter of 8.2 μm ; the HCF has an air core diameter of 30 μm and cladding diameter of 126 μm with the length of 5 mm and only TE mode was considered. The refractive index of the HCF cladding is wavelength dependent,

$$n = \sqrt{1 + \frac{0.6961663\lambda^2}{\lambda^2 - 0.0684043^2} + \frac{0.4079426\lambda^2}{\lambda^2 - 0.1162414^2} + \frac{0.8974794\lambda^2}{\lambda^2 - 9.896161^2}} \quad [198], \text{ where } \lambda \text{ is}$$

the wavelength in μm , a typical refractive index at the wavelength of 1550 nm is 1.444.

Figure 40 shows the simulated spectral response of the SMF-HCF-SMF fiber structure, based on the analysis above. As one can see from Fig. 40(a), the output spectrum of this structure has multiple high Q transmission dips and a relatively large free spectral range (FSR) of about 23 nm around 1540 nm, making the proposed SMF-HCF-SMF structure advantageous as a very narrow bandwidth optical filter or as a sensor with high accuracy (due to the high Q factor) and a wide working range (due to the large FSR). In practice, the HCF cladding diameter fluctuates very slightly, as a result of the limitations in the manufacturing process, which could have a significant influence on the transmission spectrum of the SMF-HCF-SMF structure. Figure 40(b) shows a simulation result of the spectral response of the structure containing HCF section with random fiber cladding diameter variations of ± 10 nm ($d = 48 \pm b \times 0.01 \mu\text{m}$, where b is a random number between 0 and 1). It is clear that the cladding diameter variations have a significant influence on the output spectrum, resulting in a degraded Q factor of 3.15×10^4 , which in fact is still relatively high compared to most optical fiber based interferometers, even compared with a typical fiber Bragg grating which has a 3 dB bandwidth of 0.1 nm with a Q factor of 1.55×10^4 . Figure 40(c) shows in simulation the relationship between Q and the HCF cladding diameter variation amplitude. It can be seen that the HCF cladding diameter variation has a significant influence on the Q factor of the structure. When the amplitude of the cladding diameter variation increases from 2 nm to 20 nm, the Q factor decreases from 8.13×10^5 to 7.9×10^3 . The influence of

temperature on the physical properties of an optical fiber manifests itself as both changes of refractive index and changes in fiber dimensions. The values of the changes in each of the properties are further determined by the two fiber material's parameters: the thermal expansion coefficient (TEC) and the thermo-optic coefficient (TOC). For the structure presented here, assuming the HCF has a cladding diameter D , length L and refractive index n , the corresponding changes of these parameters due to a temperature variation (ΔT) can be expressed, respectively, as

$$D_T = D_0 + \alpha \cdot D_0 \cdot \Delta T \quad (4.7)$$

$$L_T = L_0 + \alpha \cdot L_0 \cdot \Delta T \quad (4.8)$$

$$n_T = n_0 + \xi \cdot n_0 \cdot \Delta T \quad (4.9)$$

where α and ξ are the TEC and the TOC, respectively.

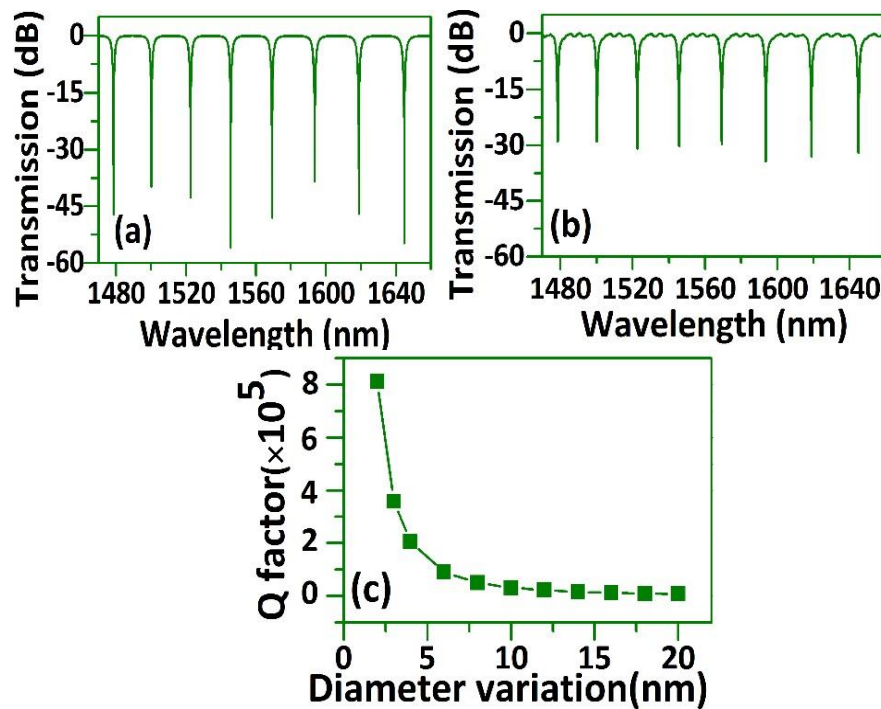


Figure 40. Simulated spectral response of the SMF-HCF-SMF fiber structure (a) no diameter variation (b) HCF cladding diameter variation amplitude of ± 10 nm and (c) Q factor vs. amplitude of HCF cladding diameter variation.

Figure 41 presents the simulation results for the wavelength of one of the transmission dips versus temperature. In the simulation, $\alpha = 5 \times 10^{-7} / ^\circ\text{C}$ and $\xi = 8.6 \times 10^{-6} / ^\circ\text{C}$. As the temperature increases, the spectral wavelength red-shifts linearly and monotonically toward the longer wavelengths. The calculated sensitivity is about 25 pm/ $^\circ\text{C}$ over a wide temperature range from 0 to 900 $^\circ\text{C}$.

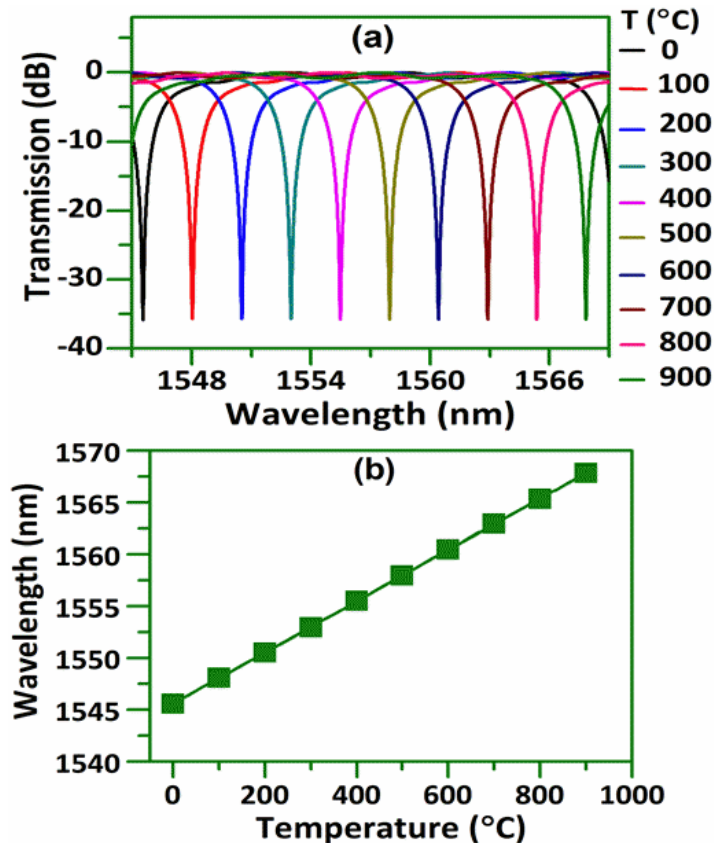


Figure 41. (a) Simulated transmission responses of the SMF-HCF-SMF fiber structure at different temperatures; and (b) the corresponding spectral shift of a selected transmission dip versus temperature.

Experimental investigation of the temperature influence on the HCF based structure has been carried out. Figure 42 shows a schematic diagram of the experimental setup for temperature/strain measurements. Two ends of SMF-28 are fixed on two manual translation stages and the short section of HCF which is spliced between these two SMF acting as the sensor head is placed straight inside

the central heating zone of a ceramic microheater. The temperature of the microheater is controlled by a programmable DC current controller.

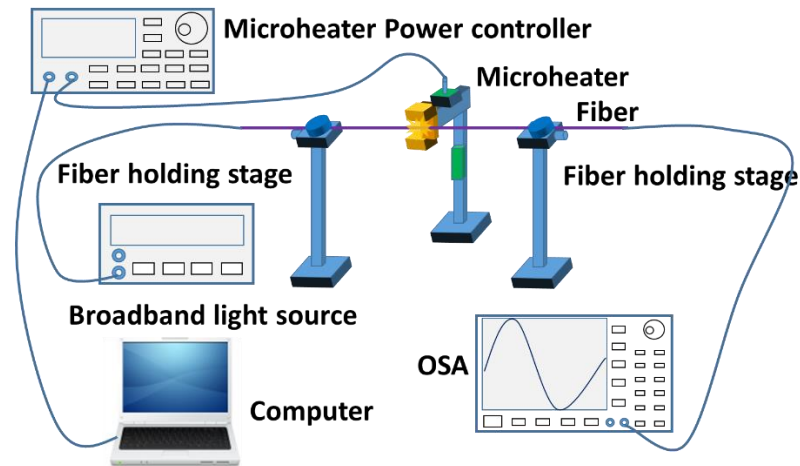


Figure 42. Schematic diagram of the experimental setup for temperature and strain measurements.

4.1.3 Results and discussion

Figure 43(a) shows the experimentally measured transmission spectral responses of the proposed structures with different lengths of HCF. As one can see from the figure, a range of sharp transmission dips are observed over the wavelength range from 1493 to 1593 nm, which agrees well with our above simulation results. As the length of the HCF increases from 3.5 mm to 8.5 mm, the transmission loss increases, the estimated Q factor values for the experimentally recorded spectral responses (for dip 2) are about 7.3×10^3 , 3.3×10^4 , 1.3×10^4 and 1.1×10^4 , respectively, demonstrating that high Q factors can be achieved experimentally. The measured FSR around the wavelength of 1540 nm range is circa 23 nm, which matches very well with the simulation result. Figure 43(a) also shows that the minimum transmission loss of the structure is about 5 dB corresponding to a sample with a HCF length of 3.5 mm. The loss is possibly due to the following two factors: 1) the light absorption/ scattering at the interface

between HCF cladding and air; 2) the SMF fiber has much smaller diameter (8.2 μm) compared to that of HCF air core (30 μm), so that not all the power transmitted in the HCF air core will be coupled to the output SMF. The loss due to the above factors can be reduced by replacing the output SMF with a larger core diameter multimode fiber (MMF), which has been verified by our additional experiment, where the transmission loss was reduced by about 2.5 dB as shown in Fig. 43(b) by replacing SMF28 with MMF with a core diameter of 62.5 μm .

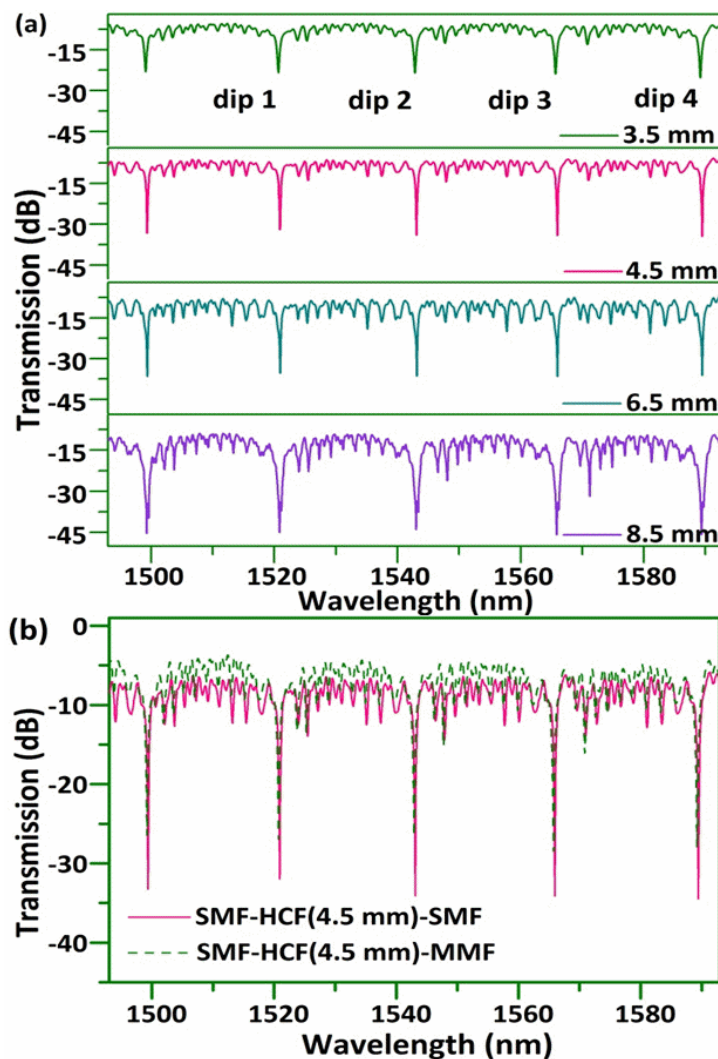


Figure 43. Measured transmission spectra for HCF based fiber structure with (a) different lengths of HCF and (b) different output fiber types of SMF and MMF.

It should be noted also that the wavelengths of the spectral dips remain almost unchanged for the structures with different lengths of HCF, which

indicates that the spectral dip wavelength of the transmission is independent of the HCF length. This is due to the fact that the interference wavelength dip is caused by the multiple beam interferences taking place within the hollow core of the HCF. The unique property makes the fabrication of this device more repeatable.

The temperature dependence of the HCF based structure has been experimentally investigated. In our experiments, a sensor with a length of circa 3.5 mm of HCF is chosen for the test. Since the microheater used in our setup has a full length of heating zone of 19 mm, it is reasonable to assume that this microheater can provide a uniform temperature distribution over the whole length of the 3.5 mm HCF section.

As in initial set of tests, the sensor stability at high temperatures is monitored over a one hour period as shown in Fig. 44(a). The sensor demonstrates a very good stability when it is exposed to constant temperatures of 500 °C and 638 °C. When the temperature is further increased to a constant value of 777 °C, the optical spectrum undergoes a blue shift of circa 0.56 nm over 60 minutes. Further increases in the temperature to constant values of 900 °C and 1005 °C, result in the blue shift increase with time becoming more significant, which indicates the sensor's stability deteriorates with the long term exposure to higher temperatures, above 800 °C. This problem can be solved by introducing an annealing process which helps to eliminate the residual stress and thermal memory existing in the fiber structure [181, 199]. As shown in Fig. 44(a), after one cycle of a 65 hour annealing process at 900 °C and 1005 °C respectively, sensor stability has been significantly improved. Figure 44(b) shows a standard deviation plot for the spectral dip's variations during one hour period at different temperatures before

and after the annealing process, which clearly demonstrates that the sensor has a significantly improved stability after 65 hours of annealing. It is also acknowledged that the observed small variations in the temperature dependencies at higher temperatures could possibly be contributed by the microheater itself as a result of the perturbations caused by the local airflow or small fluctuations in the output of the DC current controller driving the microheater.

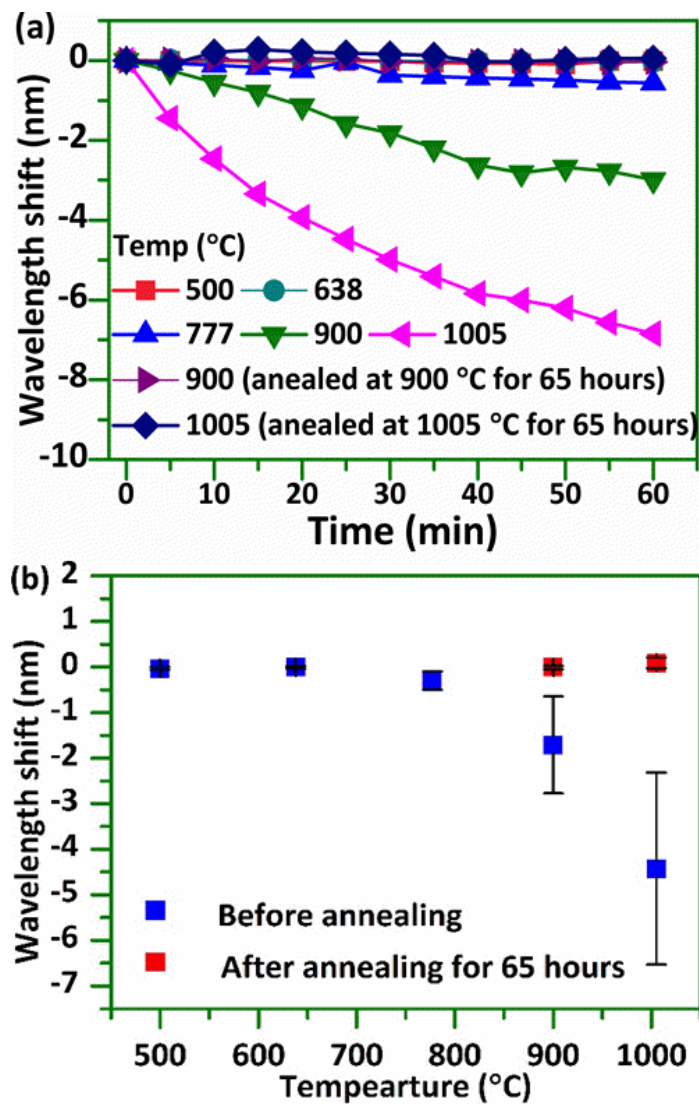


Figure 44. (a) HCF based sensor (HCF=3.5 mm) stability test and (b) the corresponding standard deviation plot in one hour period before and after the annealing process at different temperatures.

Following the temperature stability tests above, the temperature sensing performance for the sensor has been investigated. Initially this took place without an annealing process. As can be seen from Fig. 45(a), spectral dip 3 (marked in Fig. 43(a)) moves monotonically towards longer wavelengths as the temperature increases from room temperature to 500 °C. Each of the associated spectral dips corresponding to longer wavelengths display slightly improved temperature sensitivity.

The main graph in Fig. 45(b) shows the wavelength shift versus temperature for heating and cooling cycles for the same sensor which underwent three different annealing cases in sequence (no annealing (NA), then annealed at 900 °C (A900) and then subsequently annealed at 1005 °C (A1005)). For each annealing case, including no annealing, the sensor was characterized in terms of wavelength shift as a function of temperature over a range from room temperature up to a defined limit, as shown in Fig. 45(b). The sensor was also characterized for a decreasing temperature, from the upper limit of a range, back down to room temperature. The NA case used a measurement range from room temperature to 503 °C, as without annealing operation beyond circa 500 °C is not reliable. For the cases where the sensor was annealed at 900 °C and annealed at 1005 °C, the temperature range was from room temperature up to 899 °C, and up to 998 °C, respectively.

The results show that, for all the three different annealing cases, the measured wavelength shifts for the heating cycle match very well with those of the cooling cycle, indicating that this structure has very good repeatability for temperature measurement, with negligible evidence of hysteresis. From Fig. 45(b)

we can also see that, the temperature sensitivities are almost the same for all the sensors even after three different annealing processes.

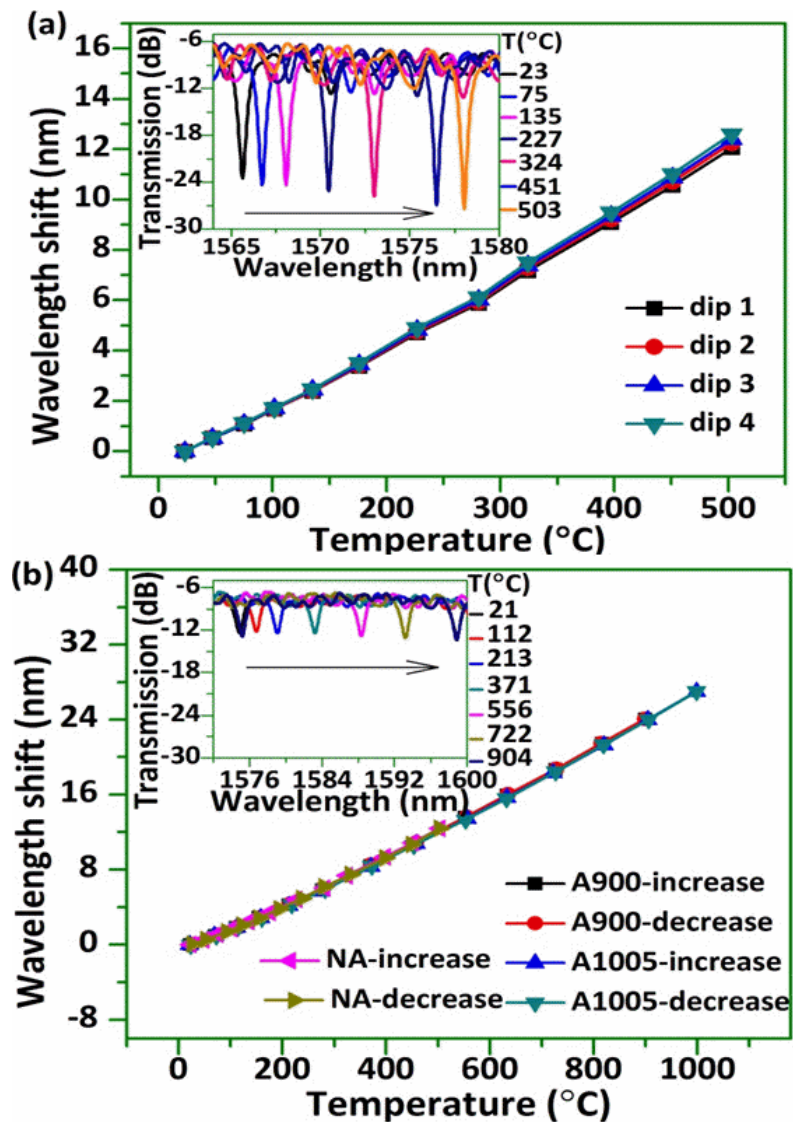


Figure 45. Wavelength shift versus temperature for HCF based sensor (HCF=3.5 mm): (a) dependencies for different dips within transmission spectrum for the sensor with no pre-annealing process and an example in the inset of the spectral response for dip 3 at different temperatures; (b) dependencies for the same transmission dip for all three different annealing processes and in the inset an example of spectral response at a selected dip for the sensor after annealing at 1005 °C for 65 hours.

The maximum temperature sensitivity of 33.4 pm/°C is achieved at the temperature around 1000 °C for the sensor after being annealed at 1005 °C, which is over two times higher than many temperature sensors reported recently

[179,183,1877]. It is noted that the measured maximum sensitivity is larger than our theoretically calculated temperature sensitivity of 25 pm/°C, this is possibly because the TOC (ξ) of the HCF cladding is temperature dependent and it has a higher value of ξ at high temperatures. Due to the large FSR, the annealed sensor can effectively measure temperature in very wide temperature range from room temperature to 1000 °C with excellent stability. The inset figure in Fig. 45(b) gives a spectral response vs. temperature for the sensor after annealed at 1005 °C for 65 hours, which shows similar wavelength shifting trend but with a reduced Q factor (5.1×10^3) and extinction ratio.

The influence of strain applied to the structure on its performance as a temperature sensor has also been investigated. In our experiment, the sensor which underwent annealing at 1005 °C is chosen for the strain test at different temperatures. For the sake of brevity, we only present the spectral responses to strain at room temperature and at 503 °C as shown in Fig. 46. It can be seen that wavelength shifts linearly with strain, and the strain sensitivities at both temperatures are almost the same, (0.64 pm/ $\mu\epsilon$ at 503 °C and 0.66 pm/ $\mu\epsilon$ at room temperature), indicating that the structure's strain sensitivity is temperature independent over a wide temperature range.

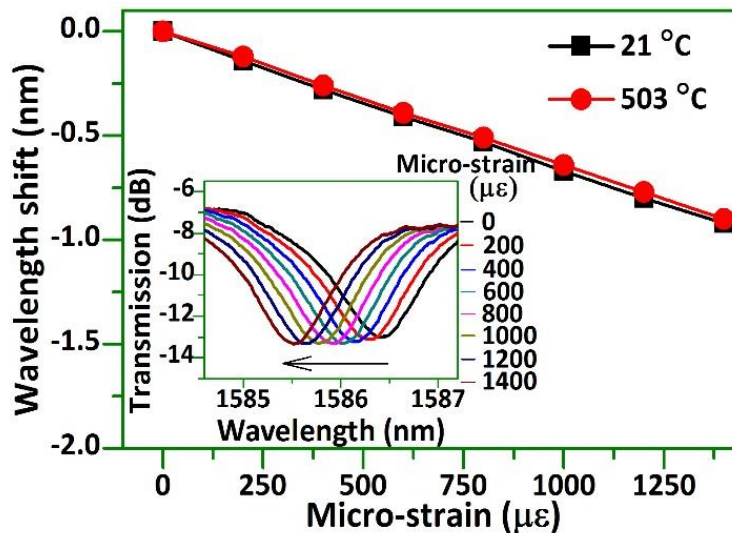


Figure 46. Spectral wavelength shift versus applied strain at 21 °C and 503 °C, and spectral responses to various strains at 503 °C for the sensor annealed at 1005 °C for 65 hours.

The influence of the HCF length on both the temperature and strain sensitivities of the sensor has also been studied and the results are shown in Fig. 47. Due to the limited heating length of the micro-heater it wasn't suitable for this experiment and so the influence of HCF length on temperature sensitivity was analyzed at lower temperatures by placing the fiber structure on a hotplate. It is clear from the figure that the HCF length has a limited influence on the temperature sensitivity. However, a greater length somehow shows a lower strain sensitivity of 0.46 pm/ $\mu\epsilon$, which is lower than many other fiber structures such as FBG (1.2 pm/ $\mu\epsilon$) [200], long-period fiber-grating (7.6 pm/ $\mu\epsilon$) [201] and hollow-core photonic crystal fiber (0.96 pm/ $\mu\epsilon$) [202]. Usually, a strain change will introduce the variation of fiber length and hence the optical length change, resulting spectral wavelength shifts. However, the spectral position of the interference dips does not change with fiber length in our case.

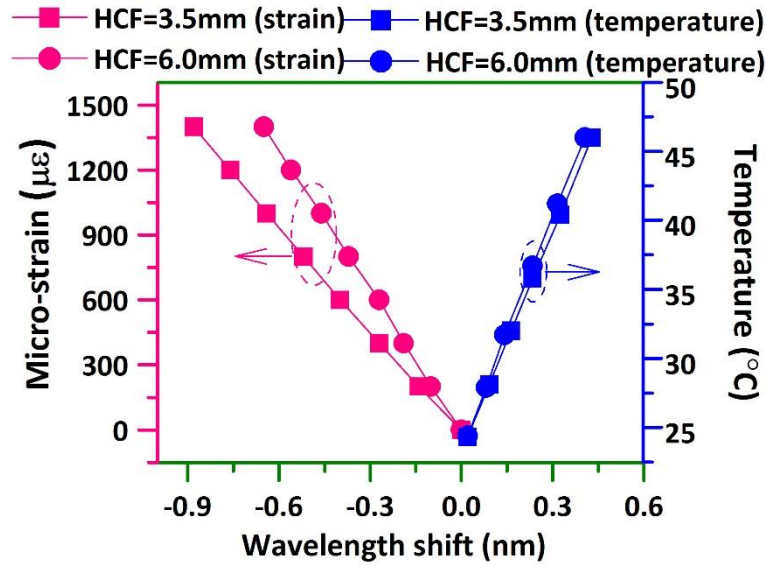


Figure 47. Influence of the HCF length on temperature and strain sensitivities of the proposed sensor.

4.1.4 Conclusion

In conclusion, a high temperature sensor based on a HCF based interferometer is proposed and investigated both theoretically and experimentally. It is found that the interferometer's transmission spectrum contains dips with a very high spectral extinction ratio and high Q factors due to multiple beam interference introduced by the hollow fiber cladding, but theoretical analysis shows that minor variations of the HCF cladding diameter may result in a significant decrease in the Q factor. Hence, accurate control of the fiber cladding diameter is critical to achieve high Q transmission dips. Experimentally, a range of periodic transmission dips with large spectral extinction ratio (~ 26 dB), large FSR (~ 23 nm) and high Q factor (3.3×10^4) were demonstrated based on the proposed fiber structure, which agrees very well with the simulation results. Experimental results also show that the length of HCF has influence on the spectral Q factor and transmission power, but it has no effects on position of the periodic transmission dips. The proposed HCF based structure has a maximum

temperature sensitivity of 33.4 pm/°C with good stability at 1005 °C after proper annealing process. In addition, the structure is relatively insensitive to strain with a sensitivity of circa 0.46 pm/με, which gives the sensor great potential for high temperature sensing. Due to the high Q factor of the structure, it has potential application as high accuracy bio-chemical sensor assuming proper functionalizing inner/outer surface of the HCF. It has many other advantages such as a simple configuration, ease of fabrication, low cost, and also excellent stability and repeatability.

4.1.5 References

- [170] R. Gao, Y. Jiang, and Y. Zhao, “Magnetic field sensor based on anti-resonant reflecting guidance in the magnetic gel-coated hollow core fiber,” *Opt. Lett.*, vol. 39, no. 21, pp. 6293–6296, 2014.
- [171] D. Liu, A. K. Mallik, J. Yuan, C. Yu, G. Farrell, Y. Semenova, and Q. Wu, “High sensitivity refractive index sensor based on a tapered small core single-mode fiber structure,” *Opt. Lett.*, vol. 40, no. 17, pp. 4166-4169, 2015.
- [172] W. Yu, T. Lang, J. Bian, and W. Kong, “Label-free fiber optic biosensor based on thin-core modal interferometer,” *Sensors Actuators, B Chem.*, vol. 228, pp. 322–329, 2016.
- [173] D. Liu, W. Han, A. K. Mallik, J. Yuan, C. Yu, G. Farrell, Y. Semenova, and Q. Wu, “High sensitivity sol-gel silica coated optical fiber sensor for detection of ammonia in water,” *Opt. Express*, vol. 24, no. 21, p. 24179–24187, 2016.
- [174] H. N. Li, D. S. Li, and G. B. Song, “Recent applications of fiber optic sensors to health monitoring in civil engineering,” *Eng. Struct.*, vol. 26, no. 11, pp. 1647–1657, 2004.
- [175] X. Jiang, K. Wang, J. Li, H. Zhan, Z. Song, G. Che, and G. L Yu, “Optical sensor of thermal gas flow based on fiber bragg grating,” *Sensors*, vol. 17, no. 2, p. 374, 2017.

- [176] A. D. Kersey, "Fiber grating sensors," *J. Light. Technol.*, vol. 15, no. 8, pp. 1442–1463, 1997.
- [177] B. Zhang and M. Kahrizi, "High-temperature resistance Fiber Bragg grating temperature sensor fabrication," *IEEE Sens. J.*, vol. 7, no. 4, pp. 586–591, 2007.
- [178] D. Grobnic, S. J. Mihailov, C. W. Smelser, and H. Ding, "Sapphire fiber bragg grating sensor made using femtosecond laser radiation for ultrahigh temperature applications," *IEEE Photonics Technol. Lett.*, vol. 16, no. 11, pp. 2505–2507, 2004.
- [179] H. Z. Yang, X. G. Qiao, S. Das, and M. C. Paul, "Thermal regenerated grating operation at temperatures up to 1400°C using new class of multimaterial glass-based photosensitive fiber," *Opt. Lett.*, vol. 39, no. 22, pp. 6438–6441, 2014.
- [180] L.-Y. Shao, T. Wang, J. Canning, K. Cook, and H.-Y. Tam, "Bulk regeneration of optical fiber Bragg gratings," *Appl. Opt.*, vol. 51, no. 30, p. 7165–7169, 2012.
- [181] J. E. Antonio-Lopez, Z. S. Eznaveh, P. LiKamWa, A. Schülzgen, and R. Amezcua-Correa, "Multicore fiber sensor for high-temperature applications up to 1000°C.," *Opt. Lett.*, vol. 39, no. 15, pp. 4309–4312, 2014.
- [182] J. J. Zhu, A. P. Zhang, T. H. Xia, S. He, and W. Xue, "Fiber-optic high-temperature sensor based on thin-core fiber modal interferometer," *IEEE Sens. J.*, vol. 10, no. 9, pp. 1415–1418, 2010.
- [183] Y. Liu, S. Qu, and Y. Li, "Single microchannel high-temperature fiber sensor by femtosecond laser-induced water breakdown.," *Opt. Lett.*, vol. 38, no. 3, pp. 335–337, 2013.
- [184] Y. Zhang, L. Yuan, X. Lan, A. Kaur, J. Huang, and H. Xiao, "High-temperature fiber-optic Fabry–Perot interferometric pressure sensor fabricated by femtosecond laser: erratum," *Opt. Lett.*, vol. 38, no. 22, pp. 4609–4612, 2013.
- [185] P. Rugeland and W. Margulis, "Revisiting twin-core fiber sensors for high-temperature measurements.," *Appl. Opt.*, vol. 51, no. 25, pp. 6227–6232, 2012.
- [186] G. Coviello, V. Finazzi, J. Villatoro, and V. Pruneri, "Thermally stabilized

- PCF-based sensor for temperature measurements up to 1000 degrees C.,” *Opt. Express*, vol. 17, no. 24, pp. 21551–21559, 2009.
- [187] C. Wu, H. Y. Fu, K. K. Qureshi, B.-O. Guan, and H. Y. Tam, “High-pressure and high-temperature characteristics of a Fabry–Perot interferometer based on photonic crystal fiber,” *Opt. Lett.*, vol. 36, no. 3, p. 412–414, 2011.
- [188] M. Bron and E. Wolf, *Principles of optics: Electromagnetic theory of propagation interference and diffraction of light*, Cambridge University Press, 1999.
- [189] C.-L. Lee, L.-H. Lee, H.-E. Hwang, and J.-M. Hsu, “Highly Sensitive air-gap fiber Fabry–Pérot interferometers based on polymer-filled hollow core fibers,” *IEEE Photonics Technol. Lett.*, vol. 24, no. 2, pp. 149–151, 2012.
- [190] C.-L. Lee, H.-Y. Ho, J.-H. Gu, T.-Y. Yeh, and C.-H. Tseng, “Dual hollow core fiber-based Fabry-Perot interferometer for measuring the thermo-optic coefficients of liquids,” *Opt. Lett.*, vol. 40, no. 4, pp. 459–462, 2015.
- [191] M. S. Ferreira, L. Coelho, K. Schuster, J. Kobelke, J. L. Santos, and O. Frazão, “Fabry-Perot cavity based on a diaphragm-free hollow-core silica tube.,” *Opt. Lett.*, vol. 36, no. 20, pp. 4029–4031, 2011.
- [192] D. W. Duan, Y. Rao, Y.-S. Hou, and T. Zhu, “Microbubble based fiber-optic Fabry–Perot interferometer formed by fusion splicing single-mode fibers for strain measurement,” *Appl. Opt.*, vol. 51, no. 8, pp. 1033–1036, 2012.
- [193] Y.-J. Rao, M. Deng, D.-W. Duan, X.-C. Yang, T. Zhu, and G.-H. Cheng, “Micro Fabry-Perot interferometers in silica fibers machined by femtosecond laser,” *Opt. Express*, vol. 15, no. 21, pp. 14123–14128, 2007.
- [194] T. Wei, Y. Han, H.-L. Tsai, and H. Xiao, “Miniaturized fiber inline Fabry-Perot interferometer fabricated with a femtosecond laser.,” *Opt. Lett.*, vol. 33, no. 6, pp. 536–538, 2008.
- [195] A. M. Zheltikov, “Ray-optic analysis of the (bio)sensing ability of ring-cladding hollow waveguides,” *Appl. Opt.*, vol. 47, no. 3, pp. 474–479, 2008.
- [196] R. Gao, D. F. Lu, J. Cheng, Y. Jiang, L. Jiang, and Z. M. Qi, “Humidity

- sensor based on power leakage at resonance wavelengths of a hollow core fiber coated with reduced graphene oxide,” *Sensors Actuators, B Chem.*, vol. 222, pp. 618–624, 2016.
- [197] R. Gao, D. F. Lu, J. Cheng, Y. Jiang, L. Jiang, and Z. M. Qi, “Optical displacement sensor in a capillary covered hollow core fiber based on anti-resonant reflecting guidance,” *IEEE J. Sel. Top. Quantum Electron.*, vol. 23, no. 2, pp. 1500106, 2017.
- [198] I. H. Malitson, “Interspecimen comparison of the refractive index of fused silica” *J. Opt. Soc. Am.*, vol. 55, no. 10, pp. 1205–1209, 1965.
- [199] D. Grobnic, C. W. Smelser, S. J. Mihailov, and R. B. Walker, “Long-term thermal stability tests at 1000 °C of silica fibre Bragg gratings made with ultrafast laser radiation,” *Meas. Sci. Technol.*, 2006, vol. 17, no. 5, pp. 1009–1013.
- [200] A. Othonos, “Fiber bragg gratings fiber bragg gratings,” *Rev. Sci. Instrum.*, vol. 68, no. 12, pp. 4309–4341, 1997.
- [201] Y. P. Wang, D. N. Wang, W. Jin, Y. J. Rao, and G. D. Peng, “Asymmetric long period fiber gratings fabricated by use of CO₂ laser to carve periodic grooves on the optical fiber,” *Appl. Phys. Lett.*, vol. 89, no. 15, pp. 151105, 2006.
- [202] S. H. Aref, R. Amezcua-Correa, J. P. Carvalho, O. Frazão, P. Caldas, J. L. Santos, F. M. Araújo, H. Latifi, F. Farahi, L. A. Ferreira, and J. C. Knight, “Modal interferometer based on hollow-core photonic crystal fiber for strain and temperature measurement,” *Opt. Express*, vol. 17, no. 21, pp. 18669–18675, 2009.

4.2 Highly sensitive twist sensor based on partially silver coated hollow core fiber structure⁶

Abstract: Interferometer based on multiple beam interferences inside a hollow core fiber (HCF) structure (also known as an anti-resonant reflecting optical waveguide) has been attracting interest of many researchers due to its periodic transmission spectrum containing high quality factor spectral dips. Functionalized HCF structures have been demonstrated for a wide range of applications in humidity, magnetic field and bio-sensing. Here, we report a new application of the HCF based structure with a partial silver coating layer for sensing of twist. It is configured by fusion splicing a section of 4.5-mm long HCF between two standard single mode fibers (SMFs), followed by a sputter-coating of a very thin layer of silver on one side of the HCF surface. It is found that the spectral response of the partially silver coated HCF structure is very sensitive to the changes of input light polarization. An increase in sensitivity of the fiber structure to twist after deposition of the silver coating when twist is applied to both the SMF and HCF sections is demonstrated by comparison with an uncoated HCF fiber structure. Experimental results show that twisting of the HCF section results in much greater changes in a selected dip's strength compared to that in the case of twisting the SMF section of the structure. The proposed HCF fiber sensors with 4.5 nm and 6.7 nm-thick silver layers show the highest sensitivities of 0.647 dB/° and 0.717 dB/° in the twist angles range of up to 10°. To the best of our knowledge, this is the highest twist sensitivity reported

⁶ D. Liu, R. Kumar, F. Wei, W. Han, A. K. Mallik, J. Yuan, S. Wan, X. He, Z. Kang, F. Li, C. Yu, G. Farrell, Y. Semenova and Q. Wu, "Highly sensitive twist sensor based on partial silver coated hollow core fiber structure", *Journal of Lightwave Technology*, vol. 36, pp. 3672-3677, 2018.

for intensity modulation based fiber sensors. Moreover, the proposed sensor offers excellent measurement repeatability.

Index Terms—*Optical fiber sensors, optical interferometry, optical fiber applications, optical polarization, silver.*

4.2.1 Introduction

Structural health monitoring and shape sensing have been widely studied and employed in numerous applications, including monitoring of bridges, buildings, tunnels, dams and pipelines, for the purpose of warning about the impending abnormal conditions or accidents at an early stage to avoid casualties and to provide maintenance and repair advice [203-204]. Twist/torsion is one of the key parameters that frequently needs to be considered in structural health monitoring. Compared with traditional electromagnetic and electronic sensors, optical fiber based twist/ torsion sensors have attracted significant attention due to their unique advantages such as miniature size, immunity to electromagnetic interference and remote sensing capabilities.

To date, a number of optical fiber based twist sensors have been reported. In general, those sensors can be mainly categorized into the following types, depending on the sensing fiber structure used: fiber gratings [205-210], polarization maintaining fibers (PMFs) [211-214], photonic crystal fibers (PCFs) [215-219] and customized and specially designed fiber based sensors [220-222]. However, fiber grating based twist sensors suffer from relatively low twist sensitivity, most importantly, the fabrication process for such gratings is complex and expensive since it normally requires using an Excimer laser and phase masks. PCF and PMF based twist sensors are reported with much higher twist sensitivity

by combining them with Sagnac interferometers, but those sensors need relatively complex signal interrogation systems, which might limit their potential applications. The customized fiber based sensors have the disadvantages of high cost and requiring complex and expensive fabrication setups.

Hollow core fiber (HCF) has been widely reported for use in optical fiber sensing applications. For example, a Fabry-Perot interferometer (FPI) based sensor was fabricated by incorporating a micro sized air-gap in the HCF to measure a range of environmental parameters, such as temperature and thermo-optic coefficients [223-225]. Most recently, a HCF based interferometer with high quality factor transmission spectrum has been reported [226]; functionalized HCF structures have been demonstrated for humidity sensing, magnetic field monitoring and bio-sensing [227-229]. In this paper, we report a novel high sensitivity twist sensor based on a commercial HCF structure utilizing an interferometric approach, enhanced by the addition of a thin coating layer of silver on one side of the HCF. A maximum twist sensitivity of $0.717 \text{ dB}/^\circ$ has been experimentally demonstrated.

4.2.2 Theoretical model and analysis

Fig. 48(a) illustrates a schematic diagram of the proposed SMF-HCF-SMF fiber structure with partial silver coating at the outer cladding of HCF. The light interference and transmission are illustrated only for the top half of the structure for the sake of clarity. Fig. 48(b) shows a scanning electron microscope (SEM) image of the HCF used and Fig. 48(c) shows a schematic diagram of the HCF cross-section after its partial silver coating (one sided coating). Since the refractive index (RI) of the air core (assuming air has a RI of 1) is smaller than

that of the HCF silica cladding, the optical mode is leaky during its propagation along the HCF. The light incident from the input SMF will be reflected at the interfaces between air core/cladding and cladding/silver/outer air. Multiple reflections take place and there are thus multiple beam interferences within the air core of the HCF, until the propagating beams enter the output SMF.

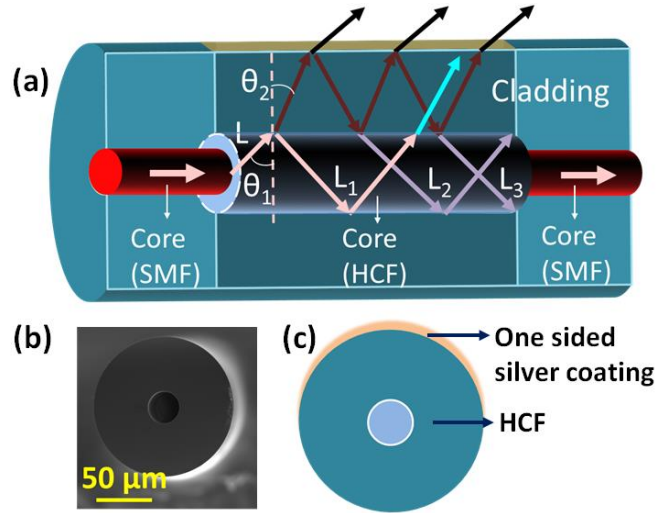


Figure 48. (a) A schematic diagram of the proposed SMF-HCF-SMF fiber structure, showing the multiple beams interference inside the hollow core; (b) an SEM image of the used HCF at the cross-section; and (c) a schematic diagram of the HCF cross-section after coating with silver layer.

Let us assume A is the amplitude of the incident light ray (L), θ_1 and θ_2 are the incident and refracted angles at the interface between the air core and cladding. If the HCF has a cladding thickness d and RI n , then the phase difference between the two adjacent reflected light rays inside the air core of the HCF ($L_1, L_2, L_3 \dots$) can be calculated by

$$\delta = \frac{4\pi}{\lambda} n d \cos \theta_2 \quad (4.10)$$

The amplitudes of the reflected light $L_1, L_2, L_3 \dots L_j \dots$ can be described as:

$$r_1 A, r_2 \rho^2 A e^{i\delta}, r_2 (-r_1 r_2) \rho^2 A e^{i2\delta} \dots, r_2 (-r_1 r_2)^{m-1} \rho^2 A e^{im\delta}, \dots \quad (4.11)$$

where r_1 and r_2 are the reflection coefficients at the interface between the inner air/cladding and cladding/silver/outer air respectively, ρ represents refraction coefficient at the interface between the inner air and fiber cladding, and m is a positive integer. Then the final amplitude of the light propagating in the hollow core can be determined by summing all the reflected amplitudes as follows:

$$\begin{aligned} A_r &= r_1 A + r_2 \rho^2 A e^{i\delta} + r_2 (-r_1 r_2) \rho^2 A e^{i2\delta} + \dots + r_2 (-r_1 r_2)^{m-1} \rho^2 A e^{im\delta} + \dots \\ &= \frac{r_1 + r_2 e^{i\delta}}{1 + r_1 r_2 e^{i\delta}} A \end{aligned} \quad (4.12)$$

The light intensity transmitted in the hollow core is hence given as

$$I_r = |A_r|^2 \quad (4.13)$$

As can be seen from the above equations, the transmitted light intensity only depends on the incident light amplitude and on the refraction and reflection coefficients at the interfaces between the air core /cladding and cladding/silver/outer air. It is noted that for the lower half of the HCF structure the transmitted light intensity could be also calculated using above equations but with a different value of r_2 . Fig. 49 shows a family of simulated spectral responses of the structure for varying reflection coefficients r_2 while assuming r_1 constant. In the simulation, the diameters of the air core and cladding are 30 μm and 126 μm respectively. The incident angle θ_i is 80.8°. The incidence angle is chosen for a typical single mode fiber with NA=0.16, where $r_1 = -0.74$. The

refractive indices of the air and silica cladding are 1 and 1.444 respectively. As shown in Fig. 49, as r_2 deviates from r_1 further, the dip's strength decreases significantly.

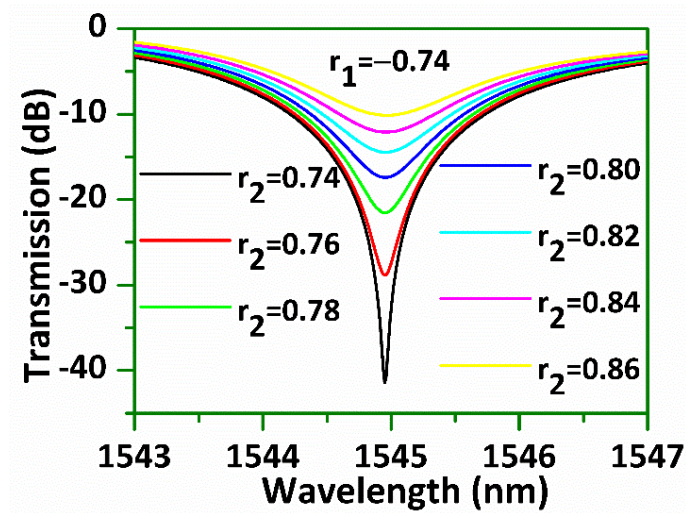


Figure 49. Simulated spectral responses of the HCF structure with a constant reflection coefficient r_1 and varying reflection coefficient r_2 .

4.2.3 Results and discussion

Here we report on the results of the experimental investigation of the influence of twist on the transmission spectrum of the partially silver-coated HCF structure. Firstly, a short section of a HCF (inner air core diameter $\sim 30 \mu\text{m}$, outer cladding diameter $\sim 126 \mu\text{m}$) with a length of 4.5 mm was fusion spliced between two SMFs. A length of 4.5 mm was chosen based on the previous experience, which demonstrated that this particular HCF length resulted in a relatively high Q factor and low loss. The splicing power and the gaps between the SMFs and HCF were carefully chosen to avoid the collapse of the hollow core during fusion splicing. In our experiment, a Fujikura 70S splicer was used, and its arc power was set to be STD-85 bit, arc time was 0.4 s and the arc gap was $13 \mu\text{m}$. Once the fiber structure was fabricated, a thin layer of silver was coated on one side of

the HCF surface using a sputter-coating machine (Quorum Technologies Q150RS). For our experiments 6 fiber structure samples were fabricated with different coating thicknesses. During the coating process, the HCF fiber was placed horizontally in the sputtering chamber and coated for a fixed period of time. Since the fiber is fixed within the chamber, only one side of the HCF is coated with silver. It is noted that the coating thickness is unevenly distributed over the surface, with the maximum thickness at the top of the cylinder's cross-section, decreasing towards both sides (Fig. 48(c)).

Because silica is not a conductor and only a very thin layer (around 10 nm) of silver is coated on the HCF fiber surface, it is difficult to measure the actual thickness of the silver coating unless using a high resolution SEM. Therefore in our experiment the coating thickness is a calibrated value on a glass slide calculated as $6.7 \text{ nm/minute} \times \text{Time}$ as shown in Fig. 50.

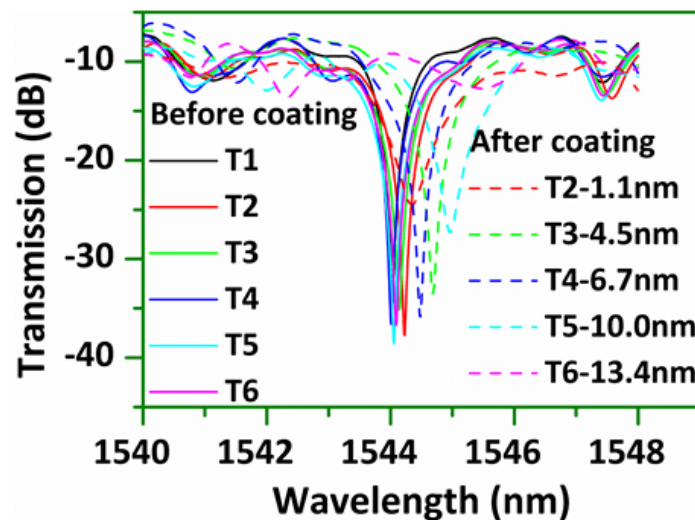


Figure 50. Measured spectral responses of the HCF based fiber structures before and after deposition of the silver coating.

Fig. 50 illustrates the influence of the silver coating thickness on the sensor's spectral response, where the largest transmission dips for all the six samples (T1 to T6) are shown before and after application of the silver coating by adjusting

the polarization state of the input light using a manual polarization controller (PC, DPC5000). As one can see from the figure, for the fiber samples without the silver coating, spectral responses have similar transmission dips with a maximum variation between the central dip wavelengths of 0.22 nm and dip strength variation of 4.4 dB, which proves the HCF based fiber structure shows good reproducibility. The observed minor variations in the transmission spectra can be attributed to minor differences in each fiber fusion splice conditions, due to minor splice power variations, and by different degrees of flatness and cleanness of the fiber ends after cleaving and fiber alignment during the fiber fusion splicing process. With the increase of the coating time from 10 to 120 s (equivalent to a coating thickness increase from 1.1 to 13.4 nm), the transmission dips gradually move toward longer wavelengths. The largest two wavelength dips after coating are observed when the coating times are 40 s (T3) and 60 s (T4), where the coating thickness is calculated to be 4.5 and 6.7 nm, respectively.

The uncoated and partially silver-coated HCF fiber structures were then placed within the experimental setup shown in Fig. 51. In our experiment, we investigated the effect of twist separately for the SMF section only (Section 1 in the figure) and also for a section containing the HCF (Section 2). To realize this, twisting of the fiber structure was carried out using two fiber rotators with the fiber firmly held in place at two points by fiber holders, marked as H1 and H2 in Fig. 51. Rotator 1 was used for twisting the SMF section (Section 1) only and rotator 2 was used for twisting the fiber structure section including the whole length of the HCF (Section 2). Both Section 1 and Section 2 have the same length of 20 centimeters, and the twist angle resolution of the rotators is about one degree. Before the fiber was fixed onto the stages, a weight of 14.6 g was

used between rotator 2 and a third fiber holder (H3), to keep the fiber straight and to ensure that a fixed strain has been applied to the fiber structure during the twist experiment. Light from a broadband light source (BBS) was launched into the HCF based structure and the transmitted light was measured by an optical spectrum analyzer (OSA). A PC (DPC5500) was used to achieve linear polarized light and to adjust the polarization state of the light before it enters the twisted fiber sections.

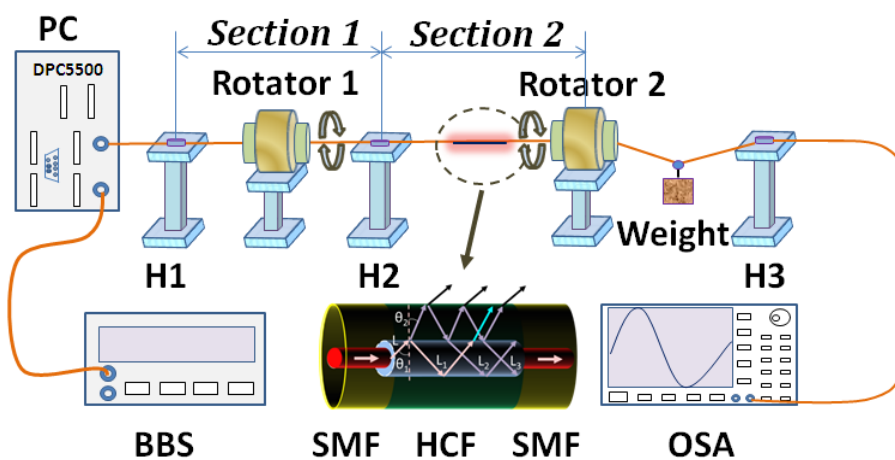


Figure 51. Schematic diagram of the twist sensing setup.

Before we performed the twist experiment, the influence of the input light polarization state (controlled by the DPC 5500) on the transmission spectral response of the partially silver coated sample (40 s coating) was investigated and the result is shown in Fig. 52 (a). As one can see from the figure, the spectral dip strength is highly dependent on the polarization state of the input light. This effect could be understood as follows. Light polarization could be described as the vector sum of S-polarized and P-polarized light components. For an uncoated HCF based fiber structure, the reflection coefficients r_1 and r_2 inside the HCF for non-normal incidence are given by the Fresnel equations (assuming air has a RI of 1):

$$r_{1s} = \frac{\cos\theta_1 - n\cos\theta_2}{\cos\theta_1 + n\cos\theta_2}, r_{2s} = -r_{1s} \quad (4.14)$$

$$r_{1p} = \frac{n\cos\theta_1 - \cos\theta_2}{n\cos\theta_1 + \cos\theta_2}, r_{2p} = -r_{1p} \quad (4.15)$$

where n is the RI of the cladding, θ_1 and θ_2 are the incident and refracted angles at the interface between the air core and cladding. According to equations (4.14) and (4.15), the reflection coefficient is dependent on the RI of the medium and on the angle of incidence. At normal incidence, light polarization state has no influence on the reflection coefficient. When the angle of incidence is different from normal and less than critical angle, the S-polarized light is always more strongly reflected than P-polarized light [230]. When the input linearly polarized (LP) light polarization state changes, its components in P and S directions change accordingly resulting in a variation of the reflection coefficients. For an ideal uncoated HCF, due to its circular symmetry, the polarization state of the input light has no influence on the reflection coefficient. However, a partial coating of silver on the outer surface of the HCF cladding significantly increases the polarization dependence of the reflection coefficient at the outer HCF surface because the one-side coating introduces an asymmetric RI distribution over the outer surface of the HCF (Fig. 52(b)), leading to a large variation on the reflection coefficient of r_2 , and consequently to large power variations as illustrated in Fig. 49. Besides, due to the actual uneven coating in all the directions, anisotropic properties and thus introduced birefringence could also introduce the change of the reflection coefficients at the cladding/silver interface. Let's assume now that a twist is applied to the partially silver coated HCF sensor. When LP light is launched into a circularly symmetric fibre, the light polarization state is maintained with almost no changes throughout the entire length of all

fiber sections [231], but, due to the uneven silver coating on the HCF surface and hence the asymmetric RI distribution over the outer surface of the HCF, the P and S polarization components and their corresponding reflection coefficients of r_2 change due to the twist as shown in Fig. 52(c). Hence, the spectral dip strength varies with different twist angles. The experimental demonstration is shown below.

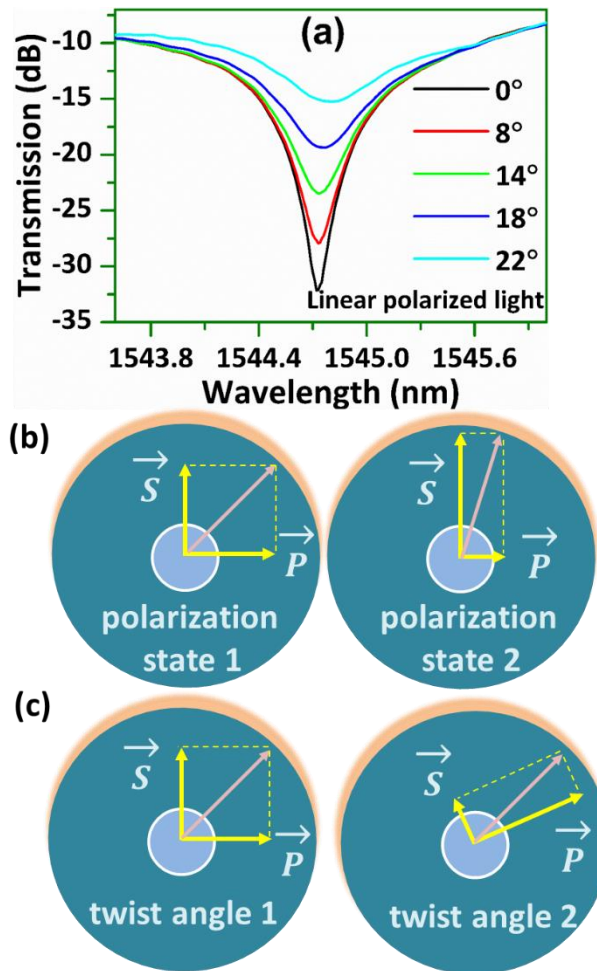


Figure 52. (a) Measured transmission spectral responses of the partially silver coated sample (40 s coating) for different input polarization states (angle of linearly polarized light changes from 0° to 22°), and a schematic diagram shows the E-field orientation (b) at different LP state, and (c) at different twist angles.

The effect of twist on the HCF sensor without the silver coating (T1) was firstly investigated and the experimental results are presented in Fig. 53. Before

applying the twist, the polarization state of the input light was adjusted using the PC to achieve the largest dip strength. This initial spectrum with the largest dip strength was then labelled as a 0° twist angle state. In our experiment, we define a clockwise twist as a positive twist angle while the counter clockwise twist as the negative twist angle. Fig. 53 shows the measured spectral dip strength variations under different twist angles. The maximum dip strength change is 2.18 dB in the case of twisting the HCF section (rotator 2), which is over 4 times higher than that of 0.51 dB for the case of twisting the SMF (rotator 1). This result indicates that twisting the HCF section achieves a higher sensitivity than that for the SMF alone. Ideally for a circularly symmetric fiber geometry, no spectral dip strength changes with twist would be expected, but this could change due to residual stress and core ellipticity, resulting from the practical fiber fabrication process. Especially for the HCF, any twist- induced stress could easily result in the RI change at the interface of inner air/cladding. Besides, the actual slight differences between the applied differential twists per unit length for section 1 and section 2 could also contribute to the observed difference in the twist sensitivities. It is noted that the fiber section containing HCF was fixed at 0° twist angle while twisting of the SMF was performed, and vice versa.

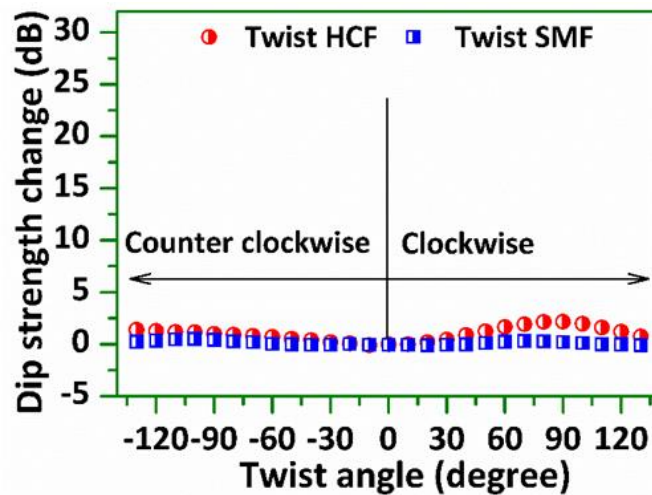


Figure 53. Measured spectral dip strength variations for a range of twist angles by twisting SMF only and HCF only – uncoated HCF sensor (T1).

Next, the effect of twist on a partially silver coated HCF sensor was investigated. Samples T3 and T4 were selected for this experiment due to their relatively large dip strength.

Fig. 54 shows the corresponding experimental results for samples T3 and T4. An example of changes in the transmission dip strength for T3 at different twist angles is shown in Fig. 54(a). At 0° of twist angle, the spectral dip has a high quality factor (Q) of 1.8×10^4 and a large extinction ratio (over 26 dB). As the twist angle (in both clockwise and counter-clockwise directions) increases, the transmission dip strength decreases monotonically. Fig. 54(b) summarizes the changes of the spectral dip strength as the twist angle varies from -90° to 90°. It can be seen from the figure that the sensor has much higher sensitivity to twist in the small twist angles range. Comparing with the uncoated HCF sensor (T1), it was found that T3 has significantly improved sensitivities both when twisting the HCF and when twisting the SMF sections alone. The maximum sensitivity when twisting the SMF is 0.21 dB/° which is over 10 times higher than that of the uncoated HCF sensor. When the HCF section was twisted, a maximum

sensitivity of $0.647 \text{ dB}/^\circ$ was achieved, which is over 17 times higher than that of the HCF sensor without the silver coating.

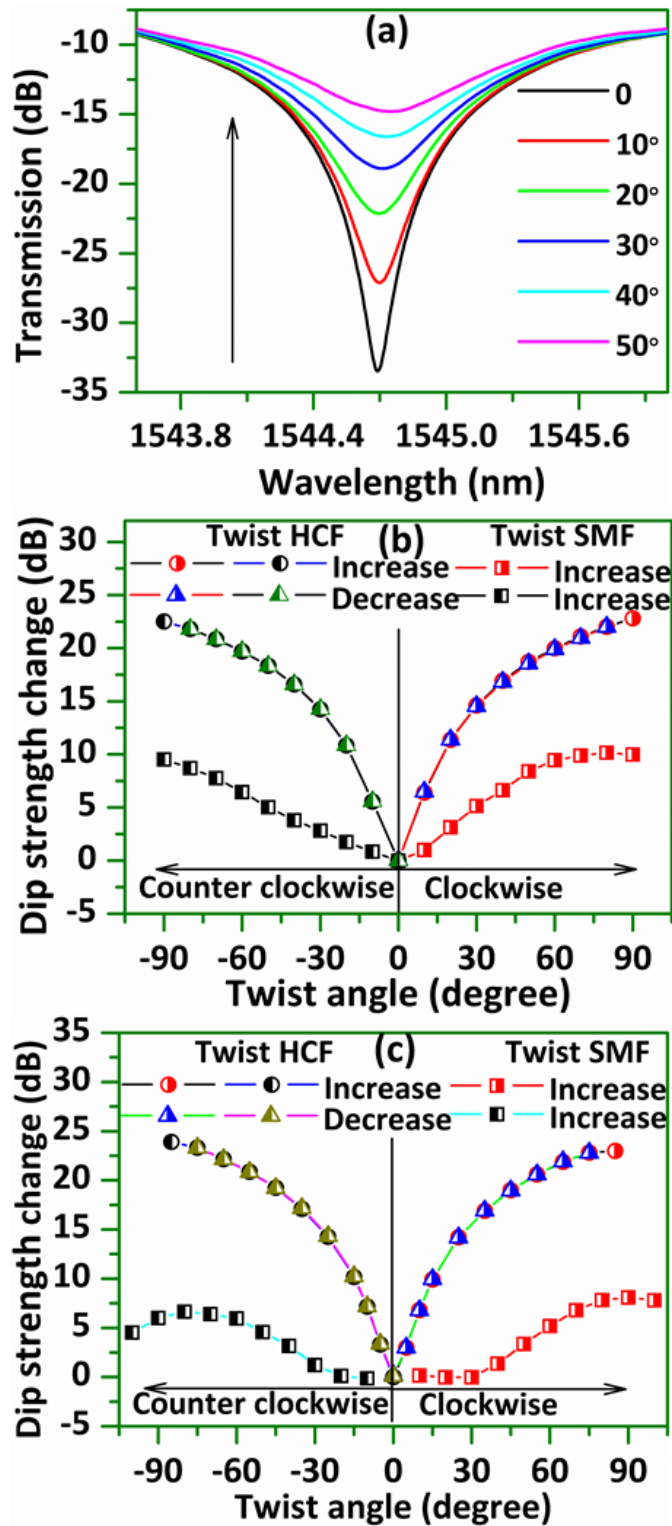


Figure 54. (a) An example of the measured spectral response of T3 when twisting HCF; (b) measured dip strength change of T3 and (c) T4 for a range of twist angles when twisting SMF only and HCF only – partially silver coated HCF sensor.

The above experimental results can be explained as follows: since the reflection coefficient at the outer HCF surface after partial silver coating is polarization dependent, twisting of HCF will introduce significant change in the relative amplitude of the transmitted light in the air core due to the changed reflection coefficient, which results in the variations of the output light intensity as shown in Fig. 49 and Fig. 52. In addition, the sensor also demonstrates good repeatability of its response with no evidence of hysteresis since the measured data for the twist angle increasing cycle matches very well the data for the twist decreasing cycle. The twist performance of T4 was also tested and the results are plotted in Fig. 54(c), which shows similar to the T3 spectral changes but with slightly improved twist sensitivity. The maximum twist sensitivity is up to 0.717 dB/° in the range of twist angles from 0° to 10°.

As can be seen from Fig. 54(b), the dip strength decreases when the fiber is twisted in both clockwise and counter clockwise directions. Hence, a first order derivative of the dip strength change is employed to identify the twist direction as shown in Fig. 55(a), a positive derivative corresponds to a clockwise twist while a negative derivative indicates a counter clockwise twist. By using both dip strength variation and the first order derivative data, both the twist angle and twist direction can be clearly identified.

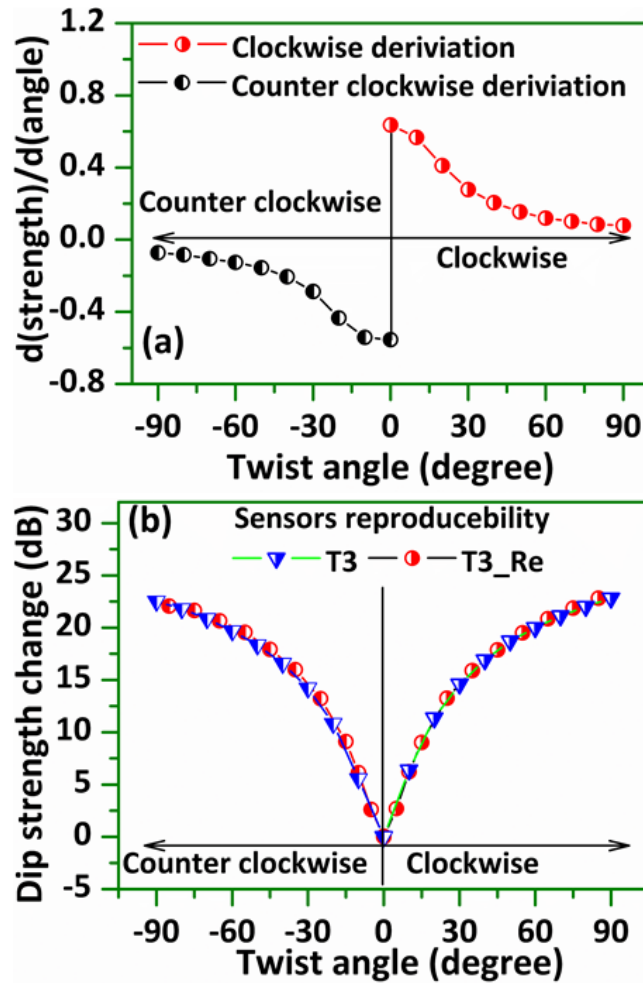


Figure 55. (a) First order derivative of the measured spectral dip strength change with the twist angle when twisting HCF and (b) sensor's reproducibility demonstration with different samples when twisting the HCF.

It is noted that since the operating principle of our sensor is based on the spectral dip strength modulation, the reproducibility of the sensor is mainly dependent on the coating thickness and the bare HCF structure's spectral dip strength. In reality, there would always be some variations in the twist sensitivities for different sensor samples due to the variation in coating thickness and dip strength. It is also noted that the higher the sensitivity of the fiber structure, the less reproducible it is in practice. In our experiment, by choosing two bare HCF structure samples with similar spectral dip strengths and coating them with silver for the same time period of 40 s, two sensor samples with very

similar responses to twist were successfully prepared as shown in Fig. 55(b).

4.2.4 Conclusion

In summary, a novel high sensitivity twist sensor is proposed and investigated by partially coating a thin layer of silver film on the surface of a short section of HCF. Samples with different coating thicknesses have been studied. The experimental results demonstrate that the samples with 4.5 nm (40 s coating) and 6.7 nm (60 s coating) silver coating thickness have the highest sensitivity of 0.647 dB/° and 0.717 dB/° in the range of twist angles from 0° to 10°, respectively. Moreover, twist of the HCF section has higher sensitivity than that of the SMF section for sensors both with and without the silver coating. Experiments proved that the proposed sensor also shows good repeatability of twist response.

4.2.5 Reference

- [203] G. W. Housner, L. A. Bergman, T. K. Caughey, A. G. Chassiakos, R. O. Claus, S. F. Masri *et al.*, “Structural control: past, present, and future,” *J. Eng. Mech.*, vol. 123, no. September, pp. 897–971, 1997.
- [204] H. N. Li, D. S. Li, and G. B. Song, “Recent applications of fiber optic sensors to health monitoring in civil engineering,” *Eng. Struct.*, vol. 26, no. 11, pp. 1647–1657, 2004.
- [205] Y. P. Wang and Y. J. Rao, “Long period fibre grating torsion sensor measuring twist rate and determining twist direction simultaneously,” *Electron. Lett.*, vol. 40, no. 3, pp. 164–166, 2004.
- [206] Y. J. Rao, T. Zhu, and Q. J. Mo, “Highly sensitive fiber-optic torsion sensor based on an ultra-long-period fiber grating,” *Opt. Commun.*, vol. 266, no. 1, pp. 187–190, 2006.
- [207] Y. Wang, M. Wang, and X. Huang, “In fiber Bragg grating twist sensor based on analysis of polarization dependent loss,” *Opt. Express*, vol. 21, no. 10, pp. 11913–11920, 2013.

- [208] J. H. Wo, M. Jiang, M. Malnou, Q. Sun, J. Zhang, P. P. Shum, and D. Liu, "Twist sensor based on axial strain insensitive distributed Bragg reflector fiber laser," *Opt. Express*, vol. 20, no. 3, pp. 2844–2850, 2012.
- [209] L. Shi, T. Zhu, Y. E. Fan, K. S. Chiang, and Y. Rao, "Torsion sensing with a fiber ring laser incorporating a pair of rotary long-period fiber gratings," *Opt. Commun.*, vol. 284, no. 22, pp. 5299–5302, 2011.
- [210] X. Chen, K. Zhou, L. Zhang, and I. Bennion, "In-fiber twist sensor based on a fiber Bragg grating with 81° tilted structure," *IEEE Photonics Technol. Lett.*, vol. 18, no. 24, pp. 2596–2598, 2006.
- [211] R. M. Silva, M. S. Ferreira, and O. Frazão, "Temperature independent torsion sensor using a high-birefringent Sagnac loop interferometer," *Opt. Commun.*, vol. 285, no. 6, pp. 1167–1170, 2012.
- [212] D. Lesnik and D. Donlagic, "In-line, fiber-optic polarimetric twist/torsion sensor," *Opt. Lett.*, vol. 38, no. 9, pp. 1494–1496, 2013.
- [213] B. Huang, X. Shu, and Y. Du, "Intensity modulated torsion sensor based on optical fiber reflective Lyot filter," *Opt. Express*, vol. 25, no. 5, pp. 5081–5090, 2017.
- [214] T. Guo, F. Liu, F. Du, Z. Zhang, C. Li, B. O. Guan, and J. Albert, "VCSEL-powered and polarization-maintaining fiber-optic grating vector rotation sensor," *Opt. Express*, vol. 21, no. 16, pp. 19097–19102, 2013.
- [215] H. M. Kim, T. H. Kim, B. Kim, and Y. Chung, "Temperature-insensitive torsion sensor with enhanced sensitivity by use of a highly birefringent photonic crystal fiber," *IEEE Photonics Technol. Lett.*, vol. 22, no. 20, pp. 1539–1541, 2010.
- [216] T. Hu, Y. Zhao, and D. Wu, "Novel torsion sensor using a polarization maintaining photonic crystal fiber loop mirror," *Instrum. Sci. Technol.*, vol. 44, no. 1, pp. 46–53, 2016.
- [217] P. Zu, C. C. Chan, Y. X. Jin, T. X. Gong, Y. F. Zhang, L. H. Chen, and X. Y. Dong,, "A temperature-insensitive twist sensor by using low-birefringence photonic-crystal-fiber-based Sagnac interferometer," *IEEE Photonics Technol. Lett.*, vol. 23, no. 13, pp. 920–922, 2011.
- [218] O. Frazao, C. Jesus, J. M. Baptista, J. L. Santos, and P. Roy, "Fiber-optic interferometric torsion sensor based on a two-LP-mode operation in birefringent fiber," *IEEE Photonics Technol. Lett.*, vol. 21, no. 17, pp.

1277–1279, 2009.

- [219] W. Chen, S. Lou, L. Wang, H. Zou, W. Lu, and S. Jian, “Highly sensitive torsion sensor based on Sagnac interferometer using side-leakage photonic crystal fiber,” *IEEE Photonics Technol. Lett.*, vol. 23, no. 21, pp. 1639–1641, 2011.
- [220] B. Song, Y. Miao, W. Lin, H. Zhang, J. Wu, and B. Liu, “Multi-mode interferometer-based twist sensor with low temperature sensitivity employing square coreless fibers,” *Opt. Express*, vol. 21, no. 22, pp. 26806–26811, 2013.
- [221] D. Yu, Q. Mo, Z. Hong, S. Fu, C. Sima, M. Tang, and D. Liu, “Temperature-insensitive fiber twist sensor based on elliptical-core few-mode fiber,” *Opt. Lett.*, vol. 41, no. 20, pp. 4617–4620, 2016.
- [222] O. Frazão, R. M. Silva, J. Kobelke, and K. Schuster, “Temperature- and strain-independent torsion sensor using a fiber loop mirror based on suspended twin-core fiber,” *Opt. Lett.*, vol. 35, no. 16, pp. 2777–2779, 2010.
- [223] C.-L. Lee, L.-H. Lee, H.-E. Hwang, and J.-M. Hsu, “Highly Sensitive Air-Gap Fiber Fabry–Pérot Interferometers Based on Polymer-Filled Hollow Core Fibers,” *IEEE Photonics Technol. Lett.*, vol. 24, no. 2, pp. 149–151, 2012.
- [224] C.-L. Lee, H.-Y. Ho, J.-H. Gu, T.-Y. Yeh, and C.-H. Tseng, “Dual hollow core fiber-based Fabry–Pérot interferometer for measuring the thermo-optic coefficients of liquids,” *Opt. Lett.*, vol. 40, no. 4, pp. 459–462, 2015.
- [225] M. S. Ferreira, L. Coelho, K. Schuster, J. Kobelke, J. L. Santos, and O. Frazão, “Fabry-Perot cavity based on a diaphragm-free hollow-core silica tube,” *Opt. Lett.*, vol. 36, no. 20, pp. 4029–4031, 2011.
- [226] D. Liu, Q. Wu, C. Mei, J. Yuan *et al.*, “Hollow Core Fiber Based Interferometer for High Temperature (1000 °C) Measurement,” *J. Light. Technol.*, vol. 36, pp. 1583–1590, 2018.
- [227] R. Gao, D. F. Lu, J. Cheng, Y. Jiang, L. Jiang, and Z. M. Qi, “Humidity sensor based on power leakage at resonance wavelengths of a hollow core fiber coated with reduced graphene oxide,” *Sensors Actuators, B Chem.*, vol. 222, pp. 618–624, 2016.

- [228] R. Gao, Y. Jiang, and Y. Zhao, "Magnetic field sensor based on anti-resonant reflecting guidance in the magnetic gel-coated hollow core fiber," *Opt. Lett.*, vol. 39, no. 21, pp. 6293–6296, 2014.
- [229] A. M. Zheltikov, "Ray-optic analysis of the (bio)sensing ability of ring-cladding hollow waveguides," *Appl. Opt.*, vol. 47, no. 3, pp. 474–479, 2008.
- [230] C. A. Dimarzio, *Optics for engineers*, CRC Press, 2011.
- [231] A. M. Smith, "Birefringence induced by bends and twists in single-mode optical fiber," *Appl. Opt.*, vol. 19, pp. 2606–2611, 1980.

Chapter 5

Conclusions and future work

This chapter reviews the conclusions from across the thesis, and discusses the key contributions to current technology and knowledge. Possible future research work as an extension of this PhD thesis is also discussed.

5.1. Conclusions from the research

The primary aim of this research, as stated in Chapter 1, is to

Develop ultra-high sensitivity and high detection accuracy optical fiber sensors for a variety of measurands, utilizing SMS or modified SMS structures, combined with fiber surface modification techniques.

This aim has been achieved, as evidenced by the developments presented in the previous chapters, specifically:

I. A traditional SMS fiber structure for breath monitoring.

In this thesis, one of the objectives is to explore the healthcare applications of fiber sensors based on a traditional SMS structure. This was achieved by the development of a novel breath sensor using a simple SMS fiber structure. The conclusions from this research are as follows:

- The SMS based breath sensor is capable of monitoring human patients' breathing state and breath rate in real time.
- The SMS based breath sensor can easily distinguish between different types of breathing conditions including a regular/irregular breathing pattern and an urgent/slow breathing pattern.

- The SMS based breath sensor can be used in strong electromagnetic fields and radioactive environments such as those experienced during MRI and CT examinations where traditional electronic sensors could not be applied.
- The SMS based breath sensor also offers the advantages of easy fabrication, low cost, fast response and potentially good resistance to environmental contamination.

II. Tapered SCSMF for RI, ammonia, and VOCs detection.

Another important objective is to increase the sensitivity of the traditional SMS fiber structure to the surrounding RI, in order to satisfy the demands of biochemical and environmental sensing applications. This was realized by novel fiber tapering techniques and by utilizing special types of fibers as follows:

Novel SCSMF based RI sensor

- The experimentally demonstrated highest RI sensitivity for the tapered SCSMF based sensor structure is up to 19212.5 nm/RIU in the RI range from 1.4304 to 1.4320, corresponding to a theoretical resolution of 5.025×10^{-7} RIU, which is over 10 times higher than that for the untapered sensor structure [232].
- A linear wavelength shift response vs. RI changes is observed for the SCSMF based sensor structure within the measurement RI range.
- Most of optical fiber based RH sensors require coating of a layer of hygroscopic material on the fiber surface of the sensor structure. However, using a coating material suffers from the disadvantages of a complicated fabrication process and limited life time, due to coating contamination or degradation. In this work, it is concluded that a tapered SCSMF structure can be operated as an RH sensor even without any coatings. A maximum

sensitivity of 18.3 nm per relative humidity unit (RHU) was achieved in the RH range from 90.4% to 94.5% RH.

Novel SCSMF based ammonia sensor

- For the first time, it is shown that sol-gel silica can be used as an ammonia sensitive coating layer, functionalized on the surface of a tapered SCSMF structure. The sensor's performance for ammonia detection is analyzed and reported.
- A maximum ammonia sensitivity of 2.47 nm/ppm has been achieved, corresponding to an ammonia concentration detection limit of 4 ppb in water, which represents a better than three order of magnitude improvement compared to fiber sensors with the same operating principle. In addition it has been demonstrated, that an increase in the sol-gel silica coating layer thickness leads to a higher ammonia sensitivity.
- The proposed sensor demonstrates fast response and recovery times of less than 2 and 5 minutes respectively. In addition, good repeatability and good selectivity to ammonia amongst a range of common ions in water and some organic molecules have been demonstrated.

Novel SCSMF and MFC based VOCs sensor

- A tapered SCSMF and an MFC have been selected as the core fiber structures for realizing highly sensitive VOCs sensors. These fiber structures were functionalized with a silica sol-gel/Nile Red coating layers. The effectiveness of the coating materials for sensing of ethanol and methanol has been demonstrated experimentally.
- The MFC based sensor shows better sensitivities of 0.130 nm/ppm and 0.036 nm/ppm to ethanol and methanol compared to those of the tapered

SCSMF based sensor. The corresponding minimum detectable ethanol and methanol concentration changes for the MFC based sensor are estimated as ~77 ppb and ~281 ppb respectively.

- Both tapered SCSMF and MFC based sensors have fast response times of less than 5 minutes, while the recovery times varied from 7 minutes to 12 minutes.
- Simultaneous measurement of ethanol and methanol concentrations has been demonstrated based on the response matrix involving two tapered SCSMF samples coated with different coating recipes (different stirring time for the preparation of the sol-gel silica).

III. HCF structure for high temperature and twist sensing.

The relatively low spectral Q factor of traditional SMS-based fiber sensors limits their measurement accuracy. In this thesis, a modified SMS structure based on a HCF is demonstrated with a spectrum providing a Q factor approximately two orders of magnitude higher than those for a tapered SCSMF or traditional SMS structure. A large spectral extinction ratio has also been demonstrated. Applications for high temperature and twist angle measurements are investigated.

The conclusions from this research are as follows:

HCF based temperature sensor

- The transmission spectrum of the proposed HCF based fiber structure contains a series of periodic transmission dips with large spectral extinction ratio (~26 dB), large FSR (~23 nm) and high Q factor ($\sim 3.3 \times 10^4$).

- A theoretical model is proposed, which attributes the formation of periodic transmission dips to multiple beams interferences introduced by the silica cladding of the HCF.
- Compared to an FBG based temperature sensor, the sensor based on HCF shows a higher temperature sensitivity (up to 33.4 pm/°C) and wider operating temperature range (from room temperature to 1000°C).
- It is concluded that the proposed sensor provides high measurement resolution, good stability, repeatability, relatively low strain sensitivity (0.46 pm/με), potentially low cost and a simple and flexible fabrication process that offers significant potential for practical applications.

HCF based twist sensor

- A partial silver coating is successfully introduced to the outer surface of the HCF for the first time for the detection of twist angle change.
- The silver coating thickness is found to have significant influence on the strength of transmission spectral dips. The maximum dip strength appears when the coating thickness is 4.5 and 6.7 nm.
- It is found that the transmission spectrum of a partially silver-coated HCF structure is very sensitive to changes in the polarization state of the input light.
- The highest twist sensitivity of 0.717 dB/° has been achieved, as the highest twist sensitivity reported for intensity modulation based sensors.
- The proposed sensor has been proven to offer excellent measurement repeatability.

5.2. Future work

For the future, there remains a number of challenges and research topics that could be extended further beyond the research presented in this thesis.

I. Extend potential applications for a tapered SCSMF structure

In Chapter 3, we have demonstrated that a tapered SCSMF structure is highly sensitive to the surrounding RI, which allowed the use this bare fiber structure for monitoring of high levels of RH. However, the sensitivity of such a bare structure in the low RH range (below a RH of 70%) is very low. To address this problem, an investigation of the functionalization of suitable coating materials (e.g. polyvinyl alcohol, polyimide, poly (methyl methacrylate), etc.) to enhance the RH sensitivity of the tapered SCSMF structure could be carried out as a part of future work.

In Chapter 3, it was also demonstrated that a tapered SCSMF structure can be used in high sensitivity chemical sensors for detection of the concentration of ammonia and VOCs. As a next step, bio-sensing applications of the tapered SCSMF structure could be investigated. It is known that antibody-antigen binding can alter local RI [233], thus for example, by immobilizing fibrinogen on the surface of a tapered SCSMF structure, the concentration of anti-fibrinogen could be detected.

II. Extend potential applications for the HCF based fiber structure

HCF based fiber structure offers a high Q factor and large extinction ratio. Compared to conventional fiber filters, such as a fiber Bragg grating and tapered fiber structures, it has the advantages of a simple configuration, ease of fabrication, low cost, with comparable (or even better) Q factor. To date, there has been lack of in-depth investigations of a HCF based fiber structure and its

potential applications. There is thus the necessity to carry out further research on the modification and functionalization of a HCF based structure, for example, by functionalizing its surface with different coating materials on the inner/outer surface of the HCF. The structure can also be employed in many different sensing applications such as bio-chemical sensing and medical diagnostics. Such future research could provide new directions for the development of novel cost effective, high performance photonics components, which will be beneficial to the wider research community in the fields of optical fiber communication components and sensors.

III. New coating materials

Coating materials are essential in the field of optical fiber based bio-chemical sensing. In Chapter 3, it has been demonstrated that sol-gel silica shows high sensitivity and good selectivity to ammonia gas compared to other VOCs, but with appropriate design of the fabrication process, the texture and surface chemistry properties of the sol-gel prepared silica, sol-gel silica based coatings sensitive to VOCs can be developed, which has been demonstrated by Echeverría *et al.* [234]. Utilizing such modified sol-gel silica materials combined with the developed fiber sensors, will mean that more sensitive sensors for various VOCs could be achieved. Meanwhile, simultaneous measurement of multiple VOCs can be realized due to the use of different property based coating materials. In addition, novel nanomaterials with a different morphology could be investigated as functional coatings since they can offer an increased ratio of exposed surface area to volume, which in turn has dramatic effects on sensor's performance.

IV. New modified SMS structure based on PCF and MCF

PCF offers a number of advantages in fiber design [235]. By properly selecting

the diameter of the core and the cladding holes, and the distance between the cladding holes (namely the pitch Λ), the fiber transmission spectrum, mode shape, nonlinearity, dispersion and birefringence can be tuned. The presence of hollow core and cladding holes makes PCF an excellent candidate for sensing applications by filling air holes with chemical/biochemical liquids or gases by using micropumps or syringes.

Similar to PCF, Multi Core Fibers (MCF) are also promising types of fibers for sensing applications [236]. In a MCF, the desired supermodes can be achieved by varying the design of the number of cores, distance between the cores, diameter of the cores, the pitch of the cores, and index profiles of the cores. Assuming only LP₀₁ mode is designed to be supported in each core, the resulting supermodes interference inside the MCF is stable and predictable. In addition, the cores and the corresponding supermodes of the MCF can be mode matched to SMF, which could significantly decrease the coupling loss between MCF and SMF. What is more, by combining with tapering technique, much stronger supermodes interference could be introduced. Therefore, MCF is an attractive candidate for sensing applications utilizing the SMS design.

5.3. References

- [232] Q. Wu, Y. Semenova, P. Wang, *et al.*, “A comprehensive analysis verified by experiment of a refractometer based on an SMF28-small-core singlemode fiber (SCSMF)-SMF28 fiber structure,” *J. Opt.*, vol. 13, no. 12, pp. 937–946, 2011.
- [233] P. A. O. T. Tagawa, and T. Tamura, *Biomedical sensors and instruments*, Second edition, *CRC Press*, 2011.
- [234] J. C. Echeverría, M. Faustini, and J. J. Garrido, “Effects of the porous

texture and surface chemistry of silica xerogels on the sensitivity of fiber-optic sensors toward VOCs,” *Sensors Actuators, B Chem.*, vol. 222, pp. 1166–1174, 2016.

[235] O. Frazão, J. L. Santos, F. M. Araújo, and L. a Ferreira, “Optical sensing with photonic crystal fibers,” *Laser Photon. Rev.*, vol. 2, no. 6, pp. 449–459, 2008.

[236] A. V. Newkirk, “Sensing using Specialty Optical Fibers,” PhD thesis, 2016.

Appendix A

Statement of Contribution

For the publications presented within this thesis, the co-authors listed below certify that:

1. Dejun Liu is the first author or the equal contribution first author for the first listed six journal publications and the first listed three conference papers in the publication list.
2. As first author for the first listed six journal publications and the first listed three conference papers in the publication list, Dejun Liu undertook all aspects of the research described in each publication, including preparation and submission of the publication and the preparation of any revisions requested by referees, with the support and advice of the co-authors.
3. The co-authors agree to the use of the publications in this thesis.



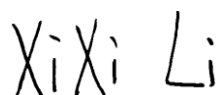
Prof. Gerald Farrell



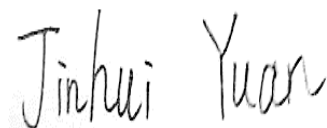
Prof. Yuliya Semenova



Dr. Qiang Wu



Ms. Xixi Li



Prof. Jinhui Yuan



Prof. Chongxiu Yu



Prof. Xiangjun Xin



Prof. Shengpeng Wan

Xingdao He

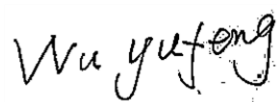
Prof. Xingdao He



Prof. Gang-Ding Peng



Dr. Wai Pang Ng



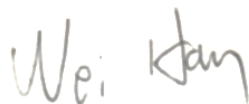
Dr. Yufeng Wu



Dr. Feng Li



Dr. Zhengyong Liu



Mr. Wei Han



Ms Fangfang Wei

Bo Liu

Prof. Bo Liu



Prof. Hwa-Yaw Tam



Dr. Yong-qing Fu



Dr. Guorui Zhou



Dr. Zhe Kang



Mr. Rahul Kumar



Mr. Arun Kumar Mallik



Mr. Chao Mei

Appendix B

Modes theory

Optical fiber has a cylindrical geometry, where a is assumed as the fiber core radius, n_1 and n_2 are the RIs of the fiber core and cladding respectively. The electric field (E_z) and magnetic field (H_z) in the z direction can be derived from the Helmholtz equation in a cylindrical coordinate system (Figure 56) [237]:

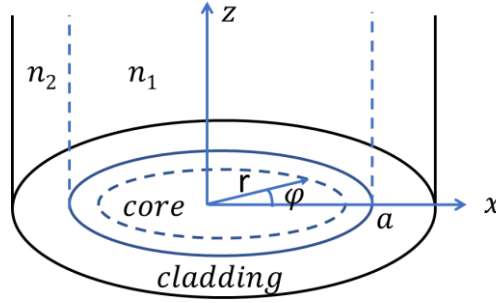


Figure 56. Cylindrical coordinate system in an optical fiber.

$$\begin{cases} E_{z1} = \frac{A}{J_m(U)} J_m(Ur/a) \sin m\varphi e^{-i\beta z} \\ H_{z1} = \frac{B}{J_m(U)} J_m(Ur/a) \cos m\varphi e^{-i\beta z} \end{cases} \quad r < a \text{ (core)} \quad (A.1)$$

$$\begin{cases} E_{z2} = \frac{A}{K_m(W)} K_m(Wr/a) \sin m\varphi e^{-i\beta z} \\ H_{z2} = \frac{B}{K_m(W)} K_m(Wr/a) \cos m\varphi e^{-i\beta z} \end{cases} \quad r > a \text{ (cladding)} \quad (A.2)$$

where β is the light transmission constant and λ is the light wavelength. In addition m is the mode number, A and B are constants which can be derived from the boundary conditions, J_m is m th order of the Bessel function of the first kind and K_m is the m th order of the modified Bessel function of the second kind, r is the distance from the fiber core, a is the fiber core radius.

Finally U and W can be expressed as follows:

$$\begin{cases} U = a\sqrt{n_1^2 K_0^2 - \beta^2} \\ W = a\sqrt{\beta^2 - n_2^2 K_0^2} \end{cases} \quad (A.3)$$

According to the Maxwell's equations, the electric field and magnetic field at a distance r and φ direction can be expressed as:

$$\begin{cases} E_r = \left(-i\beta \frac{\partial E_z}{\partial r} - \frac{i\omega\mu}{r} \frac{\partial H_z}{\partial \varphi}\right)/K_c^2 \\ E_\varphi = \left(-\frac{i\beta}{r} \frac{\partial E_z}{\partial \varphi} + i\omega\mu \frac{\partial H_z}{\partial r}\right)/K_c^2 \\ H_r = \left(\frac{i\omega\varepsilon}{r} \frac{\partial E_z}{\partial \varphi} - i\beta \frac{\partial H_z}{\partial r}\right)/K_c^2 \\ H_\varphi = \left(-i\omega\varepsilon \frac{\partial E_z}{\partial r} - \frac{i\beta}{r} \frac{\partial H_z}{\partial \varphi}\right)/K_c^2 \end{cases} \quad (A.4)$$

where ε and μ are the dielectric constant and permeability of the light transmission medium and ω is the angular light frequency. The values of E_z and H_z can be calculated through equations (A.1) and (A.2), then E_r and E_φ , H_r and H_φ can be expressed as:

$$\begin{cases} E_{r1} = -i\left(\frac{a}{U}\right)^2 \frac{1}{J_m(U)} \left[-\frac{\omega\mu m B}{r} J_m\left(\frac{Ur}{a}\right) + \frac{\beta U A}{a} J'_m\left(\frac{Ur}{a}\right)\right] \sin m\varphi e^{-i\beta z} \\ E_{\varphi 1} = -i\left(\frac{a}{U}\right)^2 \frac{1}{J_m(U)} \left[-\frac{\beta m A}{r} J_m\left(\frac{Ur}{a}\right) - \frac{\omega\mu U B}{a} J'_m\left(\frac{Ur}{a}\right)\right] \cos m\varphi e^{-i\beta z} \\ H_{r1} = -i\left(\frac{a}{U}\right)^2 \frac{1}{J_m(U)} \left[-\frac{\omega\varepsilon_0 n_1^2 m A}{r} J_m\left(\frac{Ur}{a}\right) + \frac{\beta U B}{a} J'_m\left(\frac{Ur}{a}\right)\right] \cos m\varphi e^{-i\beta z} \\ H_{\varphi 1} = -i\left(\frac{a}{U}\right)^2 \frac{1}{J_m(U)} \left[-\frac{\beta m B}{r} J_m\left(\frac{Ur}{a}\right) + \frac{\omega\varepsilon_0 n_1^2 U A}{a} J'_m\left(\frac{Ur}{a}\right)\right] \sin m\varphi e^{-i\beta z} \end{cases} \quad (r < a) \quad (A.5)$$

and

$$\begin{cases} E_{r2} = i \left(\frac{a}{W}\right)^2 \frac{1}{K_m(W)} \left[-\frac{\omega\mu m B}{r} K_m\left(\frac{Wr}{a}\right) + \frac{\beta W A}{a} K'_m\left(\frac{Wr}{a}\right) \right] \sin m\varphi e^{-i\beta z} \\ E_{\varphi 2} = i \left(\frac{a}{W}\right)^2 \frac{1}{K_m(W)} \left[-\frac{\beta m A}{r} K_m\left(\frac{Wr}{a}\right) - \frac{\omega\mu W B}{a} K'_m\left(\frac{Wr}{a}\right) \right] \cos m\varphi e^{-i\beta z} \\ H_{r2} = i \left(\frac{a}{W}\right)^2 \frac{1}{K_m(W)} \left[-\frac{\omega\varepsilon_0 n_2^2 m A}{r} K_m\left(\frac{Wr}{a}\right) + \frac{\beta W B}{a} K'_m\left(\frac{Wr}{a}\right) \right] \cos m\varphi e^{-i\beta z} \\ H_{\varphi 2} = i \left(\frac{a}{W}\right)^2 \frac{1}{K_m(W)} \left[-\frac{\beta m B}{r} K_m\left(\frac{Wr}{a}\right) + \frac{\omega\varepsilon_0 n_2^2 W A}{a} K'_m\left(\frac{Wr}{a}\right) \right] \sin m\varphi e^{-i\beta z} \end{cases}$$

(A.6)

where

$$\begin{cases} J'_m\left(\frac{Ur}{a}\right) = \frac{\partial J_m\left(\frac{Ur}{a}\right)}{\partial r} \\ K'_m\left(\frac{Wr}{a}\right) = \frac{\partial K_m\left(\frac{Wr}{a}\right)}{\partial r} \end{cases}$$

(A.7)

According to the Maxwell's equations boundary conditions at the interface between the fiber core and cladding (where $r = a$) as listed below:

$$\begin{cases} E_{z1} = E_{z2} \\ H_{z1} = H_{z2} \\ E_{\varphi 1} = E_{\varphi 2} \\ H_{\varphi 1} = H_{\varphi 2} \end{cases}$$

(A.8)

As a result we have the eigen equation for the guided modes

$$\left[\frac{J'_m(U)}{U J_m(U)} + \frac{K'_m(W)}{W K_m(W)} \right] \left[\frac{n_1^2 J'_m(U)}{U J_m(U)} + \frac{n_2^2 K'_m(W)}{W K_m(W)} \right] = m^2 \frac{\beta^2}{K_0^2} \left(\frac{1}{U^2} + \frac{1}{W^2} \right)^2$$

(A.9)

Snyder & Love define the waveguide modes as electromagnetic field configurations which maintain their intensity profile during propagation in the fiber core [238]. Using equation (A.9), we could calculate the corresponding U , W , and β for a certain mode, and eventually obtain the mode distribution of E_r , E_φ and E_z , H_r , H_φ , and H_z .

The number of guided modes in an optical fiber is determined by the normalized frequency V . The larger the value of V , the more guided modes

could be supported in the optical fiber [237].

$$V = \frac{2\pi a}{\lambda} NA = \frac{2\pi a}{\lambda} \sqrt{n_1^2 - n_2^2} \quad (A.10)$$

If $V \leq 2.405$, only the fundamental mode (HE_{11}) can be guided in the fiber core, all other modes are cut-off. It is noted that if the waveguide design is fixed, the value of V depends only on the light wavelength λ , and hence the number of guided modes is wavelength dependent.

References

- [237] S. Li, C. Li, C. Song. *Optical Waveguide Theory Essentials (Chinese Edition)*, *Electronic Industry Press*, 2013.
- [238] L. Alan Snyder and J. Love, *Waveguide Theory*, *Springer US*, 1983.

Appendix C

List of multiple numbering references in this thesis

1. Ref. [9], [237].
S. Li, C. Li, C. Song. *Optical Waveguide Theory Essentials (Chinese Edition)*, Electronic Industry Press, 2013.
2. Ref. [21], [85], [98], [133].
Q. Wu, Y. Semenova, P. Wang, and G. Farrell, “High sensitivity SMS fiber structure based refractometer--analysis and experiment.,” *Opt. Express*, vol. 19, no. 9, pp. 7937–7944, 2011.
3. Ref. [23], [90].
Q. Wu, Y. Semenova, P. Wang, A. M. Hatta, and G. Farrell, “Experimental demonstration of a simple displacement sensor based on a bent single-mode-multimode-single-mode fiber structure,” *Meas. Sci. Technol.*, vol. 22, no. 2, pp. 025203, 2011.
4. Ref. [24], [91].
Q. Wu, M. Yang, J. Yuan et al., “The use of a bend singlemode-multimode-singlemode (SMS) fibre structure for vibration sensing,” *Opt. Laser Technol.*, vol. 63, pp. 29–33, 2014.
5. Ref. [38], [93], [232].
Q. Wu, Y. Semenova, P. Wang, et al., “A comprehensive analysis verified by experiment of a refractometer based on an SMF28-small-core singlemode fiber (SCSMF)-SMF28 fiber structure,” *J. Opt.*, vol. 13, no. 12, pp. 937–946, 2011.
6. Ref. [39], [101], [132].
Q. Wu, Y. Semenova, J. Mathew, P. Wang, and G. Farrell, “Humidity sensor based on a single-mode hetero-core fiber structure,” *Opt. Lett.*, vol. 36, no. 10, pp. 1752–1754, 2011.
7. Ref. [46], [235].

- O. Frazão, J. L. Santos, F. M. Araújo, and L. a Ferreira, “Optical sensing with photonic crystal fibers,” *Laser Photon. Rev.*, vol. 2, no. 6, pp. 449–459, 2008.
8. Ref. [47], [219].
W. Chen, S. Lou, L. Wang, H. Zou, W. Lu, and S. Jian, “Highly sensitive torsion sensor based on Sagnac interferometer using side-leakage photonic crystal fiber,” *IEEE Photonics Technol. Lett.*, vol. 23, no. 21, pp. 1639–1641, 2011.
9. Ref. [48], [215].
H. M. Kim, T. H. Kim, B. Kim, and Y. Chung, “Temperature-insensitive torsion sensor with enhanced sensitivity by use of a highly birefringent photonic crystal fiber,” *IEEE Photonics Technol. Lett.*, vol. 22, no. 20, pp. 1539–1541, 2010.
10. Ref. [49], [218].
O. Frazao, C. Jesus, J. M. Baptista, J. L. Santos, and P. Roy, “Fiber-optic interferometric torsion sensor based on a two-LP-mode operation in birefringent fiber,” *IEEE Photonics Technol. Lett.*, vol. 21, no. 17, pp. 1277–1279, 2009.
11. Ref. [50], [217].
P. Zu, C. C. Chan, Y. Jin *et al.*, “A temperature-insensitive twist sensor by using low-birefringence photonic-crystal-fiber-based Sagnac interferometer,” *IEEE Photonics Technol. Lett.*, vol. 23, no. 13, pp. 920–922, 2011.
12. Ref. [55], [185].
P. Rugeland and W. Margulis, “Revisiting twin-core fiber sensors for high-temperature measurements.,” *Appl. Opt.*, vol. 51, no. 25, pp. 6227–32, 2012.
13. Ref. [56], [181].
J. E. Antonio-Lopez, Z. S. Eznaveh, P. LiKamWa, A. Schülzgen, and R. Amezcua-Correa, “Multicore fiber sensor for high-temperature applications up to 1000°C.,” *Opt. Lett.*, vol. 39, no. 15, pp. 4309–4312, 2014.
14. Ref. [58], [189], [223]
C.-L. Lee, L.-H. Lee, H.-E. Hwang, and J.-M. Hsu, “Highly Sensitive Air-Gap Fiber Fabry–Pérot Interferometers Based on Polymer-Filled Hollow Core Fibers,” *IEEE Photonics Technol. Lett.*, vol. 24, no. 2, pp. 149–151, 2012.

15. Ref. [59], [190], [224].
C.-L. Lee, H.-Y. Ho, J.-H. Gu, T.-Y. Yeh, and C.-H. Tseng, “Dual hollow core fiber-based Fabry–Pérot interferometer for measuring the thermo-optic coefficients of liquids,” *Opt. Lett.*, vol. 40, no. 4, pp. 459–462, 2015.
16. Ref. [60], [191], [225].
M. S. Ferreira, L. Coelho, K. Schuster, J. Kobelke, J. L. Santos, and O. Frazão, “Fabry-Perot cavity based on a diaphragm-free hollow-core silica tube,” *Opt. Lett.*, vol. 36, no. 20, pp. 4029–31, 2011.
17. Ref. [61], [196], [227].
R. Gao, D. F. Lu, J. Cheng, Y. Jiang, L. Jiang, and Z. M. Qi, “Humidity sensor based on power leakage at resonance wavelengths of a hollow core fiber coated with reduced graphene oxide,” *Sensors Actuators, B Chem.*, vol. 222, pp. 618–624, 2016.
18. Ref. [62], [170], [228].
R. Gao, Y. Jiang, and Y. Zhao, “Magnetic field sensor based on anti-resonant reflecting guidance in the magnetic gel-coated hollow core fiber,” *Opt. Lett.*, vol. 39, no. 21, pp. 6293–6296, 2014.
19. Ref. [67], [113].
P. Wang, G. Brambilla, M. Ding, Y. Semenova, Q. Wu, and G. Farrell, “High-sensitivity, evanescent field refractometric sensor based on a tapered, multimode fiber interference,” *Opt. Lett.*, vol. 36, no. 12, pp. 2233–2235, 2011.
20. Ref. [107], [137].
G. Brambilla, V. Finazzi, and D. J. Richardson, “Ultra-low-loss optical fiber nanotapers,” *Opt. Express*, vol. 12, no. 10, pp. 2258–2263, 2004.
21. Ref. [122], [149].
A. Og. Dikovska, G. B. Atanasova, N. N. Nedyalkov, P. K. Stefanov, P. A. Atanasov, E. I. Karakoleva, and A. Ts. Andreev, “Optical sensing of ammonia using ZnO nanostructure grown on a side-polished optical-fiber,” *Sensors Actuators, B Chem.*, vol. 146, no. 1, pp. 331–336, 2010.
22. Ref. [123], [150].
S. K. Mishra, D. Kumari, and B. D. Gupta, “Surface plasmon resonance based fiber optic ammonia gas sensor using ITO and polyaniline,” *Sensors Actuators, B Chem.*, vol. 171–172, pp. 976–983, 2012.

23. Ref. [131], [164].

Q. Wu, Y. Semenova, P. Wang, G. Farrell, “A comprehensive analysis verified by experiment of a refractometer based on an SMF28-small-core singlemode fiber (SCSMF)-SMF28 fiber structure,” *J. Opt.*, vol. 13, no. 12, pp. 125401, 2011.

24. Ref. [134], [162], [171].

D. Liu, A. K. Mallik, J. Yuan, C. Yu, G. Farrell, Y. Semenova, and Q. Wu, “High sensitivity refractive index sensor based on a tapered small core single-mode fiber structure,” *Opt. Lett.*, vol. 40, no. 17, pp. 4166–4169, 2015.

25. Ref. [158], [173].

D. Liu, W. Han, A. K. Mallik, J. Yuan, C. Yu, G. Farrell, Y. Semenova, and Q. Wu, “High sensitivity sol-gel silica coated optical fiber sensor for detection of ammonia in water,” *Opt. Express*, vol. 24, no. 21, pp. 24179–24187, 2016.

26. Ref. [159], [234].

J. C. Echeverría, M. Faustini, and J. J. Garrido, “Effects of the porous texture and surface chemistry of silica xerogels on the sensitivity of fiber-optic sensors toward VOCs,” *Sensors Actuators, B Chem.*, vol. 222, pp. 1166–1174, 2016.

27. Ref. [174], [204].

H. N. Li, D. S. Li, and G. B. Song, “Recent applications of fiber optic sensors to health monitoring in civil engineering,” *Eng. Struct.*, vol. 26, no. 11, pp. 1647–1657, 2004.

28. Ref. [195], [229].

A. M. Zheltikov, “Ray-optic analysis of the (bio)sensing ability of ring-cladding hollow waveguides,” *Appl. Opt.*, vol. 47, no. 3, pp. 474–479, 2008.